



Dumb-Bell of Variable Length in an Elliptic Orbit: Relative Equilibria, Periodicity, and Chaos

Alexander Burov¹ and Ivan Kosenko²

¹ Dorodnicyn Computing Center of the RAS, Moscow, Russia
(E-mail: aburov@ccas.ru)

² Russian State University of Tourism and Service, Moscow Region, Russia
(E-mail: kosenko@ccas.ru)

Abstract. Planar motion of an orbiting dumb-bell having a variable length in a central field of gravity is under analysis. Within the so-called “satellite approximation” planar attitude dynamics is described by a non-autonomous equation of the second order. The role of the dumb-bell length vibrations implying an existence of the radial and tangent relative equilibria for any value of the orbit eccentricity is proposed. Stability of the found relative equilibria and chaoticity for total dynamics are investigated.

Splitting of separatrices for the perturbed, with respect to the pendulum-like motions, problem is established. This effect was proved not only for small eccentricities, but also for their finite values. Moreover, it turned out that the chaotic dynamics of a dumb-bell with an invariable mass distribution, existing because of the ellipticity of the orbit, cannot be suppressed with aid of periodic variations of the mass distribution, or the dumb-bell length. Nevertheless one might observe islands of regularity corresponding to librations of large amplitude demonstrating stable behavior. These librations can be useful for the transportation operation in the near-transversal directions of the dumb-bell orbital motion.

Keywords: dumb-bell, elliptic orbit, controlled motion, attitude dynamics, splitting of separatrices, chaoticity, islands of regularity.

1 Introduction

The dynamics of space objects, including moving elements, has been investigated by many authors. These studies usually have been connected with the necessity to estimate the influence of relative motions of moving parts, for example, crew motions [1,2], circulation of liquids [3], etc. on the attitude dynamics of a spacecraft.

The development of projects of large-scale space systems with mobile elements, in particular, of satellite systems with tethered elements and space elevators, has posed problems related to their dynamics. Various aspects of the role of mass distribution even for the simplest orbiting systems, like dumb-bell systems are known since the publications [4–7], etc. The possibility of the sudden loss of stability because of the mass redistribution has been pointed out in [8] (see also [9–13]).



The considered system belongs to the mentioned class of systems and represents by itself one of the simplest systems allowing both analytical and numerical treatment without supplementary simplifying assumptions such as smallness of the orbital eccentricity. Another set of applied problems is related to orientation keeping of the system for deployment and retrieval of tethered subsatellites as well as for relative cabin motions of space elevators. In particular the problem of the stabilization/destabilization possibility for the given state of motion due to rapid oscillations of the cabin exists. This could be the subject of another additional investigation.

2 Satellite Approximation

Consider motions of a body in a central force field with a center O . Assume the body is equipped by facilities of the mass redistribution, for example, by massive points, which are able to move with respect to it along some prescribed curves. Introduce a frame $OX_1X_2X_3$ fixed in the absolute space. If C is a center of mass for the body, really an orbital system, then one can introduce the so-called König's frame (KF) with the origin in the point C and with the axes collinear to the axes of absolute frame. According to König's theorem the kinetic energy of the system can be presented as a sum of the kinetic energy associated to the movement of the center of mass and the kinetic energy associated to the movement of the particles relative to the center of mass.

Let $Cx_1x_2x_3$ be the mobile frame (MF) having an origin at the whole system center of mass, and tracking certain spatial orientation, see below for details. One can find further that kinetic energy of the motion relative to KF might be represented as $T = T_1 + T_2 + T_3$ with the terms having the form

$$T_1 = \frac{1}{2} (\mathbf{I}\boldsymbol{\omega}, \boldsymbol{\omega}), \quad T_2 = (\boldsymbol{\omega}, \mathbf{K}), \quad T_3 = \sum \mu(\dot{\boldsymbol{\rho}}, \dot{\boldsymbol{\rho}}),$$

where \mathbf{I} is the central tensor of inertia of the whole system in MF; $\boldsymbol{\omega}$ is a vector of the angular velocity of the MF with respect to the KF given by its projections onto the axes of MF; \mathbf{K} is the relative, with respect to the MF, kinetic moment of the system; summation spans all points of the body; μ is the mass of the particular point; $\boldsymbol{\rho}$ is the radius vector for this point with respect to MF.

Since one assumes that the points perform prescribed motions with respect to the MF, described by functions of time only, the function T_3 also depends on time only. Hence it does not play any role for derivation of the equations of motion and can be omitted from the Lagrange function.

Further, one makes two principal assumptions, though general enough, related to the rules of mass redistribution in the body: (a) $\mathbf{I} = \text{diag}(I_1, I_2, I_3)$; (b) $\mathbf{K} = 0$. Such an approach is motivated by examples of an affinely, in particular, similarly deformable bodies ([14–16]) as well as cross-shaped bodies considered in [6,7,17]. Other examples with a mass distribution along a



straight line are discussed below. Within these assumptions one can choose initial conditions and a rule of the mass redistribution in a way such that the plane Cx_3x_1 is coincident to the orbital frame for all time of motion. It means that the axis Cx_2 remains orthogonal to the orbital plane.

If the body dimensions are small compared to the radius of orbit of the mass center, then one may speak about consideration of motion in the so-called “satellite approximation”. Developing expression for the kinetic and potential energy with respect to the small parameter equal to the ratio of the characteristic size of the body and the distance from its mass center to the attracting center, we obtain the Lagrange function

$$L = L_0(r, \dot{r}, \dot{\nu}) + L_2(t, r, \dot{\nu}, \varphi, \dot{\varphi}), \quad L_2 \ll L_0,$$

$$L_0 = \frac{m}{2} (\dot{r}^2 + r^2 \dot{\nu}^2) + \frac{GMm}{r}, \quad L_2 = \frac{I_2}{2} (\dot{\nu} + \dot{\varphi})^2 + GM \frac{I_3 - I_1}{2r^3} (3 \cos^2 \varphi - 1),$$

where m is the body mass, G is the Gauss gravitational constant, M is the mass of the attracting center. The angle φ characterises a deviation of the axis Cx_1 from the local vertical, the angle ν is the *true anomaly*. The strain rate term in the kinetic energy is additive and within the accepted assumptions depends on time only. This is a reason why it is omitted in the expression for the Lagrange function.

Within the frame of the considered approximation the attitude dynamics of the satellite as well as its vibrations do not affect the motion of its mass center being described by the Kepler problem with the Lagrange function L_0 . At the same time the attitude dynamics defined by L_2 with an explicit time dependence through r and ν is described by the equation

$$\frac{d}{dt} [I_2(\dot{\varphi} + \dot{\nu})] = -GM \frac{3(I_3 - I_1)}{r^3} \sin \varphi \cos \varphi. \quad (1)$$

In order to integrate this equation one must substitute here the expressions for r and ν , found from the altitude dynamics. It means that in difference with the above case the orbital motion of the mass center plays an important role for its attitude dynamics. Thus, similar to [18], performing the proper Kepler reduction one can use the true anomaly ν as an independent variable instead of t .

Supposing that the moments of inertia are also parameterized by ν , one is able write the equation describing the attitude dynamics of the body with variable mass distribution as

$$\frac{d}{d\nu} \left[(1 + e \cos \nu)^2 I_2 \left(1 + \frac{d\varphi}{d\nu} \right) \right] = -3(I_3 - I_1)(1 + e \cos \nu) \cos \varphi \sin \varphi. \quad (2)$$

The equation (2) is a direct generalisation of the so-called Beletsky equation for the bodies with a variable mass distribution. Beletsky’s equation, initially written in [19], possesses a Lagrangian structure and can be obtained from Hamilton’s principle after the preliminary change of the independent



variable described above. However this fact was not explicitly described, so far in [20] the Hamiltonian representation of this equation was guessed, but not obtained via a regular way.

Now we obtain immediately from the equation (2) the following

Corollary 1. *If the variations in the mass distribution are arranged in a way such that*

$$(1 + e \cos \nu)^2 I_2 = I_2^* = \text{const}, \quad (3)$$

then the equation (2) possesses partial solutions of two kinds: (A) $\varphi = 0, \pi$, (B) $\varphi = \pm\pi/2$ existing for all values of the orbital eccentricity. At relative equilibria corresponding to these solutions the body is oriented pointing to the attracting center by the ends of the axes Cx_3 and Cx_1 respectively.

The simplest interesting example of such systems relates to the objects with mass distribution along the line segment. Suppose that the object is located in the Cx_1 axis. Then $I_1 = 0$, $I_2 = I_3 = I$. If the mass redistribution satisfies (3), then resolving this relation with respect to I and substituting the solution into (2), one obtains

$$(1 + e \cos \nu) \varphi'' + 3 \sin \varphi \cos \varphi = 0. \quad (4)$$

This equation depends only on the eccentricity e of the orbit. Let us study its properties in dependence on this parameter.

2.1 Relative equilibria and their stability

Under the mentioned conditions the system with a linear mass distribution possesses relative equilibria (A) and (B). For the relative equilibria (A), known as *vertical* or *radial* ones the dumb-bell is oriented along the local vertical and turned to the attracting center by one of its endpoints. Then $\varphi = 0$ or $\varphi = \pi$. For the relative equilibria (B), known as *tangent* ones, the dumb-bell is oriented along the tangent to the orbit of the center of mass.

In order to investigate stability of steady motions (A), that are most interesting from the practical viewpoint, denote the absolute value of the monodromy matrix trace for the Eq. (4) linearized in vicinity of $\varphi = 0$ or $\varphi = \pi$ by $|\text{tr } A|$. The numerical experiment demonstrates that the necessary condition, that reads $|\text{tr } A| < 2$, see [21] for example, is fulfilled for all e excepting may be a countable set of the eccentricity values $e \approx 0.748, 0.945, 0.986, 0.999 \dots$ with infinite oscillations of the value $\text{tr } A$ between -2 and 2 while approaching unit eccentricity, see Fig. 1. By virtue of Zhukovsky's result [22], see also [23], Ch. VIII, the stability conditions are fulfilled if $e \leq 1/4$.

2.2 Splitting of separatrices and chaotic dynamics

The equation (4) for small values of eccentricity e can be written as

$$\delta'' + 3(1 - e \cos \nu + \dots) \sin \delta = 0, \quad \delta = 2\varphi.$$

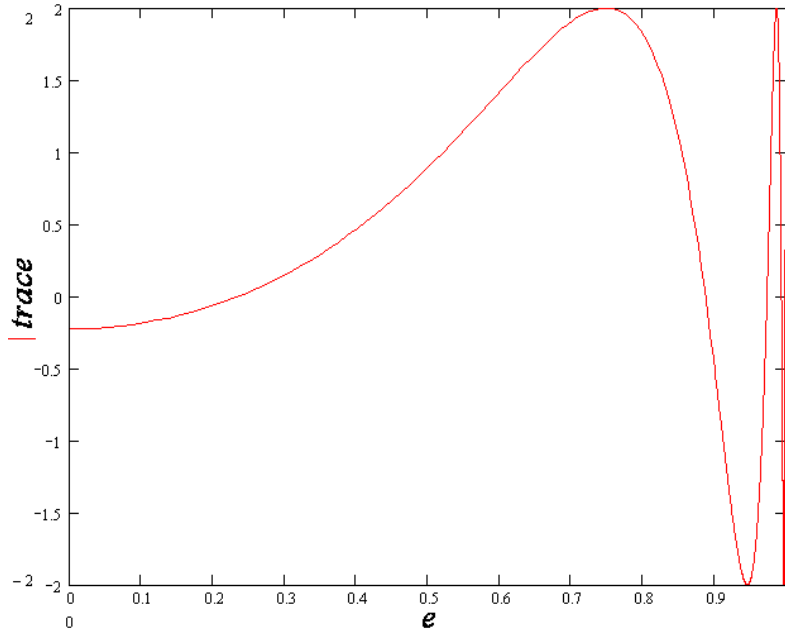


Fig. 1. Trace of the monodromy matrix as a function of the eccentricity.

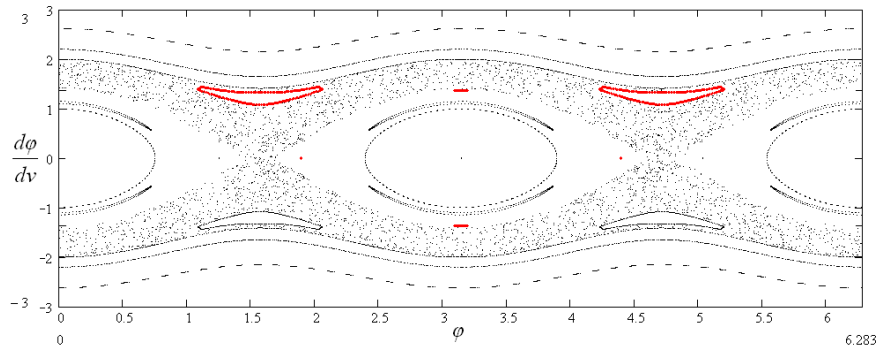


Fig. 2. Poincaré iterated map for $e = 0.33$.

For equations of this kind the splitting of separatrices, and as a consequence the non-integrability are established in [24] not only for small, but also for finite values of the parameter. Thus the chaotic dynamics, observed in the problem of oscillations of a satellite with constant inertia moments [20] cannot be suppressed by periodic variations of the mass distribution. The dependence of the equation on the only parameter partially simplifies a qualitative investigation of system's dynamics. Poincaré iterated one-period maps are depicted in Fig. 2 for the value $e = 0.33$ as an illustration, some interesting trajectories are highlighted by red color. One can observe that the growth of the parameter leads to enlargement of the regions of chaotic

behavior in vicinity of the splitted separatrices, accompanied by appearing of stable, from the numerical viewpoint, periodic motions, bordered by invariant tori.

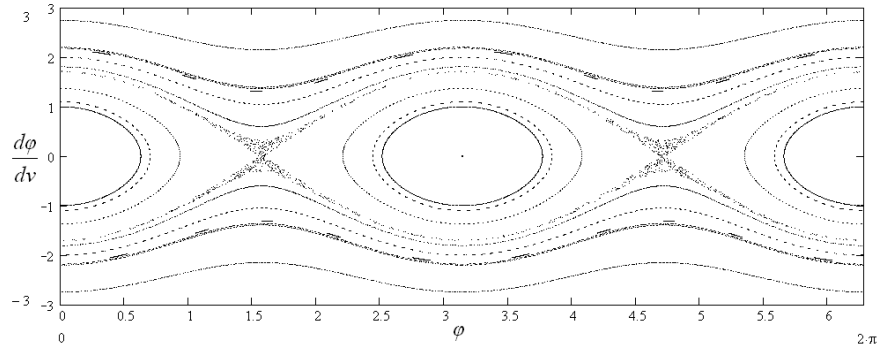


Fig. 3. Poincaré iterated map for $e = 0.03$.

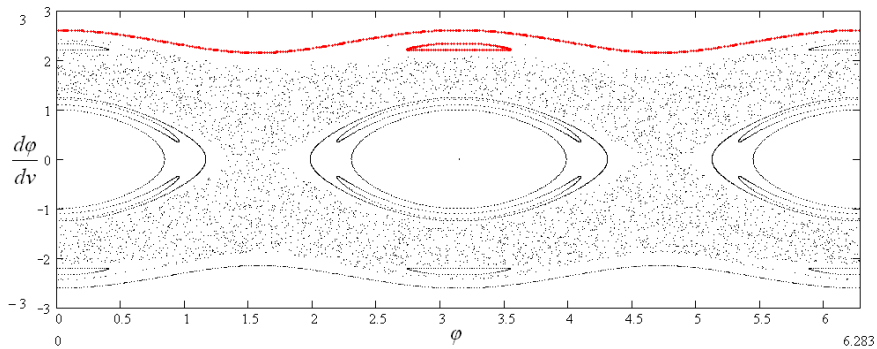


Fig. 4. Poincaré iterated map for $e = 0.53$.

One can estimate the chaoticity growth as the eccentricity increases by comparing Poincaré iterated map portraits for different values of $e = 0.03, 0.33, 0.53$ shown in Figs. 3, 2, 4 sequentially. Note that as numerical experiments show the chaoticity is a common case in the problem under consideration, without any correlation with the specific control law like (3).

3 Examples

There exist two important examples of bodies with a linear variable mass distribution, namely, a pulsating dumb-bell and a dumb-bell with a cabin wandering between its endpoints. Consider these examples separately.

First, assume the body is composed of a massless rod and a couple of mass points m_1 and m_2 , located at its endpoints. Suppose the rod length ℓ varies with time according to the prescribed rule and both endpoints are



located at the same plane, fixed to the absolute space and passing through the attracting center O . Let C be, as above, the dumb-bell center of mass, (r, ν) are the point C polar coordinates, and φ is the angle between the ray OC and the dumb-bell.

If the length of the dumb-bell is invariable then $\ell' = 0$ in the previous equation, and the change of variable $\delta = 2\varphi$ leads to so-called Beletsky's equation. Further if the length of the dumb-bell varies as $\ell = \ell_0 (1 + e \cos \nu)^{-1}$, then the condition (3) is fulfilled, and the equation (2) reads as (4). It is remarkable that the speed of the length variation vanishes in apsides of the orbit.

Second, assume the body is composed of a massless rod AB of the length ℓ and a couple of mass points m_A and m_B , located at its endpoints. Suppose that there exists a cabin K of the mass m_K performing motions between the endpoints of the dumb-bell according to the prescribed rule, which is evidently a generalization of [9] where the cabin position on the rod was fixed. Let both endpoints be located at the same plane, being fixed in the absolute space and passing through the attracting center O . Introducing a parameter $f \in \mathbf{R}$ one can implement a positioning of the cabin using the relation $\overrightarrow{OK} = f\overrightarrow{OA} + (1 - f)\overrightarrow{OB}$. Thus the moment of inertia I can be presented as a quadratic function of this parameter:

$$I = I(f) = m^{-1}\ell^2 (m_A m_B + m_B m_K f^2 + m_A m_K (1 - f)^2). \quad (5)$$

If we want to fix the MF orientation at relative equilibria, radial or transverse, then the variable f has to satisfy equation (3) where one has to replace the variable I_2 by the expression for variable I defined in equation (5).

4 Acknowledgements

The authors are grateful to Professor Troger who inspired key ideas of this work and proposed some interesting directions of future investigations. They are also thankful to Professor D. P. Chevallier for important comments. The investigation is partially supported by RFBR, grants 08-01-00600-a, 08-08-00553-a, 08-01-00718-a.

References

- 1.W. T. Thomson and V. C. Fung. Instability of spinning stations due crew motion. *AIAA Journal*, 3:1082-1087, 1965.
- 2.R. A. Amir and D. J. Newman. Research into the effects of astronaut motion on the spacecraft: A review. *Acta Astronautica*, 47:12:859-869, 2000.
- 3.N. N. Moiseev and V. V. Rumyantsev. *Dynamic stability of bodies containing fluid*, Ed. by N. H. Abramson, New York, 1968. Springer-Verlag.
- 4.Yu. M. Okunev. On some properties of translational-rotational motions of a long dumb-bell in a central force field. *Sci. Reports, Inst. of Mechanics, Mosc. State Univ.*, :10:87-121, 1971.



- 5.V. V. Beletsky and O. N. Ponomareva. A parametric analysis of relative equilibrium stability in the gravitational field. *Cosmic Research*, 28:5:664-675, 1990.
- 6.A. A. Burov and A. V. Karapetyan. On the motion of cross-shaped bodies. *Mechanics of Solids*, 30:6:11-15, 1995.
- 7.A. A. Burov. The motion of cross-shaped bodies around a fixed point in a central Newtonian force field. *J. Appl. Math. Mech.*, 60:1:25-30, 1996.
- 8.A. Burov and H. Troger. On relative equilibria of an orbital pendulum suspended with a tether. In *Second Polyakhov Readings. Selected papers*, pages 73-81, Saint-Petersburg, 2000.
- 9.V. Buchin, A. Burov, and H. Troger. A dumb-bell satellite with a cabin. Existence and stability of relative equilibria. In *Proceedings of ENOC-2008. June 30-July 4*, Saint-Petersburg, Russia, 2008. <http://lib.physcon.ru/download/p1749.pdf>
- 10.A. V. Rodnikov. The algorithms for capture of the space garbage using “Leier Constraint”. *Regular and Chaotic Dynamics*, 11:4:483-489, 2004.
- 11.A. V. Rodnikov. On systems with “Leier Constraint” in the central Newtonian force field. In *Proceedings of ENOC-2008. June 30-July 4*, Saint-Petersburg, Russia, 2008. <http://lib.physcon.ru/download/p1729.pdf>
- 12.A. V. Rodnikov. Rotations of a dumbbell equipped with “the Leier Constraint”. *Journal of Vibroengineering (JVE)*, 10:4:557-561, 2008.
- 13.I. I. Kosenko and S. Ya. Stepanov. Stability of relative equilibria of an orbit tether with impact interactions taken into account. The unbounded (read: unrestricted) problem. *Mechanics of Solids*, 41:4:64-72, 2006.
- 14.D. N. Seiliger. *Theory of motion of an similarly variable body*. Typo-Lithography of Kazan’ Imperial University, Kazan’, 1892.
- 15.N. G. Chetaev. *Theoretical mechanics*, Moscow, 1987. Mir Publishers.
- 16.J. J. Ślawniowski. The mechanics of the homogeneously-deformable body. Dynamical models with high symmetries. *ZAMM*, 62:6:229-240, 1982.
- 17.A. A. Burov and D. P. Chevallier. On motion of a rigid body about a fixed point with respect to a rotating frame. *Reg. Chaot. Dyn.* 3:2:1-11, 1998.
- 18.V. V. Beletsky. *Motion of an artificial satellite about its center of mass*. Jerusalem, 1966. Israel Program for Scientific Translation.
- 19.V. V. Beletsky. On libration of a satellite. In *Artificial Earth Satellites. No. 3*. Moscow, pages 13-31, 1959. Academy of Sciences of the USSR.
- 20.A. A. Burov. Nonintegrability of the equation of plane oscillations of a satellite in an elliptic orbit. *Mosc. Univ. Math. Bull.* 39:1:38-41, 1984.
- 21.V. I. Arnold. *Mathematical methods of classical mechanics. Graduate Texts in Mathematics. Vol. 60. Edition 2*. NY. XVI, 1989. Springer-Verlag.
- 22.N. E. Zhukovsky. Conditions of finiteness of integrals for the equation $d^2y/dx^2 + py = 0$. *Math. Sbornik*, XVI:582-591, 1892.
- 23.V. A. Yakubovich and V. M. Starzhinsky. *Linear differential equations with periodic coefficients, Parts I and II*, NY, 1975. Wiley.
- 24.V. V. Kozlov. Oscillations of one-dimensional systems with a periodic potential. *Mosc. Univ. Mech. Bull.* 35:5-6:74-78, 1980.
- 25.A. A. Burov. On oscillations of a vibrating dumb-bell in an elliptic orbit. Accepted by *Doklady Physics*.
- 26.B. M. Balk and V. G. Boltyanski. *Geometry of masses*. Moscow, 1987. Nauka. (in Russian).



Deterministic coherence resonance in systems with on-off intermittency and delayed feedback

J. Buryk, A. Krawiecki, and T. Buchner

Faculty of Physics, Warsaw University of Technology,
Koszykowa 75, PL-00-662 Warsaw, Poland

Abstract. Coherence resonance consists in the increase of regularity of an output signal of a nonlinear device for non-zero intensity of input noise. This phenomenon occurs, e.g., in stochastic systems with delayed feedback in which external noise amplifies the periodic component of the output signal with the period equal to the delay time. In this contribution it is shown that in chaotic systems with delayed feedback deterministic (noise-free) coherence resonance can occur, which consists in the maximization of the periodic component of the output signal in the absence of stochastic noise, due to the changes in the internal chaotic dynamics of the system as the control parameter is varied. This phenomenon is observed in systems with on-off intermittency and attractor bubbling, including generic maps and systems of diffusively coupled chaotic oscillators at the edge of synchronization. The occurrence of deterministic coherence resonance for the optimum value of the control parameter (e.g., of the coupling strength between synchronized oscillators) is characterized by the appearance of a series of maxima at the multiples of the delay time in the probability distribution of the laminar phase lengths, superimposed on the power-law trend typical of on-off intermittency, and by the presence of a strong maximum in the power spectrum density of the output signal.

Keywords: on-off intermittency, coherence resonance, delayed feedback.

On-off intermittency (OOI) is a sort of extreme bursting which occurs in systems possessing a chaotic attractor within an invariant manifold whose dimension is less than that of the phase space [1,2]. As a control parameter crosses a certain threshold this attractor undergoes a supercritical blowout bifurcation [3] and loses transverse stability, and a new attractor is formed which encompasses that contained within the invariant manifold. Just above the blowout the phase trajectory stays for long times close to the invariant manifold and occasionally departs from it; if the distance from the invariant manifold is an observable, this results in a sequence of laminar phases and bursts. The distribution of laminar phase lengths τ obeys a power scaling law $P(\tau) \propto \tau^{-3/2}$ [1]. In the presence of additive noise chaotic bursting occurs below the blowout bifurcation threshold; this phenomenon is known as attractor bubbling [2,4]. OOI and attractor bubbling were observed in systems as diverse as model maps with time-dependent control parameter [1], chaotic synchronization [5], spin-wave chaos [6], microscopic models of financial markets [7], etc.



The role of delayed feedback is important in many systems [8-10], e.g. optical resonators, chemical reactions and physiology [8] or chaos control [9,10]. In this paper the influence of delayed feedback on OOI is studied using generic one-dimensional maps with a time-dependent control parameter and synchronized oscillators. It is shown that addition of delayed feedback changes the threshold for the blowout bifurcation and can influence the character of the intermittent bursting: For optimum choice of the control parameter a strong periodic component in the time series above the blowout occurs, with the period equal to the delay time. This is an example of coherence resonance (CR) [11-18], a phenomenon related to the well-known stochastic resonance (SR) [19]. CR manifests itself as the peak of regularity of the output signal of certain nonlinear stochastic systems for optimum intensity of the input noise and without any external periodic stimulation. In particular, CR was observed in systems with delayed feedback, including bistable [16] and excitable [17] ones and simple threshold crossing detectors [18]. Since in the models under consideration the role of external noise is played by the internal chaotic dynamics within the invariant manifold, the observed phenomenon is deterministic CR [20], a counterpart of the noise-free (deterministic) SR [21].

As a basic model let us consider the logistic map with the time-dependent control parameter and delayed feedback

$$y_{n+1} = (1 - K) a \zeta_n y_n (1 - y_n) + K y_{n-k}, \quad (1)$$

where $0 < K < 1$ is an amplitude of the feedback term and $\zeta_n \in (0, 1)$ denotes any chaotic process constrained to the unit interval. The map in Eq. (1) has the invariant manifold $y_n = 0$ with the chaotic attractor ($\zeta_n \in (0, 1), y_n = 0$) within it. For $a > a_c$ the variable y_n exhibits intermittent bursts, where a_c is the blowout bifurcation threshold dependent on ζ_n . For $K = 0$ Eq. (1) is the generic model for OOI [1]. The qualitative properties of OOI are independent of the details of the dynamics within the invariant manifold provided that the correlation time of the process ζ_n is negligible in comparison with the mean time between bursts, which is true just above the threshold for the blowout bifurcation; hence, ζ_n can be approximated by white noise ξ_n uniformly distributed on $(0, 1)$ [1]. It should be also noted that Eq. (1) with the control parameter constant in time, i.e., with $\zeta_n \equiv 1$, (the logistic map with delayed feedback) can serve as a model for chaos control [10].

For $y_n \approx 0$ the dynamics transverse to the invariant manifold is well approximated by a linearization of Eq. (1),

$$y_{n+1} \approx (1 - K) a \zeta_n y_n + K y_{n-k}. \quad (2)$$

Introducing new variables in the direction transverse to the invariant manifold, $y_n^{(1)} = y_n, y_n^{(2)} = y_{n-k}, \dots, y_n^{(j)} = y_{n-k+j-2}, \dots, y_n^{(k+1)} = y_{n-1}$ [10] Eq. (2) can be written as a linear transformation

$$\mathbf{y}_{n+1} = \hat{M}_n \mathbf{y}_n, \quad (3)$$



where $\mathbf{y}_n = (y_n^{(1)}, y_n^{(2)}, \dots, y_n^{(k+1)})^T$ (thus, $\mathbf{y}_n = 0$ is the invariant manifold), and

$$\hat{M}_n = \begin{pmatrix} (1-K)a\zeta_n & K & 0 & 0 & \dots & 0 \\ 0 & 0 & 1 & 0 & \dots & 0 \\ 0 & 0 & 0 & 1 & \dots & 0 \\ \vdots & \vdots & \vdots & \vdots & \ddots & \vdots \\ 1 & 0 & 0 & 0 & \dots & 0 \end{pmatrix}. \quad (4)$$

The transverse stability of the attractor within the invariant manifold is controlled by the transverse Lyapunov exponent λ_T [1-3],

$$\lambda_T = \lim_{N \rightarrow \infty} \frac{1}{N} \ln \frac{\|\hat{M}_{N-1} \dots \hat{M}_2 \hat{M}_1 \mathbf{y}_0\|}{\|\mathbf{y}_0\|}, \quad (5)$$

where \mathbf{y}_0 is an arbitrary initial vector transverse to the invariant manifold (in simulations, \mathbf{y}_0 is assumed as a random vector of unit length). The exponent λ_T increases with a from negative to positive values and crosses zero at the threshold for the blowout bifurcation $a = a_c$, corresponding to the onset of OOI.

The dependence of a_c on K for the map (1) with $\zeta_n = \xi_n$ and various k is shown in Fig. 1(a). The value of a_c weakly depends on k and monotonically decreases to $a_c = 2.0$ for $K \rightarrow 1$. Typical time series y_n for a just above a_c is shown in Fig. 1(b). For increasing K the character of the time series changes from intermittent bursts with high amplitude typical of OOI to frequent bursts with small amplitude. There is also a gap between the minimum value of y_n and the invariant manifold $y_n = 0$. Thus the effect of the delayed feedback on the generic model for OOI resembles that of additive noise which prevents the phase trajectory from approaching closely the invariant manifold and lowers the threshold for the occurrence of bursting, leading to attractor bubbling [2,4]. This is not surprising since the additive noise enters Eq. (1) in the same way as the feedback term; moreover, especially for long k , due to decreasing correlation, the feedback term can be treated as a sort of deterministic noise.

For $K > 0$ the distribution of laminar phase lengths $P(\tau)$ for a just above a_c exhibits a series of maxima at the values of τ equal to k and its multiples (Fig. 1(c)) superimposed on a power-law trend typical of OOI. Let us define the output signal as $Z_n = 0$ if y_n is in the laminar phase and $Z_n = 1$ if y_n is in the burst phase (such discretization is typical in the study of systems with stochastic resonance). Then, a broad peak centered at the frequency $2\pi/k$ appears in the power spectrum density (PSD) of Z_n (Fig. 1(d)). Both absolute and relative (with respect to the mean value of the PSD on the interval $(\pi/k, 3\pi/k)$) height of this peak exhibit maximum as functions of a (Fig. 1(e)); these quantities correspond to the spectral power amplification (SPA) and signal-to-noise ratio (SNR) used in the studies of SR, respectively.

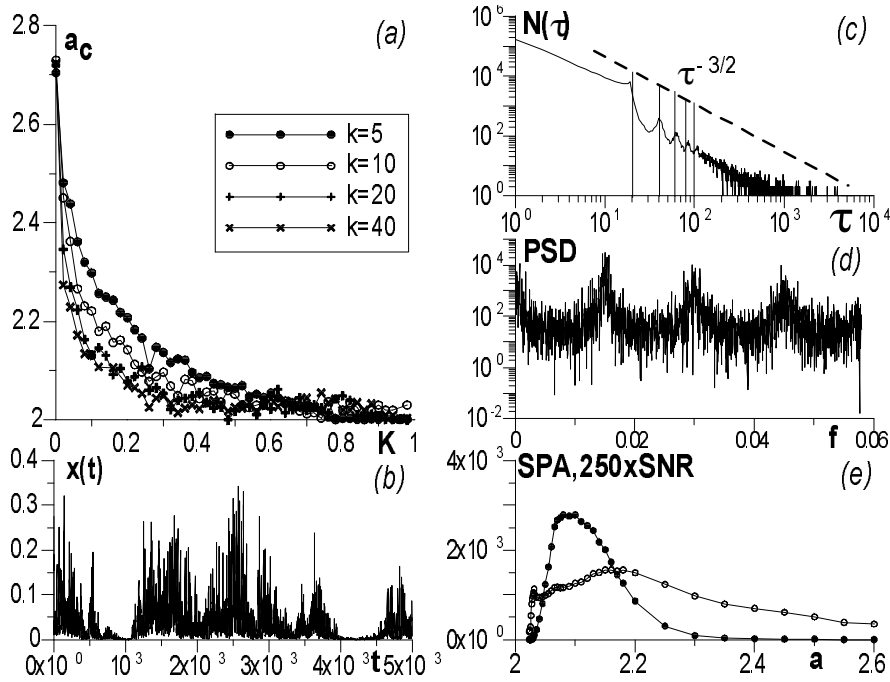


Fig. 1. For the map given by Eq. (1) with $\zeta_n = \xi_n$: (a) intermittency threshold a_c vs. K for various k (see legend); (b) time series $y_n(t)$ for $k = 20$, $K = 0.2$, $a = 2.2$ (just above a_c), the initial condition is $y_0 \in (0, 1)$, where y_0 is a random number, and $y_{-1} = y_{-2} = \dots y_{-k+1} = 0$; (c) histogram of the number of laminar phases $N(\tau)$ of duration τ for $k = 20$, $K = 0.3$, $a = 2.1$, y_n was assumed to be in the burst phase ($Z_n = 1$) if $y_n > 0.01$, vertical lines are drawn at multiples of k ; (d) PSD from the time series Z_n for $k = 64$, $K = 0.3$, $a = 2.1$; (e) SPA (circles) and SNR (dots) vs. a for $k = 64$, $K = 0.3$.

The height of these maxima increases, their width decreases and their location approaches $a = a_c$ as $K \rightarrow 1$ since then the feedback term becomes dominant in Eq. (1) and the signal Z_n is almost periodic for a just above a_c .

These results show that CR occurs in the map (1) as the control parameter is increased above the threshold for the blowout bifurcation. In fact, systems with OOI resemble excitable ones, in particular just above the intermittency threshold when the bursts are short in comparison with the quiescent laminar phases. Thus, CR in the map (1) resembles that observed in excitable systems and threshold-crossing detectors with delayed feedback and external noise [17,18], e.g., the multiple maxima in the histogram of laminar phase lengths in Fig. 1(c) correspond to those found in the histograms of inter-spike intervals in excitable systems with CR [12]. However, CR in the map (1) appears due to changes of the internal dynamics within the invariant manifold as the control parameter is varied rather than under the influence of external noise.



Thus, this phenomenon belongs to the class of deterministic CR as in Ref. [20].

Similar phenomena were observed in a system of two diffusively coupled chaotic Rössler oscillators,

$$\begin{aligned}\dot{x}_1 &= -(y_1 + z_1) \\ \dot{y}_1 &= x_1 + ay_1 + k(y_2 - y_1) + Ks(\tau) \\ \dot{z}_1 &= b + z_1(x_1 - c) \\ \dot{x}_2 &= -(y_2 + z_2) \\ \dot{y}_2 &= x_2 + ay_2 + k(y_1 - y_2) - Ks(\tau) \\ \dot{z}_2 &= (b + \delta b) + z_2(x_2 - c),\end{aligned}\tag{6}$$

where $a = 0.2$, $b = 0.2$, $c = 11$, k is the strength of the diffusive coupling, $s(\tau) = y_2(t-\tau) - y_1(t-\tau) = \Delta y(t-\tau)$ provides delayed feedback with delay τ and amplitude K , and small $\delta b \neq 0$ can be added to model the mismatch of parameters in an experimental system. For $K = 0$ and $\delta b = 0$ the oscillators are identically synchronized for $k > k_c \approx 0.12$ and there is a chaotic attractor within the invariant synchronization manifold $x_1 = x_2$, $y_1 = y_2$, $z_1 = z_2$. For $k < k_c$ synchronization is lost (i.e., the invariant manifold loses transverse stability) and $\Delta y(t) = y_2(t) - y_1(t)$ exhibits chaotic bursts typical of OOI; thus, k is the control parameter for the supercritical blowout bifurcation. For $\delta b \neq 0$ bursts occur already for $k > k_c$ due to attractor bubbling. Similarly, the delayed feedback $Ks(\tau)$ with $K > 0$ also forces the trajectory to leave the invariant manifold, as in Eq. (1), and causes the onset of intermittent bursts for $k > k_c$.

Typical time series of $\Delta y(t)$ exhibiting OOI are shown in Fig. 2(a). If, again, the output signal is defined as $Z(t) = 0$ if $\Delta y(t)$ is in the laminar phase and $Z(t) = 1$ if $\Delta y(t)$ is in the burst phase, a broad peak centered at the frequency $2\pi/\tau$ appears in the PSD of $Z(t)$ for a range of k below and just above k_c (Fig. 2(b)). The height of this peak (SPA) exhibits maximum as a function of k , both for $\delta b = 0$ and $\delta b > 0$ (Fig. 2(c)); in the latter case only the range of the control parameter where the bursts are observed is slightly broadened toward higher values. This demonstrates that deterministic CR occurs in the system given by Eq. (6) and the output signal exhibits maximum regularity for optimum value of the parameter k which controls the internal dynamics within the invariant synchronization manifold. The maximum of the SNR vs. k is not clearly visible (Fig. 2(d)): evaluating PSD from much longer time series would probably lead to smoother curves of the SNR. Hence, the results of numerical simulations suggest that deterministic CR can be observed experimentally in systems of coupled chaotic oscillators at the edge of identical synchronization.

To summarize, the influence of delayed feedback on OOI was studied using generic maps with the time-dependent control parameter and synchronized chaotic oscillators. It was found that delayed feedback can decrease

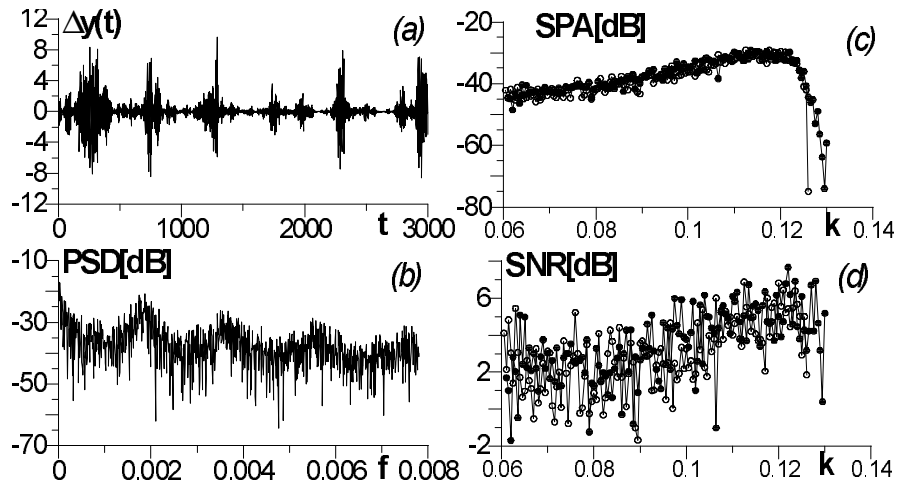


Fig. 2. For the system of diffusively coupled Rössler oscillators given by Eq. (1) with $\tau = 512$, $K = 0.05$, (a) time series $\Delta y(t)$ for $k = 0.12$, $\delta b = 10^{-4}$; (b) PSD from the time series $Z(t)$ for $k = 0.12$, $\delta b = 10^{-4}$, $\Delta y(t)$ was assumed to be in the burst phase ($Z(t) = 1$) if $\Delta y(t) > 0.1$; (c) SPA and (d) SNR vs. k for $\delta b = 0$ (circles) and $\delta b = 10^{-4}$ (dots)

the threshold for the blowout bifurcation. Deterministic CR was observed in systems under consideration, characterized by the appearance of a series of maxima at the multiples of the delay time in the probability distribution of the laminar phase lengths, superimposed on the power-law trend typical of OOI, and by the presence of a strong periodic component in the intermittent time series, with period equal to the delay time. The strength of this component exhibits maximum as the control parameter is varied, due to the changes of the internal dynamics of the system within the invariant manifold.

References

1. N. Platt, E. A. Spiegel, and C. Tresser, *Phys. Rev. Lett.* 70:279, 1993; J. F. Heagy, N. Platt, and S. M. Hammel, *Phys. Rev. E* 49:1140, 1994; S. C. Venkataramani et al., *Physica D* 96:66, 1996.
2. P. Ashwin, J. Buescu, and I. N. Stewart, *Phys. Lett. A* 193:126, 1994.
3. E. Ott and J. Sommerer, *Phys. Lett. A* 188:39, 1994.
4. N. Platt, S. M. Hammel, and J. F. Heagy, *Phys. Rev. Lett.* 72:3498, 1994; S. C. Venkataramani et al., *Phys. Rev. Lett.* 77:5361, 1996.
5. A. Čenys et al., *Phys. Lett. A* 213:259, 1996.
6. F. Rödelsperger, A. Čenys, and H. Benner, *Phys. Rev. Lett.* 75:2594, 1995; A. Krawiecki and A. Sukiennicki, *Acta Phys. Polonica A* 88:269, 1995.
7. T. Lux and M. Marchesi, *Nature* 297:498, 1999; A. Krawiecki, J. A. Hołyst, and D. Helbing, *Phys. Rev. Lett.* 89:158701, 2002.



- 8.G. Giacomelli, R. Meucci, A. Politi, and F. T. Arecchi, *Phys. Rev. Lett.* 73:1099, 1994; I. R. Epstein, *J. Chem. Phys.* 92:1702, 1990; M. C. Mackey and L. Glass, *Science* 197:287, 1977.
- 9.K. Pyragas, *Phys. Lett. A* 170:421, 1992; H. U. Voss, *Phys. Rev. Lett.* 87:014102, 2001.
- 10.T. Buchner and J. J. Żebrowski, *Phys. Rev. E* 63:16210, 2001.
- 11.H. Gang et al., *Phys. Rev. Lett.* 71:807, 1993; W.-J. Rappel and S. H. Strogatz, *Phys. Rev. E* 50:3249, 1994.
- 12.A. Longtin, *Phys. Rev. E* 55:868, 1997.
- 13.A. S. Pikovsky and J. Kurths, *Phys. Rev. Lett* 78:775, 1997; J. R. Pradines, G. V. Osipov, and J. J. Collins, *Phys. Rev. E* 60:6407, 1999; G. Giacomelli, M. Giudici, and S. Balle, *Phys. Rev. Lett.* 84:3298, 2000.
- 14.A. Neiman, P. I. Saporin, and L. Stone, *Phys. Rev. E* 56:270, 1997; I. Z. Kiss et al., *Phys. Rev. E* 67:035201, 2003; O. V. Ushakov et al., *Phys. Rev. Lett.* 95:123903, 2005.
- 15.C. Palenzuela et al., *Europhys. Lett.* 56:347, 2001.
- 16.L. S. Tsimring and A. Pikovsky, *Phys. Rev. Lett.* 87:250602, 2001; D. Huber and L. S. Tsimring, *Phys. Rev. Lett* 91:260601, 2003; D. Huber and L. S. Tsimring, *Phys. Rev. E* 71:036150, 2005; K. Panajotov et al., *Phys. Rev. A* 69:011801, 2004; M. Arizaleta Arteaga et al., *Phys. Rev. Lett.* 99:023903, 2007; Y. Jin and H. Hu, *Physica A* 382:423, 2007.
- 17.G. C. Sethia, J. Kurths, and A. Sen, *Phys. Lett. A* 364:227, 2007.
- 18.R. Morse and A. Longtin, *Phys. Lett. A* 359:640, 2006.
- 19.R. Benzi, A. Sutera, and A. Vulpiani, *J. Phys. A* 14:L453, 1981; L. Gammaitoni et al., *Rev. Mod. Phys.* 70:223, 1998; V. S. Anischenko et al., *Physics — Uspekhi* 42:7, 1999 [*Usp. Fiz. Nauk* 169:7, 1999]; F. Moss, "Stochastic resonance: looking forward", in: J. Walleczek (Ed.), *Self-Organized Biological Dynamics & Nonlinear Control*, page 236, Cambridge, UK, 2000, Cambridge University Press.
- 20.J. F. Martinez Avila, H. L. D. de S. Cavalcante, and J. R. Rios Leite, *Phys. Rev. Lett.* 93:144101, 2004.
- 21.V. S. Anishchenko, A. B. Neiman, and M. A. Safanova, *J. Stat. Phys.* 70:183, 1993; V. S. Anishchenko, M. A. Safonova, and L. O. Chua, *Int. J. Bifurcation & Chaos* 4:441, 1994; E. Reibold et al., *Phys. Rev. Lett.* 78:3101, 1997; S. Matyjaśkiewicz et al., *Phys. Rev. E* 63:026215, 2001.
- 22.Ying-Cheng Lai, *Phys. Rev. E* 53:R4267, 1996.





Detection of jet axis in a horizontal turbulent jet via nonlinear analysis of minimum/maximum temperature time series

A. Charakopoulos⁽¹⁾, T.E. Karakasidis^{(1)*}, P.N. Papanicolaou⁽²⁾

⁽¹⁾ *Department of Civil Engineering, University of Thessaly, 38334 Volos,
Greece*

⁽²⁾ *Department of Civil Engineering, National Technical University of Athens,
Athens Greece*

*thkarak@uth.gr

Abstract

We have analyzed experimental temperature time series from a horizontal turbulent heated jet, in order to identify the jet axis location using non linear measures. The analysis was applied on both, the original time series as well as on the extreme value (minimum and maximum values) time series. In our analysis we employed mainly non-linear measures such as mutual information and cumulative mutual information. The results show that the analysis of the extreme values time series using cumulative mutual information permits to distinguish the jet axis time series from the rest of the jet, as well as discriminate regions of the jet located close to jet axis or close to the boundaries. Furthermore, it is of interest that the application of simple statistical measures and clustering techniques shows that the use of extremes time series let us distinguish with greater confidence the jet axis than the use of the original one.

Keywords: Non-linear time series analysis, turbulence, mutual information, cumulative mutual information, clustering

1. Introduction

Jet flow is a very important research subject that has attracted scientific interest due to extensive applications in environmental engineering. So far a large number of investigations have been carried out to locate the trajectory and understand the turbulence properties of the flow using statistical methods which do not necessarily lead to understanding the dynamics of the flow [3, 19].

The transition from laminar to turbulent flow in a jet has been extensively studied as a fundamental non linear dynamical problem [4, 5, 17, 25]. The study of dynamical systems by analysis of the time series of a variable measured in a physical system, is of particular interest over the last decades, and gives the possibility of comprehension the underlying system dynamics. Time series analysis may include linear and non linear methods. The linear analysis includes simple statistical measures such as autocorrelation function and power spectrum, while non linear analysis methods based on the reconstruction of phase through spaces include the mutual information and correlation dimension. For a concise review of these methods one can consult the book by Kantz and Schreiber (1995) [10] and Abarabnel (1996) [1]. These more complex methods



allow us to extract more detailed characteristics of the underlying dynamical system.

In this paper linear and non linear measures are used to analyze temperature fluctuation time series. Our aim was to study the dynamic characteristics of the temperature fluctuation experiment. More specifically we analyze the temperature fluctuation measurements recorded using fast response thermistors along a horizontal line in order to investigate if one can discriminate time series corresponding to regions close to the jet axis, where conditions of fully developed turbulence are expected, from time series corresponding to regions that are more distant and from those close to the boundary with the ambient water. Horizontal buoyant jet investigations [2, 6, 9, 18] are mainly concerned with the structure of the flow.

The novelty of the present work is that the analysis was applied both on the original time series as well as on the extreme value (minimum and maximum values) time series. The initial time series is reduced to a series (extreme time series) of successive pairs of minimum and maximum values. The objective of our analysis is to investigate whether it is possible that a time series of extreme values can reveal dynamic characteristics of the underlying system in the same or better way as the analysis of the original time series. One can easily understand that the interest is important, since this would permit us to study dynamical systems using reduced information.

The structure of the paper is as follows. In Sec. 2 we discuss briefly the theoretical background and the experimental set-up for the temperature measurements. In Sec.3 we present the methodology employed for data analysis along with the linear and nonlinear measures. The results and discussion are presented in Sec. 4. Finally the conclusions are presented in Sec. 5.

2. Theory and Experimental Set-up

2.1 Theory

A horizontal heated round jet of diameter D and density ρ_o flows out of a nozzle with velocity U in a calm ambient fluid of density ρ_a . The specific volume, horizontal momentum and buoyancy fluxes are defined as

$$\begin{aligned} Q &= \frac{\pi D^2}{4} U \\ M &= QU \quad \text{and} \\ B &= g_o' Q = \frac{\rho_a - \rho_o}{\rho_a} g Q \end{aligned} \quad (1)$$

respectively, where g is the gravitational acceleration and g_o' the effective gravity that will subsequently produce vertical momentum flux. Fisher et al. (1979) [7] have defined two characteristic length scales as



$$l_Q = \frac{Q}{M^{1/2}} \quad \text{and} \quad l_M = \frac{M^{3/4}}{B^{1/2}} \quad (2)$$

the ratio of which is the initial jet Richardson number R_o

$$R_o = \frac{l_Q}{l_M} = \left(\frac{\pi}{4}\right)^{1/4} \frac{\sqrt{g_o D}}{U} = \left(\frac{\pi}{4}\right)^{1/4} \frac{1}{F_o} \quad \text{and} \quad F_o = \frac{U}{\sqrt{g_o D}} \quad (3)$$

where F_o is the initial densimetric Froude number.

The temperature difference between the jet and ambient fluid produces the density deficiency that is responsible for the initial jet specific buoyancy flux.

The dilution S at a point of the jet flow field is defined to be the ratio

$$S = \frac{T_o - T_a}{T - T_a} \quad (4)$$

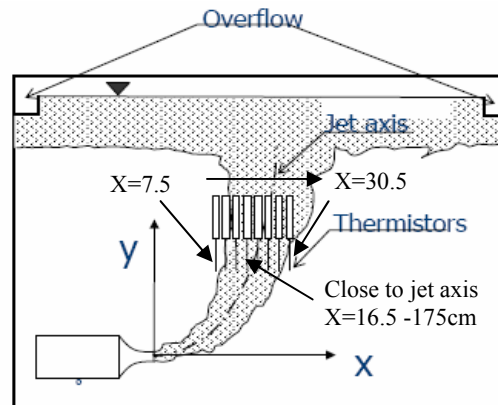
Where T_o is the initial jet temperature T_a the ambient temperature and the T the local time-averaged temperature. Jirka (2004) [8] has defined the jet axis to be the point of minimum dilution S_c

$$S_c = \frac{T_o - T_a}{T_c - T_a} \quad (5)$$

where T_c is the maximum time-averaged (centerline) temperature. We define x_c and y_c the horizontal and vertical distances from the nozzle where the jet axis is located. Near the nozzle ($x/l_M < 1$) the jet trajectory is horizontal, the flow is mainly driven by the initial momentum flux and it is characterized as jet-like [18]. When ($y/l_M > 2$) the trajectory of the flow is altered to vertical and the flow is characterized as plume-like. The flow regime ($1 < x/l_M < 5$) is the transition from jet-like to plume-like flow [18], [21].

2.2 Experimental setup

The experiments were performed at the Hydromechanics and Environmental Engineering Laboratory of the University of Thessaly [20]. The dispersion tank is made of 12.5mm thick Lucite with orthogonal horizontal section 0.90m x 0.60m and 0.80m depth. A perspective view of the experimental setup is shown in Fig.1.



.Fig. 1. Perspective view of the experimental setup

The tank was equipped with a peripheral overflow to remove excess water. In this matter the depth of water is fixed at 77 cm. The hot water jet supply consists of a water heater made of stainless steel, which is well insulated and pressurized by air at 2 atm, to provide adequate constant head pressure to drive to jet. During the water heating, a recirculating pump was used to ensure that the hot water is well mixed and there are no temperature gradients. An insulated pipe drives the water from the heater into the jet plenum, through a calibrated flow meter. A jet nozzle of 0.65cm diameter was used. The jet water temperature was around 60 °C, while the ambient water temperature ranged between 18 to 20 °C. Temperature measurements were obtained by an array of eight fast response thermistors spaced equally at 1cm apart, positioned at constant elevation from the nozzle, on the plane of symmetry of the buoyant jet. The jet was made visible by means of a slide projector on a semitransparent paper sheet (shadowgraph) in order to place the rake of thermistors properly. In this paper, we use the data recorded at an elevation of 5cm above the nozzle axis. The initial parameters of the flow are shown in table 1. We analyzed 24 recordings of temperature time series, one for each location of measurement, where the sampling time at each location was 30s at a frequency of 200Hz. Comprehensive details about the experimental setup can be found in Karakasidis et al (2009) [11].

Table 1. Experimental conditions

D(cm)	W(cm/s)	T _o (°C)	T _a (°C)	M(cm ⁴ /s ²)	B(cm ⁴ /s ³)	Re	l _m (cm)	R _o	y _c /l _m
0.65	29.25	60	17.8	284	149	1646	5.66	0.102	0.883

3. Time series analysis

3.1 Methodology

In an effort to discriminate the jet axis time series from the rest of the jet we used linear and nonlinear measures applied both on the original time series as well as on the extreme value (minimum and maximum values) time series. The initial time series is reduced to a series (extreme time series) of successive pairs of minimum and maximum values following the methodology by D.Kugiumtzis et al., 2006 [14]. The goal of this work was to examine if simple linear and non linear methods such as cumulative mutual information, can discriminate different states of systems from the analysis of the reduced length time series, instead of the full original time series.

3.2 Data set – Extreme time series model

As already mentioned 24 time series of temperatures have been recorded using fast response thermistors along a horizontal line of a fully developed turbulent heated jet. Consequently some of the time series correspond to conditions of turbulent flow (time series derived close to centerline of the jet) while other time series, obtained close to the boundary between the heated jet and the ambient water, have intermittent (laminar and turbulent) flow characteristics. Each time series consist of 6000 observations.

We derived new *extreme time series* of successive maximum and minimum values from each initial time series. Suppose we have a time series of length N , $\chi(t)$, $t = 1, 2, \dots, N$. If $y_1 = \chi(t_1)$ the first minimum, $y_2 = \chi(t_{1+\dots})$ the first turning point (maximum), $y_3 = \chi(t_{2+\dots})$ the second turning point (minimum) etc we extract from the initial time series the time series $y(t) = y_1, y_2, y_3, \dots, y_n$ called *extreme time series*. The extracted time series have lengths varying from $N=130$ to 1500 depending on the structure of the initial time series.

An example of a whole initial and extreme time series is shown in Fig. 2(a). In Fig. 2 (b) a zoom of a segment of the initial temperature time series of Fig 2(a) is presented.

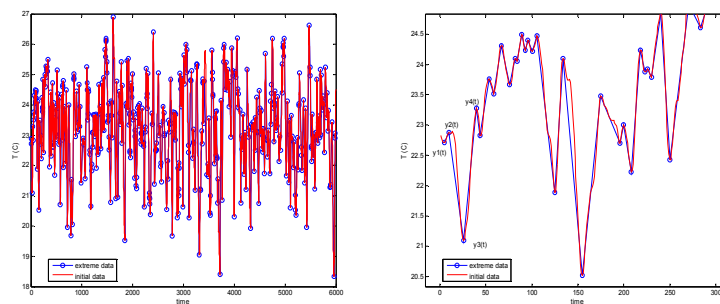


Fig. 2. (a) Initial and extreme time series. (b) Segment of initial and extreme time series.



3.3 Nonlinear measures

The most widely known nonlinear measure, which is used to select the appropriate delay time τ for state space reconstruction is the Mutual Information $I(t)$ and is defined as:

$$I(\tau) = \sum_{x(t_i), x(t_i+\tau)} P(x(t_i), x(t_i+\tau)) * \log \left[\frac{P(x(t_i), x(t_i+\tau))}{P(x(t_i)) * P(x(t_i+\tau))} \right] \quad (6)$$

Where $x(t_i)$ is the i^{th} data point of time series, $\tau = k\Delta t (k = 1, 2, \dots, k_{\max})$; $P(x(t_i))$ is the probability density at $x(t_i)$; $P(x(t_i), x(t_i + \tau))$ is the joint probability density at $x(t_i), x(t_i + \tau)$; τ is the delay time.

The delay t of the first minimum is chosen as a delay time for the reconstruction of phase space.

We also used a new nonlinear measures the *Cumulative Mutual Information* $M(\tau_{\max})$, defined as the sum of mutual information $I(t)$ D.Kugiumtzis et al., 2007 [14] for a number of delay τ .

$$M(\tau_{\max}) = \sum_{\tau=1}^{\tau_{\max}} I(\tau) \quad (7)$$

3.4 Clustering analysis using the Cumulative Mutual Information function

Clustering is an important technique that groups together similar data sets. Several studies used clustering methods based on mutual information [23, 24]. In our study we used single linkage hierarchical clustering algorithm in order to classify our data. The clustering techniques applied both on the original time series as well as on the extreme value (minimum and maximum values) time series. As a measure of similarity we used the *Cumulative Mutual Information*.

One of the main advantages of hierarchical clustering is that a dendrogram can be drawn to find the appropriate number of clusters in a dataset. Briefly we propose the following clustering algorithm steps:

- We compute the Euclidean distance y between pairs of objects in n -by- p data matrix X . Rows of X correspond to observations; columns correspond to variables.
- We create a hierarchical cluster tree z from the distances in y (y is a Euclidean distance matrix or a more general dissimilarity matrix, formatted as a vector)
- Finally we group the data set into clusters. The most dependent data are grouped together.

4. Results and Discussion

During the experiment the jet axis (at elevation 5cm above the nozzle axis) was located by optical measurements nearly at the midpoint between the jet

boundaries ($x=16.5 - 17.5$ cm). This was also supported by the behavior of the average temperatures observed in these time series, as well as from Recurrence Plot analysis [11]. It is well known from the theory of fluid mechanics that turbulence near the center of the jet is fully developed. There appear many short-lived small scale turbulent structures, while near the jet boundary the large scale flow structures live longer.

We calculated the mutual information function for both, the original as well as for the extreme data series and the results are presented in Figs. 3(a)-(b). In Fig. 3 (b) we observe that for the extreme time series reported at $x=16.5$ cm and $x=17.5$ cm (points which are near jet axis) the mutual information function clearly attains the lowest values for any value of the time delay, if compared to the results for the rest of the time series. Such behavior is consistent with what we expected since close to the jet centreline the memory of the flow structures is lost fast.

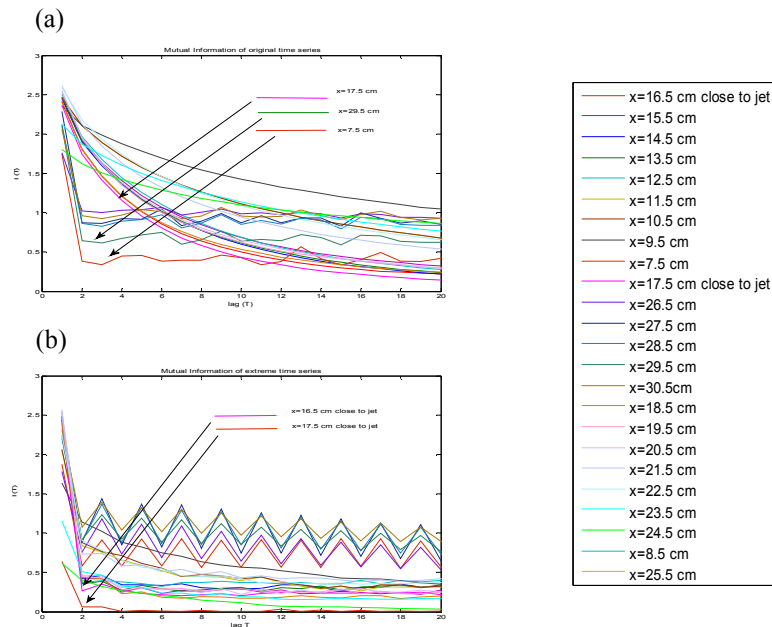


Fig. 3. (a) Mutual information of the Initial time series along the horizontal line. (b) Mutual information of the Extreme time series along the horizontal line

In Fig. 3(a) we can see that there are time series presenting the smallest local minimum but not the lowest values of average mutual information which correspond in fact to regions in or close to the ambient water, while time series close to the jet axis (close to $x=17.5$ cm) present the lowest values of average mutual information although for larger lags. As we get far from the jet axis, but always in the turbulent jet region, average mutual information increases and time lags of the minimum are shifted toward larger times. We must however

bear in mind that the time lags are not directly compared for the original and the extreme time series, since the distance between successive points varies.

In Fig.4 (a) and (b) we summarize results for the cumulative mutual information for the original and extreme time series. A close look in Fig. 4(b), where the cumulative mutual information for the extreme time series is presented, indicates that we can discriminate three main regions corresponding to time series. The first region corresponds to a set of time series too far from the centerline of jet ($x=7.5\text{cm}$, $x=27.5\text{cm}$, $x=28.5\text{cm}$, $x=29.5\text{cm}$, $x=30.5\text{cm}$). The second region corresponds to a set of time series very close to the center of jet ($x=16.5\text{cm}$, $x=15.5\text{cm}$, $x=17.5\text{cm}$, $x=18.5\text{cm}$, $x=19.5\text{cm}$). The third region corresponds to a set of time series ($x=9.5\text{cm}$, $x=21.5\text{cm}$, $x=22.5\text{cm}$, $x=23.5\text{cm}$) far from the center of jet but not as much as the time series from the first region.

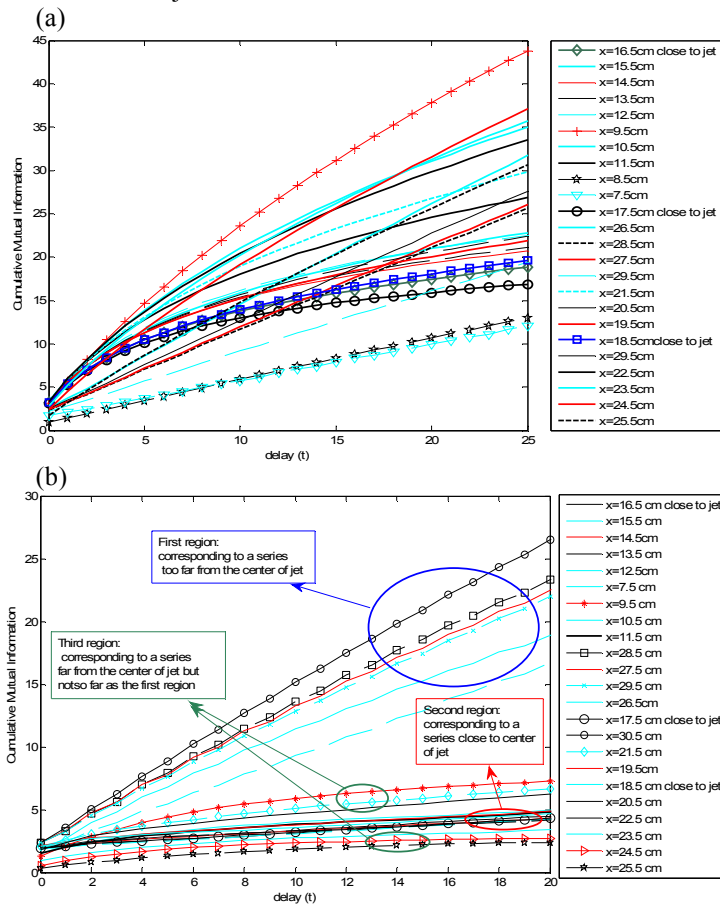


Fig. 4. (a) Cumulative Mutual information of the Initial time series along the horizontal line. (b) Cumulative Mutual information of the Extreme time series along the horizontal line.



It is of interest to note that such a detailed discrimination of the three regions is not so straightforward in Fig. 4(a) where the cumulative mutual information from the original time series is presented.

Furthermore we evaluate the discriminating power of cumulative mutual information, applying a clustering algorithm to the set of our cumulative mutual information time series. For the clustering we used the algorithm described in paragraph 3.4. The hierarchy built by the clustering algorithm based on cumulative mutual information from reduced and original time series is represented by the dendrograms given in Fig. 5 and Fig.6.

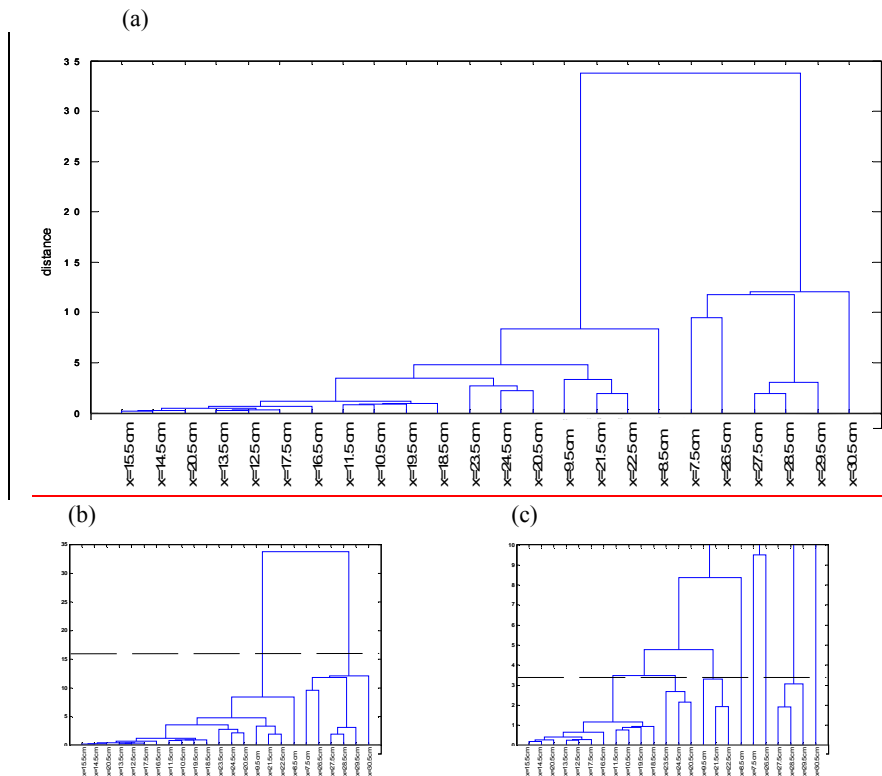


Fig. 5. (a), (b), and (c) Dendrogram Cumulative Mutual information of the Extreme time series along the horizontal line at different cut point

In Figure 5(a) we present the hierarchy clustering of each extreme time series. We decided to make two "cuts" at the dendrogram at different levels of distance (vertical axis). In Fig. 5(b), the first "cut" is made at distance~16, where one can clearly see two main partitions. One main group consisted from the time series at $x=7.5\text{cm}$, $x=26.5\text{cm}$, $x=27.5\text{cm}$, $x=28.5\text{cm}$, $x=29.5\text{cm}$, $x=30.5\text{cm}$. This group corresponds to the region too far from the axis of the jet.



The second main cluster includes the remaining time series. This first step is important because we can exclude the time series corresponding to the edges of the measuring area.

In Fig. 5 (c) we can see the dendrogram which results in from the second ‘‘cut’’ at distance~3.5. We can see more clearly some major cluster and some smaller. Specifically the time series at $x=23.5\text{cm}$, $x=24.5\text{cm}$, $x=20.5\text{cm}$ and at $x=9.5\text{cm}$, $x=21.5\text{cm}$, 22.5cm join and at $x=21.5\text{cm}$, $x=10.5\text{cm}$, $x=19.5\text{cm}$ is joined with $x=18.5\text{cm}$. These above partitions correspond to a set of time series far from the center of jet but not as much as the time series from the first step ($x=7.5\text{cm}$, $x=26.5\text{cm}$, $x=27.5\text{cm}$, $x=28.5\text{cm}$, $x=29.5\text{cm}$, $x=30.5\text{cm}$).

Moreover in Fig. 5 (c) we can distinguish other some small clusters which include the time series at $x=15.5\text{cm}$, $x=14.5\text{cm}$, $x=20.5\text{cm}$ and $x=13.5\text{cm}$, $x=12.5\text{cm}$, $x=17.5\text{cm}$. We can notice that the time series at $x=16.5\text{cm}$ correspond close to the centerline of jet is separate from other.

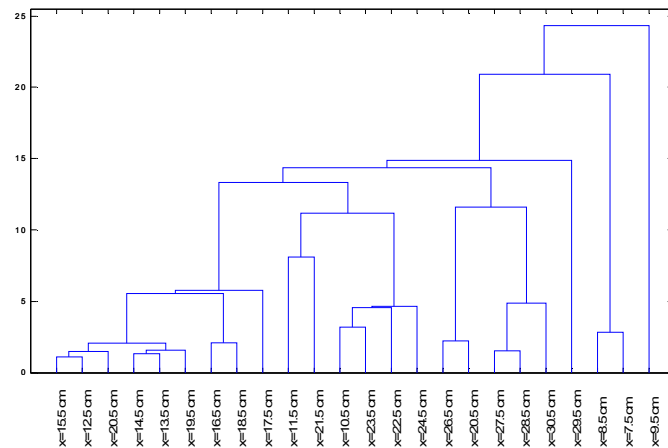


Fig. 6. Dendrogram Cumulative Mutual information of the Initial time series along the horizontal line.

As we can see in Fig 6 where the results for the cumulative mutual information resulting from the analysis of the original time series are presented, there are several clusters without the same discriminating structure observed from the analysis of the extremes time series (Fig.5).

5. Conclusions

In this work we have investigated a new approach in order to detect the jet axis of temperature time series derived from experimental data. The novelty of this study is that the analysis was applied both on the original time series as well as on the extreme value (minimum and maximum values) time series. More specifically we focus to a new measure the *Cumulative Mutual Information*, and



we showed that it can discriminate the underlying dynamics from one time series to another. Another important issue is that the performance of the *Cumulative Mutual Information* was applied to a reduced length time series (extreme time series) and showed that it has higher discriminating power than in the original time series. This issue is very important if we take into account the size of the computational analysis of original data due to the length of the time series.

6. References

- [1] Abarabnel H.D.I. Analysis of observed chaotic data. Springer, Berlin. 1996.
- [2] Anwar, H.O., 1969. Behavior of a buoyant jet in a calm fluid, Proc. ASCE, J. Hyd. Div.. 95(4), 1289-1303.
- [3] Bradshaw P. Turbulence, Topics in Applied Physics, 12, Springer, 1978
- [4] Broze G. and Hussain F. Transitions to chaos in a forced jet: intermittency, tangent bifurcations and hysteresis. *J. Fluid Mech.* 331, 37-71, 1996.
- [5] Crow S. C, and Champagne F. H. Orderly structure in jet turbulence. *J. Fluid Mech.* 48, 3, 547-591, 1971.
- [6] Fan, L-N., 1967, Turbulent buoyant jets into stratified or flowing ambient fluids, Rep. No. KH-R-15, W.M. Keck Laboratory of Hydraulics and Water Resources, California Institute of Technology, Pasadena, California.
- [7] Fischer H. B, List E. J, Koh R. C. Y, Imberger J, and Brooks N. H. Mixing in Inland and Coastal Waters (Academic Press), 1979.
- [8] Jirka G. H. Integral model for turbulent buoyant jets in unbounded stratified flows. Part I: Single round jet. *Env. Fluid Mech.* 4, 1-56, 2004.
- [9] Johnston A. J., Phillips C. R. and Volker R.E. Modeling horizontal round buoyant jets in shallow water. *Journal of Hydrauling Engineering* . 120, 1994.
- [10] Kantz H. and Schreiber T. Nonlinear time series analysis. Cambridge University Press, Cambridge, 1995.
- [11] Karakasidis T. E., Liakopoulos A., Fragkou A. and Papanicolaou P. N. Recurrence Quantification Analysis of Temperature Fluctuations in a Horizontal Round Heated Jet. *International Journal of Bifurcation and Chaos*, 19, 2487-2498. 2009.
- [12] Kraskov A, Stogbauer H, Andrzejak R. G, and Grassberger P. Hierarchical clustering using mutual information. *Europhysics Letters*, 70(2), 278-284, 2005
- [13] Kugiumtzis D, Kehagias A and Aifantis E. C. Statistical analysis of the extreme values of stress time series from Portevin-Le Chatelier effect. *Physical Review E*, 70, 036110, 2004.
- [14] Kugiumtzis D, Pavana A, Tsimpiris A, Vlachos I, and Larsson PG. Time series feature evaluation in discriminating preictal EEG states. *Lecture Notes in Computer Science* . 4345, 298-310, 2006.
- [15] Kugiumtzis D, and Vlachos I. Turning point prediction of oscillating time series using local dynamic regression models. arXiv:0809.2229v1, 12 Sep 2008
- [16] Kugiumtzis D, Vlachos I, Pavana A, and Larsson PG. Assessment of measures of scalar time series analysis in discriminating preictal states. *International journal of Bioelectromagnetism*, 9(3), 134-145, 2007.
- [17] Mataoui A, and Schiestel R. Unsteady phenomena of an oscillating turbulent jet flow inside a cavity: Effect of aspect ratio. *Journal of Fluids and Structures*. 25, 60-79, 2009.
- [18] Michas S. N. and Papanicolaou P.N. Horizontal round heated jets into calm uniform ambient. *Desalination*. 248, 803-815, 2009.



- [19] Monin A. S, and Yaglom A .M. Statistical Fluid Mechanics, 2 (MIT Press, Cambridge) 1975
- [20] Palamitzoglou G. *Diploma Thesis*, Department of Civil Engineering, University of Thessaly. 2005.
- [21] Papanicolaou P. N. and List E. J. Investigations of round vertical turbulent buoyant jets. *J. Fluid Mech.* 195, 341-391, 1988.
- [22] Papanicolaou P. N. and List E. J. Statistical and spectral properties of tracer concentration in round buoyant jets. *Int. J. Heat Mass Transfer.* 30, 2059-2071, 1987.
- [23] Priness I, Maimon O, and Ben-Gal I. Evaluation of gene-expression clustering via mutual information distance measure, *Bioinformatics*, 8(6), 111, 2007
- [24] Tourassi G, Frederick E, Markey M, and Floyd C. Application of the mutual information criterion for feature selection in computer-aided diagnosis, *Med. Phys.*, 28(12), 2394-2402, 2001.
- [25] Wang X, and Keat Tan S. Environmental fluid dynamics-jet flow. *Journal of Hydrodynamics*, 22(5), 1009-1014, 2010.



Multifractal Analysis of the Psychorelaxation Efficiency for the Healthy and Pathological Human Brain *

Olga E. Dick

Pavlov Institute of Physiology of Russian Academy of Science, St. Petersburg,
Russia
E-mail: glazov.holo@mail.ioffe.ru

Abstract: Changes in EEG time series before, during and after removing a pain syndrome by applying the psychorelaxation technique are examined for healthy subjects and patients with chronic psychogenic pain disorders connected with disruptions of interrelations between cortex and subcortex on the thalamic and the brain-stem level. The degree of psychorelaxation and decrease of the pain syndromes is estimated as a change in the multifractality degree gained by the wavelet transform modulus maxima method. For the healthy subjects we observe the reliable decrease of the multifractality degree and the enhancement of the anticorrelated dynamics of consecutive EEG values during the pain and their recovery up to the previous values during psychorelaxation. The all healthy subjects notice that the pain syndrome disappears. The analogous dynamics in the multifractality and the improvement of the functional state are observed only for 70% “thalamic”patients. For other 30% patients of the group the multifractality degree remains less than for the healthy subjects. For all the “brain-stem”patients during relaxation the multifractality degree remains high and the singularity spectrum corresponds to both the correlated and anticorrelated dynamics. The study demonstrates that the changes in the multifractality give a good ability to estimate the psychorelaxation efficiency for the healthy and pathological human brain.

Keywords: EEG, Psychorelaxation technique, Multifractal analysis.

1. Introduction

It is well known that bioelectrical activity of the human brain recorded from the head surface as electroencephalography signal (EEG) can be considered as oscillatory processes exhibiting clearly defined variability and having the chaotic and fractal properties [2, 9]. Fractal dynamics of EEG is supported by the form with step-like features and some sort of self-similarity at least stochastically. In other words, on small scales EEG patterns are not identical to the whole signal but the self-similarity remains after averaging by statistically independent samples of the signal. Multifractality of the human brain is found in EEG time series in both healthy and pathologic states [5, 7]. The present work is devoted to the comparative analysis of the multifractality degree in EEG

* Paper included in *Chaotic Systems: Theory and Applications*, C.H. Skiadas and I. Dimotikalis, Eds, World Scientific, pp , 2011.



patterns of normal and pathological brain activities. Impairments connected with anxious phobic disorders are considered as pathology. Chronic pain complaints are specific for patients suffering these disorders. These complaints frequently are not confirmed by medical research and accompanied by emotional disturbances leading to a significant reduction in the level of social functioning [4]. Neural disorders of this type are rather resistant to medicinal treatment. That is why the development of various psychotherapeutic methods is of interest to clinical practice. These methods allow to remove pain symptoms sometimes. One of the methods is psychorelaxation technique [3] in which the psychorelaxation is in switching attention from the pain sense on the perception of color spots arising spontaneously in the state of concentrating on the pain locus with closed eyes. Switching attention from the pain intensity to the color spots is accompanied by decreasing the pain symptoms up to their complete disappearance.

The aim of the work is to estimate the psychorelaxation efficiency for treatment of psychogenic pain in patients with anxious phobic disorders by the method of multifractal analysis. For solving the task we analyze EEG fragments recorded during the perception of psychogenic pain and during its removal by the psychorelaxation technique.

2. Experimental procedure

The scalp EEG data were recorded during 50 minutes with Ag/AgCl electrodes placed at the frontal F3, F4, Fz and occipital O1, O2, Oz sites from 15 healthy subjects and 18 patients with neural impairments connected with anxious phobic disorders. For healthy subjects the pain was evoked by a tactile stimulation on the midpoint between the first and second fingers during 1 minute. The pain was removed by psychorelaxation technique. For patients with psychogenic pain its reduction was performed during 10 - 20 psychorelaxation trials. So, the recordings were obtained for three states: before tactile pain stimulation (10 minutes), during it (20 minutes) and during relaxation (20 minutes) for the healthy subjects and during psychogenic pain and in relaxation state for the patients with neural disorders. The psychorelaxation technique [3] is in switching attention from the pain sense on the perception of color spots arising spontaneously when concentrating on the pain locus with closed eyes. Thus, in the psychorelaxation state the pain sense transformed into a color image by the patient brain. The observed color spots could appear as achromatic (black or grey) colors or chromatic (red, orange, yellow or blue) ones and they could change the color. As attention was shifted from the pain to the color spots and their color was changed, the patient's condition could be improved up to the complete disappearance of pain symptoms.

The data were sampled at a rate 256 samples/sec with a resolution of 12 bits/sample. Then the data were digitally filtered using 1–45 Hz band pass filter. The each state included 256000 samples and it was divided into 20 segments of the duration 50 seconds. After repeated recordings 60 non-artifact segments of



equal duration were randomly chosen from the sets: “before pain”, “during pain” and “during psychorelaxation”.

2. Estimation of EEG multifractality

To estimate multifractal scaling properties of EEG time series we applied the wavelet transform modulus maxima (WTMM) method [1]. The algorithm of the method consists of the following procedures.

1) The continuous wavelet transform of the time series describing the examined signal $x(t)$:

$$W(a, t_0) = \frac{1}{a} \int_{-\infty}^{+\infty} x(t) \psi^* \left(\frac{t - t_0}{a} \right) dt,$$

is used. Here a and t_0 are the scale and space parameters, $\psi((t - t_0)/a)$ is the wavelet function obtained from the basic wavelet $\psi(t)$ by scaling and shifting along the time, symbol * means the complex conjugate. As the basic wavelet we use the complex Morlet wavelet:

$$\psi(t) = \pi^{-1/4} e^{i\omega_0 t} e^{-t^2/2}.$$

The value $\omega = 2\pi$ gives the simple relation between the scale a and the frequency f : $f = 1/a$.

2) A set $L(a)$ of lines of local modulus maxima of the wavelet coefficients is found at each scale a .

3) The partition functions are calculated by the sum of q -powers of the modulus maxima of the wavelet coefficients along the each line at the scales smaller the given value a :

$$Z(q, a) = \sum_{l \in L(a)} \left(\sup_{a^* \leq a} |W(a^*, t_l(a^*))| \right)^q,$$

$t_l(a^*)$ determines the position of the maximum corresponding to the line l at this scale.

4) By the fact that the partition function is $Z(q, a) \sim a^{\tau(q)}$ at $a \rightarrow 0$ [1], the scaling exponent can be extracted as $\tau(q) \sim \log_{10} Z(q, a) / \log_{10} a$.

5) Choosing different values of the power q one can obtain a linear dependence $\tau(q)$ with a constant value of the Hölder exponent $h(q) = d\tau(q)/dq = \text{const}$ for monofractal signals and nonlinear dependence $\tau(q) = qh(q) - D(h)$ with large number of the Hölder exponents for multifractal signals.

6) The singularity spectrum (distribution of the local Hölder exponents) is calculated from the Legendre transform [1]: $D(h) = qh(q) - \tau(q)$.

Using the WWTM algorithm for the different EEG segments we obtain the multifractal parameter, namely, the width of the singularity spectrum $\Delta h = h_{\max} - h_{\min}$, where $h_{\max} = h(q = -5)$ and $h_{\min} = h(q = 5)$ are the maximal and minimal values of the Holder exponent corresponding to minimal and maximal fluctuation of the brain activity, respectively. Smaller Δh indicates that the time series tends to be monofractal and larger Δh testifies the enhancement of multifractality. To examine the differences between the mean values of the parameter obtained for all the segments of different sets of one subject the non-parametric Mann-Whitney test ($p < 0.05$) was applied.

4. Results and discussion

In three different states: background (before the pain stimulation), during the pain stimulation and during psychorelaxation power spectra of EEG for a healthy subject have no significant differences. Alpha activity [7 - 14] Hz dominates.

Multifractal analysis enables us to distinguish the EEGs in the three states. For the all examined electrode sites the width of the singularity spectrum (Δh) decreases during the pain stimulation and recovers up to previous values after pain removing. In the all states $h_{\max} < 0.5$ (Fig. 1), hence, the singularity spectrum corresponds to anticorrelated dynamics of consecutive EEG values.

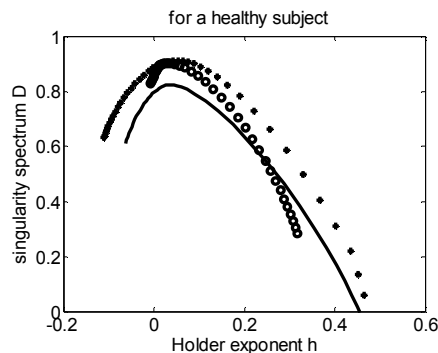


Fig. 1. The examples of singularity spectra of a healthy subject in three functional states (the curve denoted as "*" symbol corresponds the state before the tactile pain stimulation, the curve specified as "o" describes the state during the pain stimulus and the solid line corresponds the psychorelaxation state).

Thus, persistent sequences are characterized by stochastically 'up-down' patterns. The decrease of h_{\max} during the pain stimulation testifies about the enhancement of the anticorrelation degree, so that the signal becomes less smooth and more singular and the randomness of the fluctuations increases.



Therefore, the interval time series tend to become more random during the pain stimulation and recover during relaxation.

The decline of the width of the singularity spectrum during the pain stimulation shows a reduction of nonuniformity of the signal and a fall in the multifractality degree. This fall is due to weak fluctuations (for $q < 0$, $h > 0$), and at strong fluctuations ($q > 0$) the time series become monofractal (uniform by scaling characteristics) and the singularity spectrum transforms into a point ($h = \text{const}$).

In the state of concentration of the attention on the pain sense the all healthy subjects noticed achromatic colors (black or grey) and the short-wavelength colors (blue or green) in the relaxation state. The pain syndrome disappeared. The results agree with the previous data in which each color image caused a specified shift in the psychophysiological state of a subject and determined the presence of psychoemotional stress [6]. In the work [3] it has been revealed that psychotherapeutic influence relieving the stress, is accompanied by a reliable enhancement of colors of the short-wavelength part of visible light.

The patients with neural disorders were separated into two groups accordingly to the classification [8]. For the first group of patients (10 subjects) the disruptions of interrelations between cortex and subcortex on the thalamic level were found in the rest state. It was expressed in changing thalamo – cortical (vertical) and thalamo – thalamic (horizontal) links. Except for alpha activity describing optimal cortico – subcortical relations, the EEG time series of the patients included theta activity specified pathological changes in these relations. During the pain sense the power spectra are characterized by the increase in theta activity. It testifies about an enhancement of unstability of neurodynamic processes. During psychorelaxation theta activity falls in occipital sites of 45% of the group and remains or increases both in frontal and occipital sites (55% of the group). Improvement of psychophysiological state did not correlate with a decrease of theta activity. In other words, there were no reliable changes in power spectra.

During concentrating on the pain locus the patients observed mainly the long-wavelength colors (red, orange, yellow). These colors remained during the psychorelaxation for the 30% patients of the group. The other 70% patients noticed the transformation of color spots to the short-wavelength blue and the complete removal of the pain sense.

Multifractal analysis shows the reliable changes in the electrical brain activity. In all states of the patients with disruptions on the thalamic level the Holder exponent values and the width of the singularity spectrum are less than the values obtained for the healthy subjects. It means that the degree of anticorrelation of persistent sequences of EEG is higher and the randomness of 'up-down' patterns increases. It corresponds to the enhancement of unstability of neurodynamic processes in the brain of the patients as compared with the healthy subjects.

During the pain sensation by the patients the multifractal parameter reduces in all electrode sites. During psychorelaxation the recovery of the Holder exponent values up to the values corresponding to the healthy subjects corresponds to the transformation of color spots to the short-wavelength blue (70% patients of the

group) (Fig. 2a). For other 30% patients the maximal values of the Holder exponent increase weakly during psychorelaxation and they do not reach the values obtained for the healthy subjects (Fig. 2b). The width of the singularity spectrum remains less than for the healthy subjects.

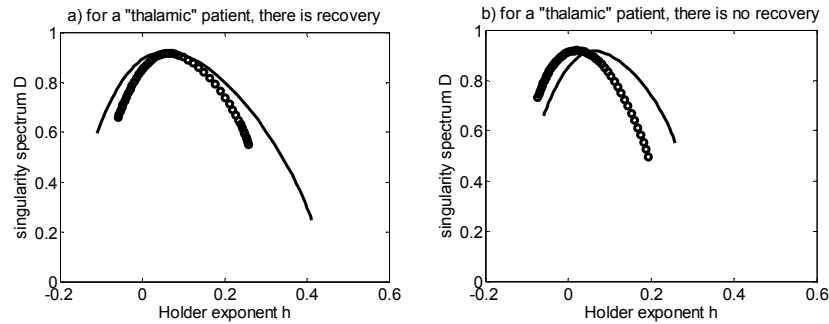


Fig. 2. The examples of singularity spectra of a subject with disruptions of cortico – subcortical links on the thalamic level during the pain sense and during the psychorelaxation (the curve specified as “o” describes the state during the pain sensation and the solid line corresponds to the psychorelaxation state).

Thus, removing pain syndromes for the first group patients corresponds to the fall in the degree of anticorrelation of persistent EEG sequences and decline of the randomness of ‘up–down’ patterns observed in all electrode sites. Hence, the improvement of the functional state testifies about a decline of instability of neurodynamic processes of the brain and optimization of cortico – subcortical links.

For the patients of the second group (8 subjects) disruptions in cortico – subcortical relations manifest on the brain-stem level that leads as a rule to distortion of the stem – cortical and cortico – thalamic (vertical) links. It results to the significant suppression of the alpha component and emergence of the theta activity. It is accompanied by the large instability of neurodynamic processes and amplification of the psychoemotional stress. So, the theta activity is prevalent in the all states of this group of the patients. The spectra decline with increasing frequency remembering the spectrum of the pink noise with its inverse proportionality to frequency ($\sim 1/f$).

The Holder exponent values and the width of the singularity spectrum are larger than the values obtained for the healthy subjects in all studied electrode sites. That is why the multifractality degree of the persistent sequences of EEG far exceeds the degree obtained for the healthy subjects.

During the pain sense the singularity spectrum ($0.1 < h < 0.9$) corresponds to the both correlated dynamics ($h > 0.5$) and anticorrelated dynamics ($h < 0.5$) (Fig.3). During relaxation at strong fluctuations ($q > 0$) the Holder exponent values decline but the multifractality degree remains high and the singularity spectrum corresponds to both ‘up–down’ and ‘up – up’ patterns.

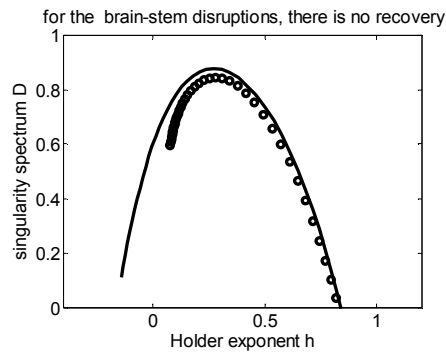


Fig3. The examples of singularity spectra of a subject with neural disorders on the brain stem level during the pain sense and during the psychorelaxation (the curve specified as “o” describes the state during the pain sensation and the solid line corresponds the psychorelaxation state).

The transformation of achromatic dark color spots is not observed for 81% patients. For others 19% achromatic dark colors change into long - wavelength red or orange (distant from colors for the healthy subjects). The both cases are characterized by the similar changes in the singularity spectra and the absence of the improvement of the psychophysiological state.

3. Conclusion

The study demonstrates that power spectra of the patients with neural disorders do not always reflect variations of the psychorelaxation degree. Contrastingly, the changes in the multifractal parameter give a good ability to estimate changes in the healthy and pathological brain activity. Multifractality of the healthy brain is statistically stable as well as stable its neurodynamics. The both cases of unstability in two studied groups of the patients with anxious phobic disorders are connected with deviation (in different sides) of the multifractal parameter from the values specified for the healthy brain. The improvement of the psychophysiological state of the patients during psychorelaxation correlates to approximation of the multifractal parameter to the values obtained for the healthy subjects

References

1. E. Bacry, J. F. Muzy and A. Arneodo. Singularity spectrum of fractal signals: exact results. *J. Statist. Phys.* 70: 635-674, 1993.
2. E. Bullmore, et al. Generic aspects of complexity in brain imaging data and other biological systems. *NeuroImage.* 47. 1125- 1135, 2009.
3. V. A. Ishinova, I. A. Svyatogor, T. N. Reznikova. Features of color reflection in psychogenic pain in patients with somatoform disorders during psychotherapeutic treatment. *Spanish J. of Psychology*, 12, 715-724, 2009.



4. B. D. Karvasarsky. Encyclopedia of psychotherapy. St. Petersburg, Ed. Piter, 2002.
5. D. Popivanov, et. al. Multifractality of decomposed EEG during imaginary and real visual-motor tracking. *Biological Cybernetics* 94: 149-156, 2006.
6. J. Schultz. Das autogene Training. [The Autogenic Training]. 14th Edition. Stuttgart. Ed. Thieme. 1973.
7. I. H. Song and D. S. Lee. Fluctuation Dynamics in Electroencephalogram Time Series. In: Mira J, and Alvarez JR(eds) *Lecture Notes in Computer Sci.* Springer-Verlag, Berlin, pp.195-202, 2005.
8. I. A. Svyatogor. Classification of EEG patterns and their neurophysiological interpretation for desadaptation disorders. *Biologicheskaiia obratnaia sviaz.* 3. 10 -19, 2000.
9. A. M. Wink, et al. Monofractal and multifractal dynamics of low frequency endogenous brain oscillations in functional MRI. *Human Brain Mapping* 29: 791-801, 2008.

Acknowledgements

The author thanks V. A. Ishinova and I. A. Svyatogor, the physicians of St. Petersburg Albrecht Rehabilitation Center and Pavlov Institute of Physiology for their help with EEG recordings.



Detection and Characterization of Cracks in Beams via Chaotic Excitation and Statistical Analysis

Chandresh Dubey and Vikram kapila

Polytechnic Institute of NYU, 6 Metrotech Center, Brooklyn, NY, USA
(E-mail: cdubey01@students.poly.edu, vkapila@poly.edu)

Abstract. A chaotic signal is used to excite a cracked beam and statistical properties of the resulting time series of beam response are analyzed to detect and characterize the crack. For a single degree of freedom (SDOF) approximation of the beam with opening and closing crack, standard deviation, skewness, and kurtosis of are shown to be strongly influenced by crack properties. For a finite element model of a cracked cantilever beam, standard deviation and kurtosis are shown to yield information about the location and severity of crack. Simulation results are experimentally validated.

Keywords: Chaotic excitation, Duffing oscillator, Standard deviation, Skewness.

1 Introduction

Vibration-based damage detection methods are widely used to identify hidden damages in beam and structural components [1,8,14]. In recent years, many researchers have investigated the use of chaotic excitation signals to develop crack detection techniques due to their applicability over a wide frequency spectrum [7,10]. Although the influence of chaotic excitation on statistics-based characterizing parameters has been investigated [7], statistics-based characterizing parameters are significantly influenced by the choice of excitation signal. Recently, statistics-based characterizing parameters were shown to yield satisfactory results in predicting the severity and location of crack in [14], which used a harmonic signal to excite a plate structure in the vicinity of its natural frequency.

In this paper, we consider the chaotic excitation of [10] and statistics-based characterizing parameters examined in [14] for crack detection in beams. Similar to [10], we use a SDOF approximation of a cracked beam. However, unlike the Hausdorff distance used in [10], we consider several statistical characteristics to quantify the crack. Moreover, we extend this framework to the continuous model of structure. In contrast to [10], our proposed technique does not necessitate the reconstruction of the chaotic attractor, instead relevant information is extracted from the time series. We present several alternatives to allow the detection of i) only the presence of crack using one time series data; ii) the location and severity of crack using time series data measured at uniformly distributed locations along the beam span; and iii) approximate location and severity of crack using only two time series data.



2 Input Signal

Although a variety of input signals has been studied for vibration-based crack detection in the literature [1,7,8,10,14], in this paper, we report on the effectiveness of the chaotic solution of a forced Duffing's equation, which can be expressed as a set of three first-order ordinary differential equations

$$\dot{y}_1 = y_2, \quad \dot{y}_2 = F \cos(y_3) + k_1 y_1 - k_2 y_1^3 - d y_2, \quad \dot{y}_3 = \omega, \quad (1)$$

where d , k_1 , and k_2 correspond to some physical parameters of the Duffing oscillator, F is the amplitude of the sinusoid driving the oscillator, and ω is the angular frequency of the forcing sinusoid. Setting the parameters to $d = 0.05$, $k_1 = 0$, $k_2 = 1$, $F = 7.5$, and $\omega = 1$ with initial values of $y_1(0) = 0$, $y_2(0) = 0.4$, and $y_3(0) = 0$, equation (1) exhibits a chaotic behavior [10].

3 Modeling of a Cracked Beam as a SDOF System with Displacement Input

Following [10], a cracked beam is modeled as a SDOF piecewise linear spring-mass-damper system which behaves nonlinearly due to the presence of crack as the system stiffness changes with opening/closing of crack. For the closed crack case, the effective stiffness is assumed to be k , which reduces to $k_s = k - \Delta k$ for the open crack case where Δk is related to the depth of the crack. For a SDOF model with a relatively small crack, it follows that $\frac{\Delta k}{k} = \frac{a}{h}$, for $a \ll h$ [2,10]. Next, we consider that the y_1 solution of (1) is used as an excitation input applied at the base of the SDOF system as a displacement. The equations of motion for this piecewise continuous SDOF system are [10]

$$\begin{aligned} M\ddot{x}_1 + c\dot{x}_1 + kx_1 &= cy_1 + ky_1, & \text{for } x_1 \geq 0, \\ M\ddot{x}_1 + c\dot{x}_1 + k_s x_1 &= cy_1 + k_s y_1, & \text{for } x_1 < 0, \end{aligned} \quad (2)$$

where M is the mass of cantilever beam, c is the damping coefficient, and x_1 is the displacement of beam from the undeformed position.

4 SDOF Results

We subject the SDOF model of (2) to the chaotic excitation y_1 resulting from (1). The resulting time series output is recorded and used to evaluate the values of statistical parameters such as standard deviation (σ), skewness, and kurtosis [12]. This process is repeated for varying crack depths. The results are graphed and examined to determine the existence of any trends that may indicate the presence and severity of crack. The physical parameters of the problem data used in our simulations are as follows: mass $m = 0.18$ kg, nominal stiffness $k = 295$ N/m, and damping $c = 0.03$ Ns/m. We also consider one stiffness value above and one below the nominal stiffness. This allows us to investigate how the proposed methodology may work on randomly selected specimen since in real world situations the natural frequency of specimen may



not be known *a priori*. The results of our analysis are summarized in Figure 1. All three statistical characterizing parameters, namely σ , skewness, and kurtosis exhibit a continuous growth with increasing crack depth and this trend is observed for three test structures of different natural frequencies, each excited with the same chaotic input. This result indicates that we do not need to have the exact knowledge of the natural frequency of the structure that is being investigated for crack detection. This of course stems from the fact that the chaotic excitation signal possesses a broad frequency content.

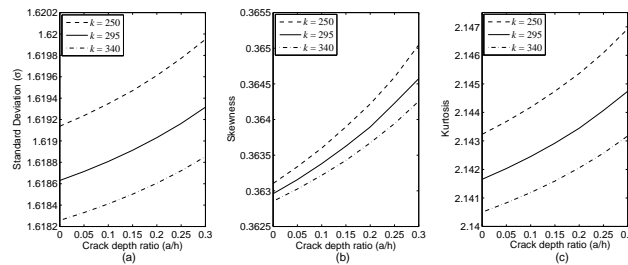


Fig. 1. SDOF results of statistical characterizing parameters for chaotic input. Crack depth ratio versus (a) Standard deviation, (b) Skewness, and (c) Kurtosis.

5 Continuous Model

We now extend the results of section 4 to the continuous model case. To do so, as in [11,13], we consider a continuous model of the dynamical behavior of the beam with a surface crack in two parts. Specifically, when the beam moves away from the neutral position so that the crack remains closed, then the beam behaves as a typical continuous beam [4,11,13]. However, when the beam moves in the other direction from the neutral position, causing the crack to be opened, the resulting dynamics require the modeling of crack with a rotational spring whose stiffness is related to the crack depth [3,4,11,13].

Next, we used the ANSYS software [6] to simulate the dynamics of a cracked beam under external excitation. We modeled the beam as a 2-D elastic object using a *beam3* element [6] which has tension, compression, and bending capabilities. The crack is simulated by inserting a torsional spring at the location of the crack and using the mathematical model described in [3,4,11,13]. The torsional spring is modeled using a *combin14* element [6] which is a spring-damper element used in 1-D, 2-D, and 3-D applications. In our FE model, we used the *combin14* element as a pure spring with 1-D (i.e., torsional) stiffness since the model of [3,4,11,13] does not consider damping. The physical characteristics of the beam used in our FE model are as follows: material–Plexiglass, length–500 mm, width–50 mm, thickness–6 mm, modulus of elasticity–3300 MPa, density–1190 kg/m³, and Poisson’s ratio–0.35. This FE model was validated [4] by comparing the natural frequencies



resulting from the FE simulations versus the natural frequencies computed in Matlab for the dynamic model of [4,11,13].

Next, we subject the FE model to a base displacement using the time series y_1 of (1). In particular, using MATLAB, we simulate (1) and save 15,000 time steps of y_1 time series, which is used as an input to excite the FE model. The FE simulation is used to produce and record spatio-temporal responses for each node (corresponding to discretized locations along the beam span). The resulting data is imported in MATLAB for a detailed time series analysis, whose results are grouped in two parts as explained below.

We first analyze the beam tip time series data to detect the presence of any cracks along the beam span. Figure 2 provides plots of the normalized crack depth a/h versus σ and kurtosis, both of which exhibit a growth trend with increasing crack depth. However, increasing crack depth produces a significantly greater growth in kurtosis compared to σ . Moreover, note that the rate of growth in σ and kurtosis increases when the crack is near the fixed end of the beam and decreases as the crack location shifts to the free end of the beam. Finally, a sound beam starts out with a nominal kurtosis value (in our example, 2.056) and the presence of crack anywhere along the beam causes the kurtosis value to increase indicating the presence of crack. However, it is not possible to determine either the crack depth or crack location using only the beam tip response analysis.

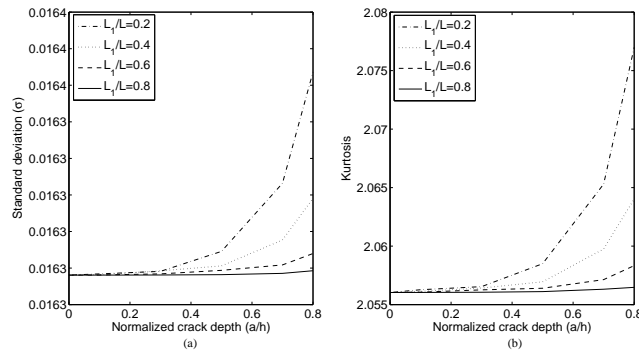


Fig. 2. Variation in standard deviation σ and kurtosis with crack severity for different crack locations

Next, we use the time series data of the beam response along its span to develop a method to predict the severity and approximate location of the crack on the beam surface. We conduct a FE simulation of a beam with a known crack depth and a known crack location. As before, we use the time series y_1 of (1) as the input excitation and record the time series of beam response at every 5 mm distance along the beam length. This simulation is repeated for three different crack locations to test the consistency of our results. Next, σ , skewness, and kurtosis are computed for the time series at each location for each crack depth and are plotted in Figures 3 and 4 for



crack locations of $L_1 = 0.2L$ and $L_1 = 0.6L$, respectively. The σ versus normalized beam length plot shows that the slope of the resulting curve increases with increasing crack depth, i.e., the beam without crack has the smallest slope and the beam with the most severe crack has the largest slope. Moreover, the slope of each curve changes abruptly at the location of crack; thus this behavior can be used to determine the approximate location of crack. A careful examination of the skewness plot reveals that the various curves corresponding to different crack depths do not follow the kind of ordering observed in the standard deviation σ plots. Thus we will no longer consider the skewness plots. Next, the kurtosis plots are found to behave in a similar manner as σ plots and can be used to predict crack location and severity. In fact, the kurtosis plots exhibit an order of magnitude larger changes compared to standard deviation σ , rendering them more suitable for detecting crack location and severity.

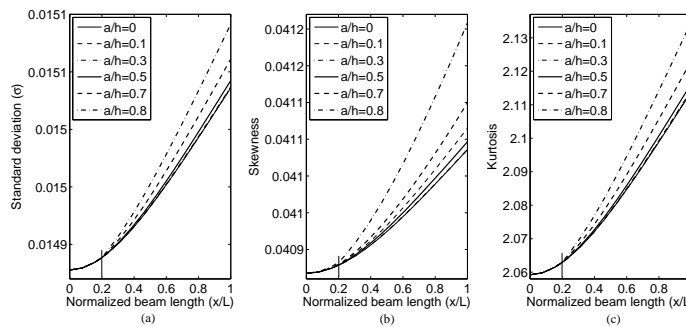


Fig. 3. Variation in standard deviation σ , skewness, and kurtosis with varying crack severity for a crack located at $0.2L$

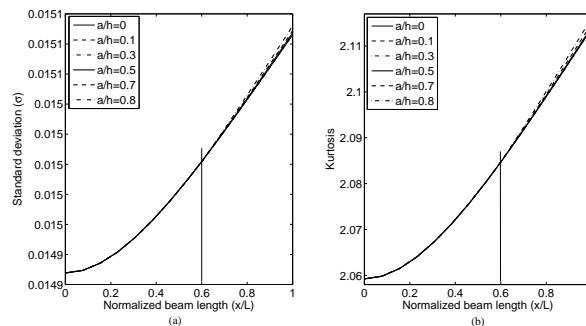


Fig. 4. Variation in standard deviation σ and kurtosis with varying crack severity for a crack located at $0.6L$

As seen above, we can detect the severity and location of a crack provided that the spatio-temporal data is recorded for a series of locations along the beam length. An examination of the kurtosis plots of Figures 3–4 suggests one approach to overcome this problem. For each crack depth and each crack

location, the kurtosis yields a distinct slope past the crack location. For example, Figure 5(a) shows the variation of kurtosis slope versus the crack depth, thus yielding *constant crack location curves*. Similarly, Figure 5(b) shows the variation of kurtosis slope versus the crack location, thus yielding *constant crack depth curves*. To use the diagrams in Figure 5, we record only two time series along the beam span, preferably near the beam tip. The recorded time series can be analyzed to obtain the corresponding kurtosis values. Furthermore, the knowledge of location where the time series data was recorded allows us to compute the kurtosis slope. Next, superimposing the computed kurtosis slope value on Figure 5(a) yields the approximate crack location whereas doing the same on Figure 5(b) yields the approximate crack depth. Having obtained the approximate knowledge of the crack location, we can focus on either collecting additional time series data in the identified region of crack or we can make efficient use of NDT techniques by focusing only on the identified region of crack.

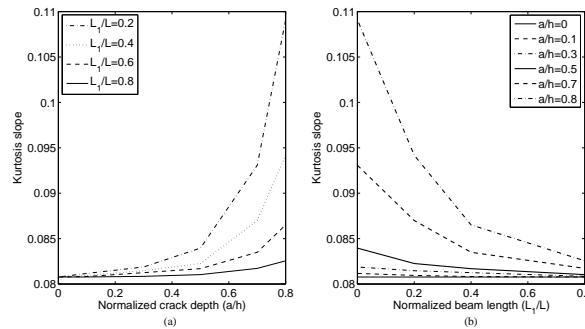


Fig. 5. (a) Kurtosis slope versus normalized crack depth for fixed crack locations and (b) kurtosis slope versus normalized length for fixed crack depths

6 Experimental Verification

A schematic of the experimental setup used is given in Figure 6. An aluminum base holds the shaker (Brüel & Kjær Type 4810). To produce a base excitation, a test specimen is clamped on shaker. An accelerometer (Omega ACC 103) is mounted at the tip of the specimen using mounting bee wax. Our software environment consists of Matlab, Simulink, and Real Time Workshop in which the Duffing's chaotic oscillator is propagated to obtain the time series corresponding to the y_1 signals of (1). Next, an analog output block in the Simulink program outputs the y_1 signal to a digital to analog converter of Quanser's Q4 data acquisition and control board which in turn is fed to a 12 volt amplifier (Kenwood KAC-8202) to drive the shaker. The accelerometer output is processed by an amplifier (Omega ACC PSI) and interfaced to an analog to digital converter of the Q4 board for feedback to the Simulink program. Properties of the specimen used in our experiments are same as in Section 5. To emulate a fine hair crack, we used a 0.1 mm



saw to introduce cracks of several different desired depths. For specimen of different crack depth, all located at $L_1 = 0.2L = 100$ mm from fixed end, the accelerometer measurement is recorded and used to produce the output response time series, which is used to perform our analysis. A total of six specimens were prepared with crack depth varying from 0% to 50% of the thickness. In all the specimen, saw crack was introduced on the top surface to match with the simulation condition. The time series data obtained from the accelerometer suffered from general sensor errors (dc offset and ramp bias), causing the raw time series data to be unusable for further analysis. We used the Wavelet transformation toolbox [5] of MATLAB, to filter the raw time series data and remove the errors [4]. The corrected time series data [4] is used to compute various statistical characterizing parameters. Figures 7 provides the variation in standard deviation, skewness, and kurtosis, versus the crack depth for the corrected time series data. Note that these three statistical characterizing parameters show an increasing trend with increasing crack depth validating the predictions of our numerical study in Section 4 for SDOF case and in Section 5 for the continuous beam case when only tip displacement measurement is used. Although the plots obtained from the experimental data are not as smooth as the ones resulting from numerical simulation, this may be the result of inaccuracies resulting from sample preparation or a variety of experimental errors [4].

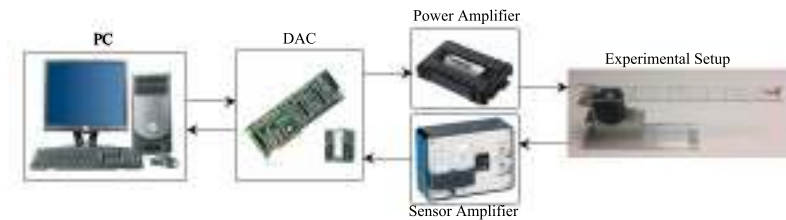


Fig. 6. Experimental setup

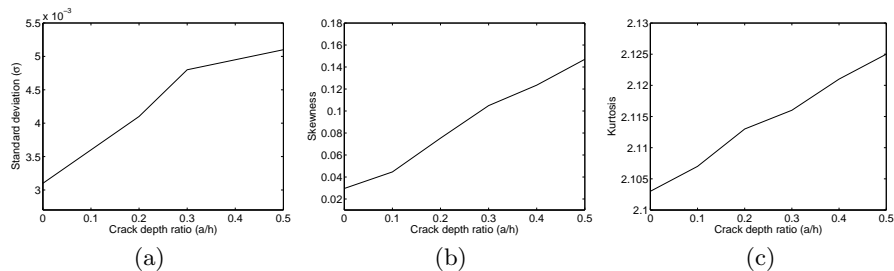


Fig. 7. (a) Standard deviation (σ), (b) Skewness, and (c) Kurtosis for different crack depths at $L_1 = 0.2L$

7 Conclusion

In this paper, to detect and characterize a crack in a beam, we considered a SDOF and a FE model of the beam excited by a chaotic input, as displace-



ment at the base. We showed that for the SDOF model, crack severity can be easily and consistently predicted by using standard deviation, skewness, and kurtosis of the time series data. Moreover, for the FE model, we showed that standard deviation and kurtosis exhibit trends that can be used to predict crack location and crack depth. Finally, the simulation results were validated experimentally.

Acknowledgments

This work is supported in part by the National Science Foundation under an RET Site grant 0807286, a GK-12 Fellows grant 0741714, and the NY Space Grant Consortium under grant 48240-7887.

References

- 1.U. Andreausa, P. Casinib, and F. Vestronia. Non-linear dynamics of a cracked cantilever beam under harmonic excitation. *International Journal of Non-Linear Mechanics*, 42:566–575, 2007.
- 2.N. Bouraou and L. Gelman. Theoretical bases of free oscillation method for acoustical non-destructive testing. *Proceedings of Noise Conference, The Pennsylvania State University*, 519–524, 1997.
- 3.Y. Bammios, E. Douka, and A. Trochidis. Crack identification in beam structures using mechanical impedance. *Journal of Sound and Vibration*, 256(2):287–297, 2002.
- 4.C. Dubey. Damage detection in beam structures using chaotic excitation. Master’s Thesis at Polytechnic Institute of NYU, New York, 2010.
- 5.A. Jensen and I. CH. Anders. *Ripples in Mathematics: The Discrete Wavelet Transform*. New York, 2001. Cambridge University Press.
- 6.S. Moaveni. *Finite Element Analysis Theory and Application with ANSYS*. Upper Saddle River, NJ, 2007. Prentice Hall.
- 7.J. M. Nichols, S. T. Trickey, M. D. Todd, and L. N. Virgin. Structural health monitoring through chaotic interrogation. *Meccanica*, 38:239–250, 2003.
- 8.S. Orhan. Analysis of free and forced vibration of a cracked cantilever beam. *NDT&E International*, 40:443–450, 2007.
- 9.Z. K. Peng, Z. Q. Lang, and S. A. Billings. Crack detection using nonlinear output frequency response functions. *Journal of Sound and Vibration*, 301:777–788, 2007.
- 10.J. Ryue and P. R. White. The detection of crack in beams using chaotic excitations. *Journal of Sound and Vibration*, 307:627–638, 2007.
- 11.P. F. Rizos, N. Aspragathos, and A. D. Dimarogonas. Identification of crack location and magnitude in a cantilever beam from the vibration modes. *Journal of Sound and Vibration*, 138(3):381–388, 1990.
- 12.M. Spiegel and L. Stephens. *Statistics*. New York, NY, 2008. McGraw-Hill.
- 13.M. Taghi, B. Vakil, M. Peimani, M. H. Sadeghi, and M. M. Ettefagh. Crack detection in beam like structures using genetic algorithms. *Applied Soft Computing*, 8:1150–1160, 2008.
- 14.I. Trendafilova and E. Manoach. Vibration-based damage detection in plates by using time series analysis. *Mechanical Systems and Signal processing*, 22:1092–1106, 2008.



Wave Fractal Dimension as a Tool in Detecting Cracks in Beam Structures

Chandresh Dubey and Vikram kapila

Polytechnic Institute of NYU, 6 Metrotech Center, Brooklyn, New York
(E-mail: cdubey01@students.poly.edu, vkapila@poly.edu)

Abstract. A chaotic signal is used to excite a cracked beam and wave fractal dimension of the resulting time series and power spectrum are analyzed to detect and characterize the crack. For a single degree of freedom (SDOF) approximation of the cracked beam, the wave fractal dimension analysis reveals its ability to consistently and accurately predict crack severity. For a finite element simulation of the cracked cantilever beam, an analysis of spatio-temporal response using wave fractal dimension in frequency domain reveals distinctive variation vis-à-vis crack location and severity. Simulation results are experimentally validated.

Keywords: Chaotic excitation, Chen's oscillator, Wave fractal dimension.

1 Introduction

Vibration-based methods for crack detection in beam type structures continue to attract intense attention from researchers. To quantify the crack depth and to detect crack location, vibration-based crack detection methods employ a variety of characterizing parameters, such as natural frequency [8], mode shape [13], mechanical impedance [2], statistical parameters [16], etc. In recent research, wave fractal dimension, originally introduced by Katz [9] to characterize biological signals, has been used to detect the severity and location of crack in beam [4] and plate structures [5].

Since the past decade, progress in chaos theory has led several researchers to consider the use of chaotic excitation in vibration-based crack detection [11,12]. A majority of these efforts necessitate the reconstruction of a chaotic attractor from the time series data corresponding to the vibration response of the structure [11,12]. Unfortunately, the reconstruction of a chaotic attractor is often tedious and may not always yield satisfactory results for crack detection even in the SDOF approximation case. To detect and characterize cracks, the current chaos-based crack detection methods use a variety of chaos and statistics-based parameters, such as correlation dimension [12], Hausdorff distance [12], average local attractor variance ratio [11], etc. In this paper, we study the use of wave fractal dimension as a characterizing parameters to predict the severity and location of a crack in a beam that is made to vibrate using a chaotic input.



2 Beam Excitation Input

In [3] we considered three methods to excite the cracked beam: a non-zero initial condition, a harmonic input, and the chaotic solution of autonomous dissipative flow type Chen's attractor [14]. Due to space constraints, here we report on the results corresponding to the use of chaotic signal as an input excitation force to vibrate a cracked beam. The Chen's system in state space form is expressed as

$$\dot{y}_1 = a_1(y_2 - y_1), \quad \dot{y}_2 = (a_3 - a_1)y_1 - y_1y_3 + a_3y_2, \quad \dot{y}_3 = y_1y_2 - a_2y_3, \quad (1)$$

where a_1 , a_2 , and a_3 are constant parameters. Setting the parameters to $a_1 = 35$, $a_2 = 3$, and $a_3 = 28$, with initial values of $y_1(0) = -10$, $y_2(0) = 0$, and $y_3(0) = 37$, equation (1) exhibits a chaotic behavior [3,14] and the solution y_1 is expected to be non-periodic. See [3] for our reasons to restrict consideration to Chen's system.

3 Wave Fractal Dimension

Waveforms are common patterns that arise frequently in scientific and engineering phenomena. The concept of wave fractal dimension [9] is used to differentiate one waveform from another. For waveforms, produced using a collection of ordered point pairs (x_i, y_i) , $i = 1, \dots, n$, the total length, L , is simply the sum of the distances between successive points, i.e., $L = \sum_{i=1}^{n-1} \sqrt{(x_{i+1} - x_i)^2 + (y_{i+1} - y_i)^2}$. Moreover, the diameter d of a waveform is considered to be the farthest distance between the starting point (corresponding to $n = 1$) and some other point (corresponding to $n = i$, $i = 2, \dots, n$), of the waveform, i.e., $d = \max_{i=2, \dots, n} \sqrt{(x_i - x_1)^2 + (y_i - y_1)^2}$. Next, by expressing the length of a waveform L and its diameter d in a standard unit, which is taken to be the average step α of the waveform, the wave fractal dimension can be expressed as [9]

$$D = \log(L/\alpha) / \log(d/\alpha) = \frac{\log(n)}{\log(n) + \log(d/L)}, \quad (2)$$

where $n = L/\alpha$, denotes the number of steps in the waveform. We use (2) to estimate the wave fractal dimension.

4 Modeling of a Cracked Beam as a SDOF System with Force Input

Following [1,12], a cracked beam is modeled as a SDOF switched system which emulates the opening and closing of the surface crack by switching the



effective stiffness $k_s = k - \Delta k$, where k is the stiffness of the beam without crack, k_s is stiffness during stretching and Δk is stiffness difference. For a SDOF model with a relatively small crack, the ratio of Δk to k is equal to the ratio of the crack depth a to the thickness h of the beam [1,12]. Next, we consider that the y_1 solution of (1) is applied as a force to the mass of the SDOF system. The equations of motion for this piecewise continuous SDOF system are

$$\begin{aligned} M\ddot{x} + c\dot{x} + kx &= F(t), & \text{for } x \geq 0, \\ M\ddot{x} + c\dot{x} + k_s x &= F(t), & \text{for } x < 0, \end{aligned} \quad (3)$$

where M is the mass of the cantilever beam, c is the damping coefficient, and x is the displacement of the beam. The physical parameters of the problem data used in our simulations are as follows: mass $m = 0.18$ kg, nominal stiffness $k = 295$ N/m, and damping $c = 0.03$ Ns/m.

5 SDOF Results

We now consider the application of the chaotic forcing input of (1) to vibrate the SDOF model for various values of crack depths. The resulting time series plots (see Figure 3.11 of [3]) are used to compute the corresponding wave fractal dimension. Figure 1(a) plots normalized crack depth versus the wave fractal dimension, showing that the wave fractal dimension monotonically increases with increasing crack depth. Since wave fractal dimension is a characteristic of the waveform only, we consider the wave fractal dimension analysis of the time series of [3] in frequency domain. Using the Fast Fourier Transform (FFT) [7] technique, we convert the time domain data of [3] to frequency domain (see Figure 3.13 of [3]), producing the power spectrum of the response of the SDOF cracked beam. The power spectrum reveals that the portion of FFT in the vicinity of beam's natural frequency ω_n experiences significant changes. Thus, we concentrate in the neighborhood of ω_n as our window for computing the wave fractal dimension. Using this technique, in Figure 1(b), we plot normalized crack depth versus the wave fractal dimension for the windowed waveforms of Figure 3.13 of [3]. The wave fractal dimension is seen to monotonically increase with increasing crack depth and this curve exhibits a significant rate of change. Thus, in the following analysis, we use the wave fractal dimension of power spectrum as a natural choice for crack detection and crack characterization.

6 Continuous Model

We now extend the results of section 5 to the continuous model case. To do so, as in [13,15], we consider a continuous model of the dynamical behavior of the beam with a surface crack in two parts. Specifically, when the beam

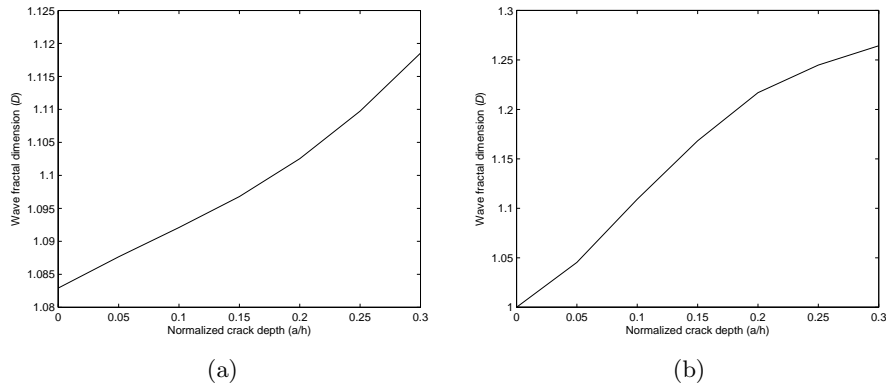


Fig. 1. (a) Time domain and (b) Frequency domain change of the wave fractal dimension with normalized crack depth for chaotic forcing input

moves away from the neutral position so that the crack remains closed, then the beam behaves as a typical continuous beam [3,13,15]. However, when the beam moves in the other direction from the neutral position, causing the crack to open, the resulting dynamics require the modeling of crack with a rotational spring whose stiffness is related to the crack depth [2,3,13,15].

Next, we used the ANSYS software [10] to simulate the dynamics of a cracked beam under external excitation. We modeled the beam as a 2-D elastic object using a *beam3* element [10] which has tension, compression, and bending capabilities. The crack is simulated by inserting a torsional spring at the location of the crack and using the mathematical model described in [2,3,13,15]. The torsional spring is modeled using a *combin14* element [10] which is a spring-damper element used in 1-D, 2-D, and 3-D applications. In our FE model, we used the *combin14* element as a pure spring with 1-D (i.e., torsional) stiffness since the model of [2,3,13,15] does not consider damping. The physical characteristics of the beam used in our FE model are as follows: material–Plexiglass, length–500 mm, width–50 mm, thickness–6 mm, modulus of elasticity–3300 MPa, density–1190 kg/m³, and Poisson’s ratio–0.35. This FE model was validated [3] by comparing the natural frequencies resulting from the FE simulations versus the natural frequencies computed in Matlab for the dynamic model of [3,13,15].

Next, we apply force input to the FE model using the time series y_1 of (1). In particular, using MATLAB, we simulate (1) and save 15,000 time steps of y_1 time series, which is applied as force input at 40 mm from the fixed end in ANSYS. The FE simulation is used to produce and record spatio-temporal responses for each node (corresponding to discretized locations along the beam span). The resulting data is imported in MATLAB for a detailed wave fractal dimension analysis, whose results are grouped in two parts as explained below.

We first analyze the beam tip displacement power spectrum data to detect the presence of any cracks along the beam span. Figure 2 provides plots of the normalized crack depth a/h versus wave fractal dimension for a crack located at $L_1 = 0.2L$ and, alternatively, at $L_1 = 0.4L$. We term these curves as *uniform crack location curves*. We observe that a beam without a crack yields a wave fractal dimension of 1.1205, and wave fractal dimension above this nominal value indicates presence of a crack in the beam. However, it is not possible to determine either the crack depth or crack location using only the beam tip response analysis.

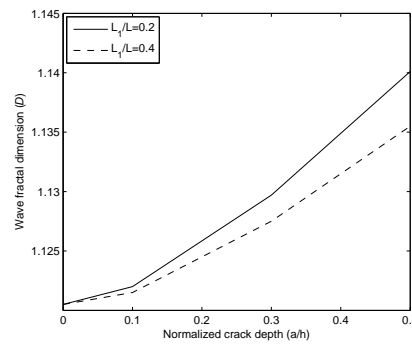


Fig. 2. Wave fractal dimension versus normalized crack depth–uniform crack location curves for $L_1 = 0.2L$ and $L_1 = 0.4L$

Next, to predict the severity and approximate location of the crack on the beam surface, we record the time series data of the beam response along its span for chaotic forcing input. Using the FFT, the time series data is converted to frequency domain. The resulting power spectrum plot is analyzed to identify a suitable window for computing the wave fractal dimension. Throughout this analysis, the frequency window used for computing the wave fractal dimension is kept fixed for all crack depths considered. Figure 3(a) plots wave fractal dimension against normalized beam length for cracks of various severity located at $L_1 = 0.2L$. These *uniform crack depth curves* yield the same wave fractal dimension till the crack location and their slopes change abruptly at the location of crack. In fact, past the crack location, the uniform crack depth curves exhibits a larger slope for a larger crack depth. Figure 3(b) shows similar behavior for crack location, $L_1 = 0.4L$. The abrupt split in uniform crack depth curves at crack location and their increasing slope with increasing crack depth can be used to establish both the severity and location of crack.

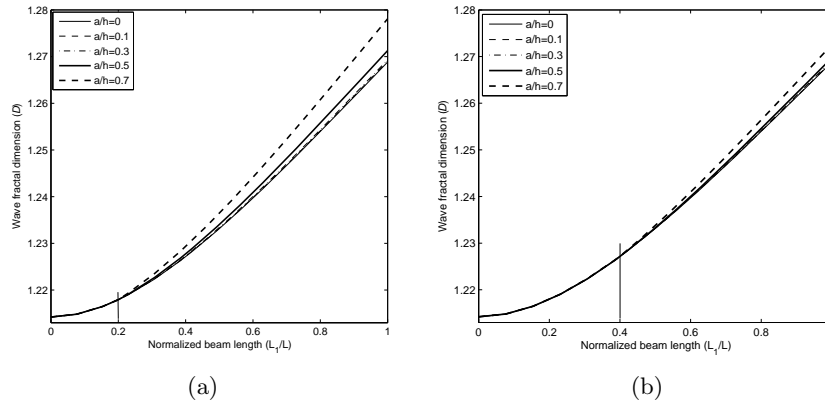


Fig. 3. Wave fractal dimension versus normalized beam length–uniform crack depth curves for (a) $L_1 = 0.2L$ and (b) $L_1 = 0.4L$

7 Experimental Verification

A schematic of the experimental setup used is given in Figure 4. An aluminum base holds the shaker (Brüel & Kjær Type 4810). To produce a base excitation, a test specimen is clamped on shaker. An accelerometer (Omega ACC 103) is mounted at the tip of the specimen using mounting bee wax. Our software environment consists of Matlab, Simulink, and Real Time Workshop in which the Chen’s chaotic oscillator is propagated to obtain the time series corresponding to the y_1 signals of (1). Next, an analog output block in the Simulink program outputs the y_1 signal to a digital to analog converter of Quanser’s Q4 data acquisition and control board which in turn is fed to a 12 volt amplifier (Kenwood KAC-8202) to drive the shaker. The accelerometer output is processed by an amplifier (Omega ACC PSI) and interfaced to an analog to digital converter of the Q4 board for feedback to the Simulink program. Properties of the specimen used in our experiments are same as in Section 6. To emulate a fine hair crack, we used a 0.1 mm saw to introduce cracks of several different desired depths. For specimen of different crack depth, all located at $L_1 = 0.2L = 100$ mm from fixed end, the accelerometer measurement is recorded and used to produce the output response time series, which is used to perform our analysis. A total of six specimens were prepared with crack depth varying from 0% to 50% of the thickness. In all the specimen, saw crack was introduced on the top surface to match with the simulation condition.

The time series data obtained from the accelerometer suffered from general sensor errors (dc offset and ramp bias), causing the raw time series data to be unusable for further analysis. We used the Wavelet transformation toolbox [6] of MATLAB, to filter the raw time series data and remove the errors [3]. The corrected time series data [3] is converted to frequency domain

and used to compute wave fractal dimension. Figure 5 provides the variation in wave fractal dimension versus the crack depth for the corrected power spectrum data. Note that the wave fractal dimension shows an increasing trend with increasing crack depth validating the predictions of our numerical study in Section 5 for SDOF case and in Section 6 for the continuous beam case when only tip displacement measurement is used. Although the plots obtained from the experimental data are not as smooth as the ones resulting from numerical simulation, this may be the result of inaccuracies resulting from sample preparation or a variety of experimental errors [3].

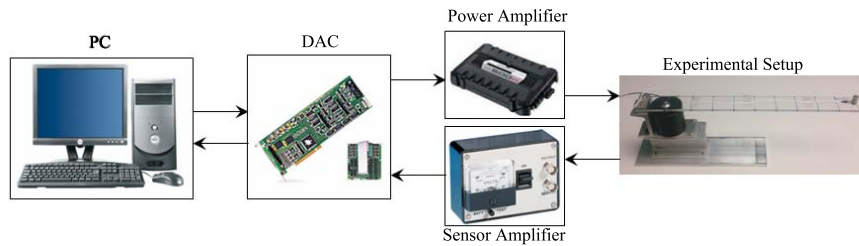


Fig. 4. Experimental setup

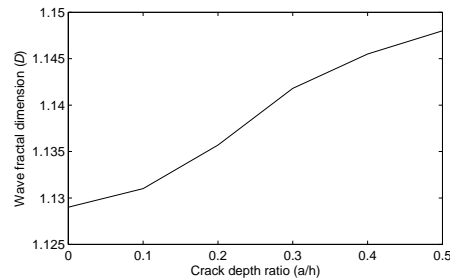


Fig. 5. Frequency domain change of wave fractal dimension with normalized crack depth at $L_1 = 0.2L$

8 Conclusion

In this paper, to detect and characterize a crack in a beam, we considered a SDOF and a FE model of the beam excited by a chaotic force input. We showed that for the SDOF model, crack severity can be easily and consistently predicted by using wave fractal dimension of power spectrum of time series data. Moreover, for the FE model, we showed that wave fractal dimension



exhibits a trend that can be used to predict crack location and crack depth. Finally, the simulation results were validated experimentally.

Acknowledgments

This work is supported in part by the National Science Foundation under an RET Site grant 0807286, a GK-12 Fellows grant 0741714, and the NY Space Grant Consortium under grant 48240-7887.

References

- 1.N. Bouraou and L. Gelman. Theoretical bases of free oscillation method for acoustical non-destructive testing. *Proceedings of Noise Conference, The Pennsylvania State University*, 519–524, 1997.
- 2.Y. Bammios, E. Douka, and A. Trochidis. Crack identification in beam structures using mechanical impedance. *Journal of Sound and Vibration*, 256(2):287–297, 2002.
- 3.C. Dubey. Damage detection in beam structures using chaotic excitation. Master’s Thesis at Polytechnic Institute of NYU, New York, 2010.
- 4.L. J. Hadjileontiadis, E. Douka, and A. Trochidis. Fractal dimension analysis for crack identification in beam structures. *Mechanical Systems and Signal processing*, vol. 19, pp. 659–674. 2005.
- 5.L. J. Hadjileontiadis and E. Douka. Crack detection in plates using fractal dimension. *Engineering Structures*, vol. 29, pp. 1612–1625. 2007.
- 6.A. Jensen and la. CH. Anders. Ripples in Mathematics: The Discrete Wavelet Transform. New York, 2001. Cambridge University Press.
- 7.J. F. James. A Student’s Guide to Fourier Transforms: With Applications in Physics and Engineering. New York, NY, 2003. Springer Verlag.
- 8.J. T. Kim and N. Stubbs. Crack detection in beam type structures using frequency data. *Journal of Sound and Vibration*, vol. 259(1), pp. 145–160. 2003.
- 9.M. J. Katz. Fractals and the analysis of waveforms. *Computers in Biology and Medicine*, vol. 18(3), pp. 145–156. 1998.
- 10.S. Moaveni. Finite Element Analysis Theory and Application with ANSYS. Upper Saddle River, NJ, 2007. Prentice Hall.
- 11.J. M. Nichols, S. T. Trickey, M. D. Todd, and L. N. Virgin. Structural health monitoring through chaotic interrogation. *Meccanica*, 38:239–250, 2003.
- 12.J. Ryue and P. R. White. The detection of crack in beams using chaotic excitations. *Journal of Sound and Vibration*, 307:627–638, 2007.
- 13.P. F. Rizos, N. Aspragathos, and A. D. Dimarogonas. Identification of crack location and magnitude in a cantilever beam from the vibration modes. *Journal of Sound and Vibration*, 138(3):381–388, 1990.
- 14.J. C. Sprott. Chaos and Time-Series Analysis. New York, NY, 2003. Oxford University Press.
- 15.M. Taghi, B. Vakil, M. Peimani, M. H. Sadeghi, and M. M. Ettefagh. Crack detection in beam like structures using genetic algorithms. *Applied Soft Computing*, 8:1150–1160, 2008.
- 16.I. Trendafilova and E. Manoach. Vibration-based damage detection in plates by using time series analysis. *Mechanical Systems and Signal processing*, 22:1092–1106, 2008.



Modeling of Baltic Sea ecosystem using POP model

Lidia Dzierzbicka, Jaromir Jakacki, Maciej Janecki, Artur Nowicki

Institute of Oceanology Polish Academy of Sciences, Sopot, Poland
E-mail: dzierzb@iopan.gda.pl

Abstract: A 3D ecosystem model of Baltic Sea is presented, and model output is compared with field data from the southern Baltic Sea. This model is used to estimate the annual phytoplankton biomass under circulation and solar radiation forcing conditions. The marine ecosystem model consists of a set of equations. There are all of the same general form, i.e. equations of the diffusion type (a second-order partial differential equation), expressing changes in any state variable. The marine ecosystem model is coupled to the three-dimensional, time-dependent hydrodynamical model, POPCICE for the Baltic Sea. The POPCICE model consists of Parallel Ocean Program (POP) and Community Ice Code (CICE). Both models are from Los Alamos National Laboratory (LANL). POPCICE was forced using European Centre for Medium-Range Weather Forecasts (ECMWF) data. The POPCICE model provides the velocities, temperature and salinity on a temporal and spatial scale that resolves the atmospherically induced variability mentioned above. The results of the simulations are presented for one year (2004) for the whole of Baltic Sea. Model generally in good agreement with field data. The study was financially supported by the Polish State Committee of Scientific Research (grants: No N N305 111636, N N306 353239) and ECOOP IP WP 10.1.3 Project.

Keywords: 3D ecosystem model, Baltic Sea, phytoplankton, nutrient, temperature

1. Introduction

The Baltic Sea is a semi-enclosed shelf sea bounded by the Scandinavian Peninsula in the north and east, the Jutland Peninsula in the west and continental Europe in the south. The brackish nature of the Baltic, in which salinity decreases in a north-easterly direction, is due to the combination of the high river discharge and the limited inflows of salty water from North Sea. The Baltic Sea run off drains a catchment area which is approximately four times bigger than the sea itself. Major part of catchment area, especially in the continental part, intensive agriculture is practiced. This means that high loads of nutrients and organic matter eventually could reach the Baltic, making this sea one of the most productive marine ecosystems in the world [5].

The numerous threats and natural disasters elicited by changes in the environment have persuaded experts to radically intensify ecological investigations and forecasts on a regional and global scale. A key part in these changes is played by marine ecosystems, especially the organic matter production processes occurring in them. During the last four decades, a way of solving these problems has been developed using numerical methods describing the bioproductivity of marine basins. Mathematical models of ecosystems can also be used as tools for forecasting and evaluating the influence of human activities, or for analysing future changes to an ecosystem that may take place under the influence of external factors [2].



The marine system model consists of two parts: hydrodynamic and ecosystem part. The main goal of this work was to create a three-dimensional, biological model embedded in the hydrodynamical model for simulation of the annual phytoplankton biomass in the Baltic Sea.

2. The CEMBSv1 model

The CEMBSv1 model was embedded in the existing 3D hydrodynamic model of the Baltic Sea. Described in project ECOOP IP WP 10 sea – ice model (POPCICE) has been used to implement biological equations for plankton system. Some basic information about the model: POPCICE – coupled sea-ice model. The model consists of Parallel Ocean Program (POP) and Community Ice Code. Both are from Los Alamos National Laboratory (LANL). POPCICE was forced using European Centre for Medium-Range Weather Forecasts (ECMWF) data. It is forced by the following atmospheric fields: 2 meters temperature and dew point, long and short waves radiation (downward), 10 meters wind speed and air-ocean wind stress. Ocean model time step is 480 s and ice model time step is 1440 s. Horizontal resolution for ice and ocean model: ~9 km (1/12 degree). Vertical resolution (ocean model): 21 levels (for the Baltic sea ~18 levels). Both models work on the same grid, so there are no problems with exchanging fluxes between the models. In this paper, we are focused only on the biological part of the model.

Conceptual basis

The ecosystem model is based on 1D biological model of Dzierzbicka-Glowacka [2, 3]. In 3D model, phytoplankton is represented by state variable and the model formulations are based on a simple total inorganic nitrogen ($\text{NO}_3 + \text{NO}_2 + \text{NH}_4$) cycle (Figure 1). Nutrient serves initially as a means to trigger the bloom of phytoplankton and later to limit the phytoplankton production.

The model is conceptualized for the shallow sea, typical with the replenishment of the mixed layer with nutrients from the bottom. The water column dynamics are implemented in a three-dimensional frame, where phytoplankton and nutrient (nitrogen) are transported by advection and diffusion. The physical frame, including all necessary forcing is presented at Figure 2.

The biological model incorporates formulations for the primary production mechanism and remineralization mechanisms within the mixed layer, in the lower layer and at the bottom. Primary producers are transported, die and are utilized by zooplankton (mesozooplankton). The grazed phytoplankton is divided into three parts: the first one contributes to zooplankton growth, the second is deposited as fecal pellets, and the last one is excreted by zooplankton as dissolved metabolites; thus, it replenishes the nutrient pool.

A proportion of the material contributing to growing is assumed to be lost immediately, representing dying zooplankton. Proportions of both the fecal and the excreted material are immediately regenerated (see [2]). Mortality of phytoplankton is modeled in two ways: the grazing by mesozooplankton, which form the bulk of grazers in the Baltic Sea and here it is prescribed by mesozooplankton biomass; all other kinds of mortality, like cell lyses and

grazing by zooplankton other than mesozooplankton, are assumed to be proportional to phytoplankton standing stock, with a constant mortality rate, and therefore dynamically coupled to phytoplankton dynamics. The effect of the microbial food web (see [1]) is parameterized by converting this portion of detrital material immediately into regenerated nutrients within the water column. The major portion sediments onto the bottom where it is re-worked by benthic communities.

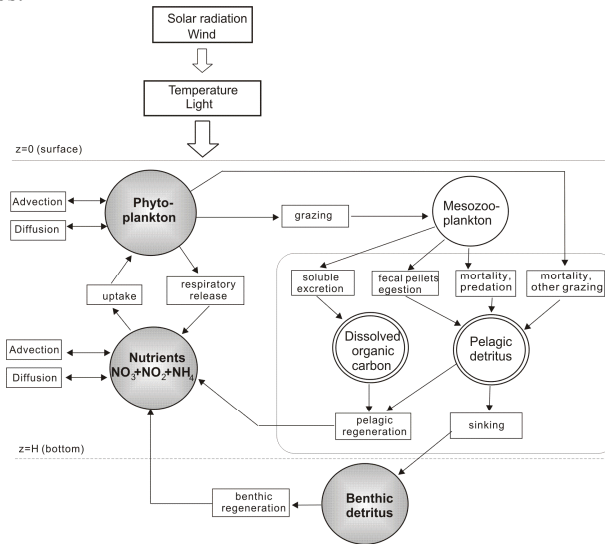


Fig. 1. Schematic diagram of the CEMBSv1 processes

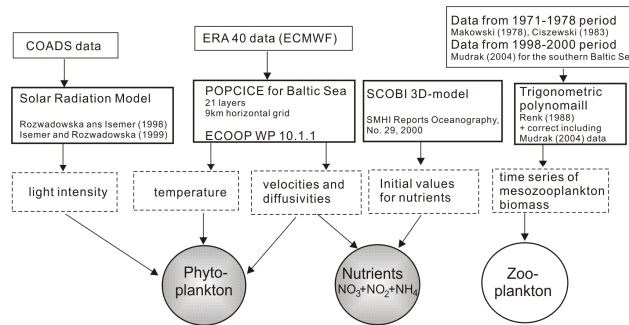


Fig. 2. Schematic diagram of the forcing data and related state variables

Equations

Two partial differential equations describe the spatial and temporal evolution in the total inorganic nitrogen $Nutr(x,y,z,t)$ (mmol N m^{-3}) and phytoplankton $Phyt(x,y,z,t)$ (mg C m^{-3}) pools, and an ordinary differential equation describes



the benthic detritus $Detr(x,y,t)$ (mg C m⁻²) pool. The set of equations with model parameters is below presented.

$$\begin{aligned} \frac{\partial Phyt}{\partial t} = & - \left(u \frac{\partial Phyt}{\partial x} + v \frac{\partial Phyt}{\partial y} \right) + \frac{\partial}{\partial x} \left(K_x \frac{\partial Phyt}{\partial x} \right) + \frac{\partial}{\partial y} \left(K_y \frac{\partial Phyt}{\partial y} \right) - (w + w_z) \frac{\partial Phyt}{\partial z} + \frac{\partial}{\partial z} \left(K_z \frac{\partial Phyt}{\partial z} \right) \\ & + PRP - RESP - MORP - GRZ \\ \frac{\partial Nutr}{\partial t} = & - \left(u \frac{\partial Nutr}{\partial x} + v \frac{\partial Nutr}{\partial y} \right) - w \frac{\partial Nutr}{\partial z} + \frac{\partial}{\partial x} \left(K_x \frac{\partial Nutr}{\partial x} \right) + \frac{\partial}{\partial y} \left(K_y \frac{\partial Nutr}{\partial y} \right) + \frac{\partial}{\partial z} \left(K_z \frac{\partial Nutr}{\partial z} \right) + \\ & + g_N \left[- (PRP - RESP_{light}) + RESP_{dark} + p_M MORP + p_F FEC + p_Z (MORZ + PRED) + EXCZ \right] \\ \frac{\partial Detr}{\partial t} = & D - REMD \end{aligned}$$

$$D = \int_0^H \left[(1 - p_M) MORP + (1 - p_F) FEC + (1 - p_Z) (MORZ + PRED) \right] dz$$

where: u, v, w – the time-dependent velocities obtained from the POPCICE, and w_z – sinking velocity of phytoplankton, K_x, K_y, K_z – horizontal and vertical diffusion coefficient (see ECOOP WP 10.1.1).

The first four terms on the right-hand side of the phytoplankton equation describe the horizontal and vertical advection and diffusion of phytoplankton, where u, v and w are the time-dependent velocities obtained from our model for the Baltic Sea (POPCICE, see ECOOP WP 10.1.1), K_x, K_y, K_z are the horizontal and vertical diffusion coefficients, and the following terms describe gross production (PRP), respiration ($RESP$), mortality ($MORP$) and grazing (GRZ). Gross primary production (PRP) is calculated from the nutrient and light limitation functions - f_N and f_I . Steele's function, (Steele, 1962) where optimal light intensity I_{opt} , is used as a light limitation function which includes photoinhibition. For nutrient limitation the Michaelis-Menten formula is applied with a constant K_N as the half-saturation constant. Respiration ($RESP$) consists of basal maintenance and photorespiration, each being proportional to phytoplankton biomass, where the basic dark respiration proportion is r_{BR} as a proportionality factor to the maximum photosynthetic rate, and the photorespiration proportion r_{PR} is proportional to gross primary production. The temperature dependence f_T is modeled according to $f_T = \exp(0.0769(T-10))$ with the constant 0.0769 expressing the respiration change f_T with temperature, yielding a doubling by an increase of 10°C in temperature and $f_T(T_o) = 1$ at $T_o = 10^\circ\text{C}$. Mortality of phytoplankton ($MORP$) is assumed to be proportional to the phytoplankton standing stock, with mortality rate mp . Copepod grazing (GRZ) is assumed to be proportional to copepod biomass $Zoop$ with rate g_{max} , but this rate is modified by a Michaelis-Menten function of phytoplankton biomass with the half-saturation constant k_{Phyt} subject to a threshold $Phyt_o$, below which grazing ceases.

The state equation for nutrient includes the first four terms on the right-hand side expressing the horizontal and vertical advection and diffusion of nutrient, where the same velocities and diffusion coefficients are used as for phytoplankton, and the four processes nutrient uptake (UPT), dark respiratory



release (*RELE*), remineralization in the water column (*REM*) and zooplankton excretion (*EXCZ*). Nutrient uptake (*UPT*) appears in the nitrogen equation for positive net production in the euphotic zone only. The constant g_N is the N:C ratio according to the Redfield ratio. Respiration in the dark consumes particulate organic matter. To conserve matter, the respiration term in the equation for phytoplankton carbon must be balanced by a nutrient release term (*RELE*) in the equation for nitrogen. This term parameterizes the contribution of respiration to the nutrient pool at the given fixed ratio g_N . For light intensities below the compensation intensity, the respiratory release is regenerated immediately into nitrogen. Fractions of dead phyto- and zooplankton and of fecal pellets that are instantaneously remineralized within the water column by the microbial food web (*REM*) are given by proportionality factors p_M for phytoplankton, p_Z for zooplankton and p_F for fecal pellets. Excretion of dissolved (*EXCZ*) and particulate material is parameterized as fixed proportions of zooplankton grazing (ez), fecal pellet production (f) and zooplankton mortality (mz), with the condition $ez + f + mz = 1$.

The benthic detritus equation consists of two terms, sedimentation out of the water column to the bottom (indicated by the integration from the surface to the bottom H , simultaneously from all depths) and regeneration at the bottom. Effect of sedimentation of detrital material out of the water column consists of contributions by dead phytoplankton, fecal pellets and dead zooplankton, which are not remineralized in the water column by the microbial food web. Remineralization at the bottom is assumed to be proportional to the amount of available benthic detritus, with a constant rate r_D .

3. Results of the simulations

For a large areas, the biogeochemical processes strongly depend on hydrodynamics of the sea. On figures (3-5) monthly model output for the surface layer is shown for the different model variables (temperature, phytoplankton and nutrient). Figure 4 presents the onset of the spring bloom of phytoplankton calculated by the model. It shows that the simulated spring bloom begins in the Skagerrak-Kattegat area earlier than in the Baltic Proper. When the spring bloom starts in the Baltic Proper it firstly develops in the coastal zone and southern part and then it is spread northwards. In late spring/early summer the spring bloom starts in the Gulf of Finland and Bothnian Sea and finally it reaches the Bothnian Bay. In the second part of year, in September and October, blooms of smaller intensity appears throughout the Baltic, but in the northern regions and coastal zone of the sea they are higher than in the southern Baltic Sea.

Following the annual nutrient dynamics (Figure 5), the season begins with high total inorganic nitrogen concentrations in the whole column water. As the spring starts the nutrient is consumed. The phytoplankton prefers ammonia to nitrate, so as long as ammonia is available, ammonia is consumed.

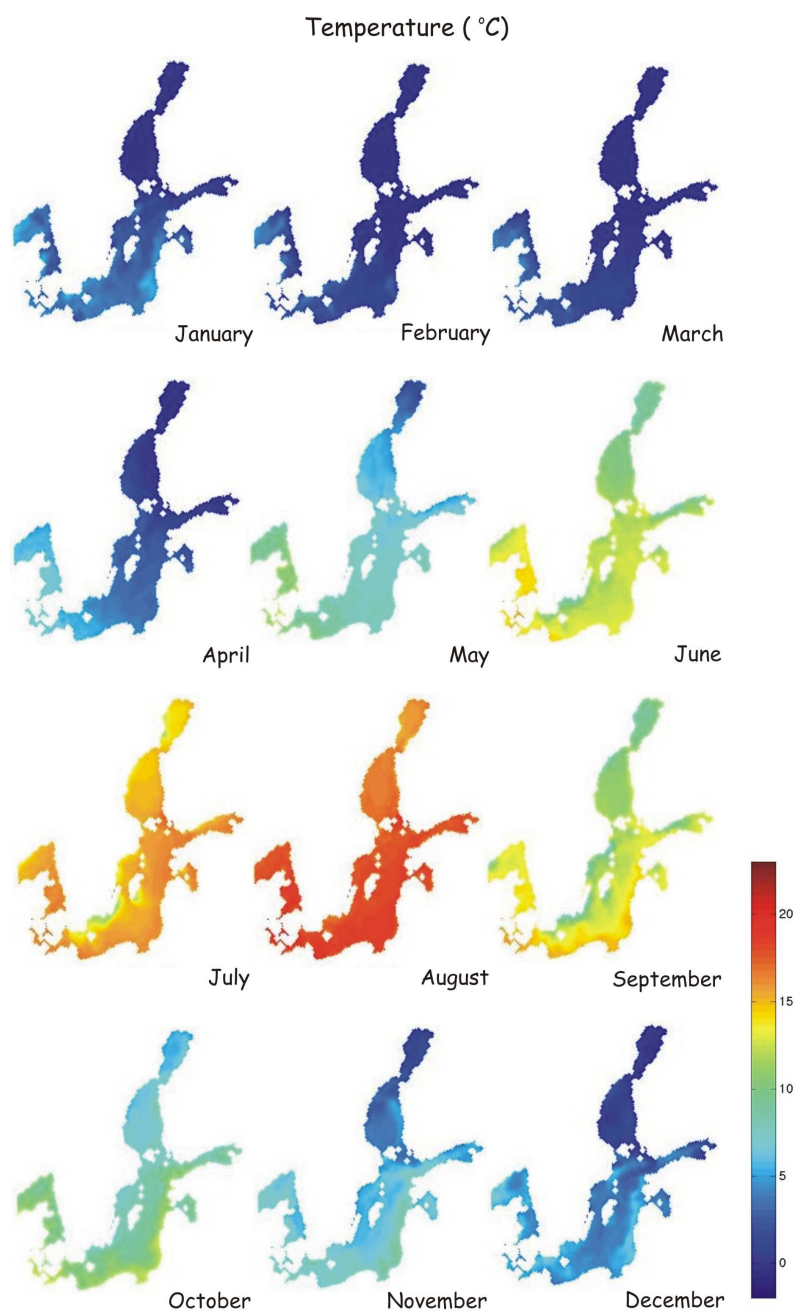


Fig. 3. Monthly averaged temperature (°C) for the surface layer during January – December 2004

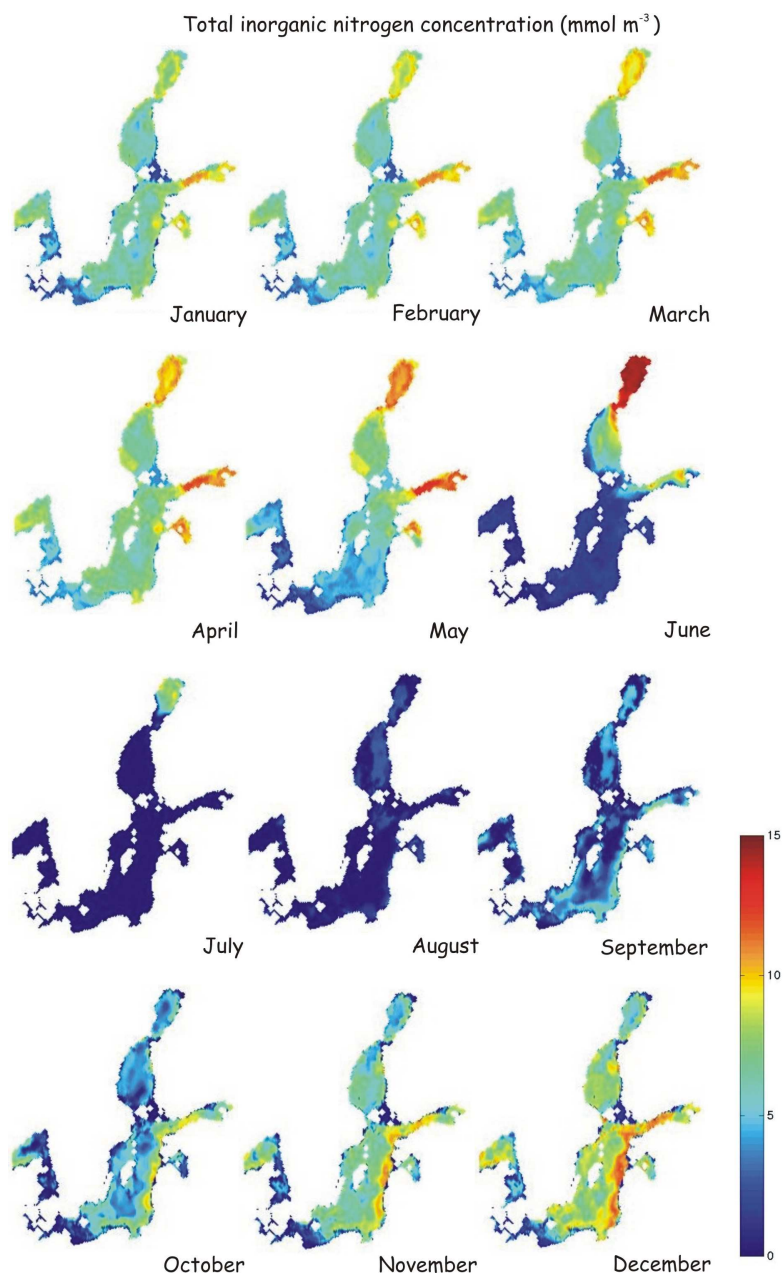


Fig. 4. Monthly averaged total inorganic nitrogen concentration (mmol m^{-3}) for the surface layer during January – December 2004

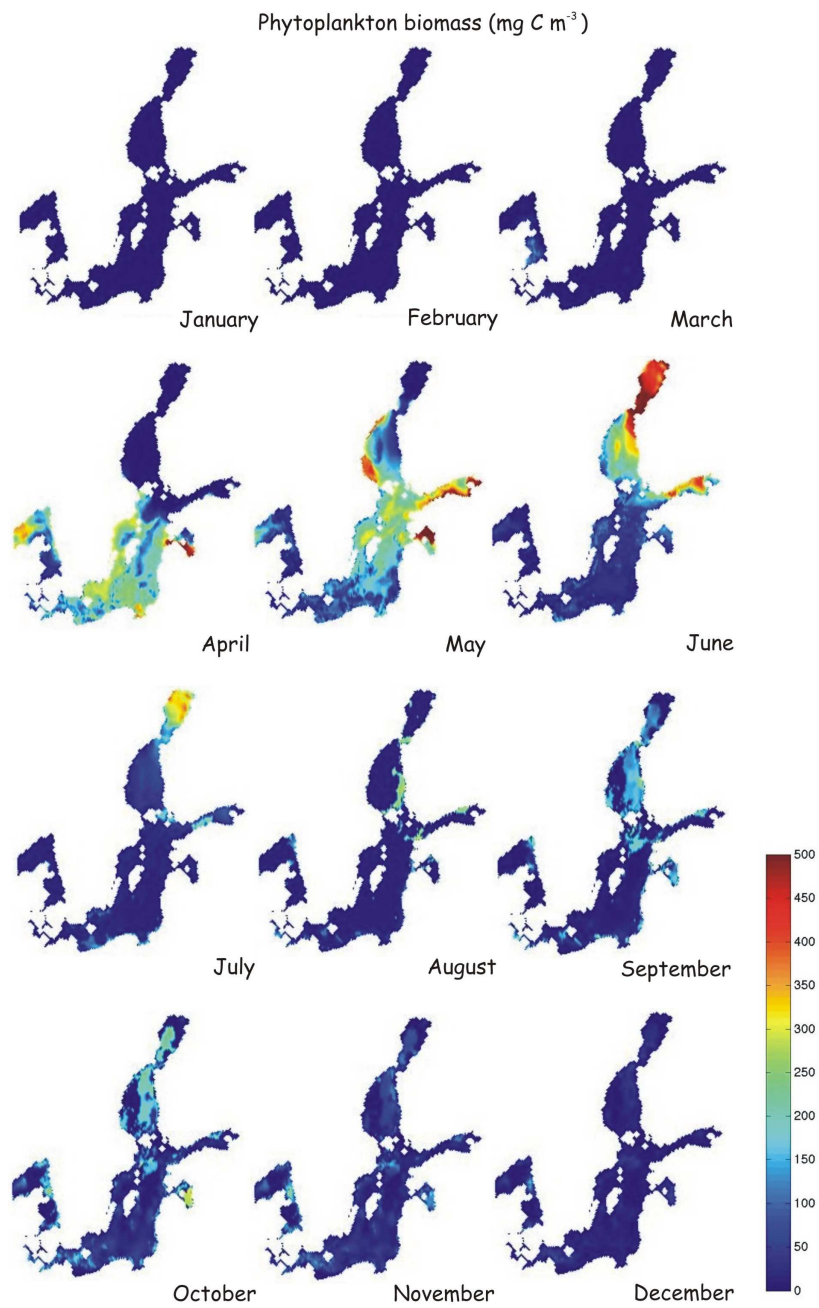


Fig. 5. Monthly averaged phytoplankton biomass (mgC m^{-3}) for the surface layer during January – December 2004



As soon as the ammonia pool in the surface layer is emptied, the phytoplankton turns towards the nitrate for assimilation. It is also noticeable that the one spring bloom has started, and the total inorganic nitrogen concentrations turn low, the bloom is maintained by the external supply of inorganic nitrogen. At the end of June, when the system is depleted of nitrate, the nitrogen fixation starts and phosphorus pool is regained, it is not included in this model. However, winds are strong enough in September to replenish the full water column with abundant nutrients. In the autumn, there is a slightly rise in the phytoplankton biomass. It is caused by the increase in nutrient concentrations resulting from the deeper mixing of the water. However, the growing season is ended in December, when the phytoplankton biomass dropped to the January-February level.

4. Conclusions

As a rule, mathematically simulated data are only an approximation of environmental processes. However, a properly validated model provides substantial knowledge as regards the spatial and temporal resolutions of processes, which is very difficult to obtain from in situ measurements.

The results indicate that the 3D CEMBSv1 model could be a useful tool for investigating the annual phytoplankton biomass and predicting its changes. Some of the discrepancies observed (see ECOOP WP 10.1.3 Project) could be the result of the dynamism of ecosystem changes.

The 3D CEMBSv1 model is an open model which enables the study of (1) annual, seasonal, monthly and daily variability of marine plankton in the southern Baltic sea, (2) the impact of various climatic conditions over several years, and (3) the influence of different hydrophysical and biological process on the vertical distributions of characteristics as a function of time. The 3D model presented in this paper may have a practical use in forecasting ecological changes in the Baltic (see [4], ECOOP WP 10.1.3 Project).

References

1. F. Azam, T. Fenchel, J. Field, J. S. Gray, L. A. Meyer-Reil, and F. Thingstad. The Ecological Role of Water-Column Microbes in the Sea *Mar Ecol Prog Ser* 10:257–263, 1983.
2. L. Dzierzbicka-Głowacka. Modelling the seasonal dynamics of marine plankton in southern Baltic Sea. Part 1. A Coupled Ecosystem Model. *Oceanologia* 47:591–619, 2005.
3. L. Dzierzbicka-Głowacka. Modelling the seasonal dynamics of marine plankton in southern Baltic Sea. Part 2. Numerical simulations. *Oceanologia* 48:41–71, 2006.
4. L. Dzierzbicka-Głowacka, J. Jakacki, M. Janecki and A. Nowicki. Long-term variations of the distribution of phytoplankton biomass in the Baltic Sea simulated by a three-dimensional model. *Oceanologia* 53, (in press) 2011.
5. HELCOM. Development of tools for assessment of eutrophication in the Baltic Sea. Baltic Sea Environmental Proceedings, no. 104, pp. 64, 2006 <http://www.helcom.fi/stc/files/Publications/Proceedings/bsep104.pdf>





A New Solution for Optimal Control a Non-Linear Model by Transformation to Measure Space *

Sara Ebrahimi, Hamid Reza Sahebi

Department of Mathematics, Islamic Azad University, Branch Ashtian, Ashtian, Iran

E-mail: ebrahimi@mail.aiau.ac.ir

Abstract: In the recent decade, a considerable number of optimal control problems have been solved successfully based on the properties of the measures. Even the method, has many useful benefits, in general, it is not able to determine the optimal trajectory and control at the same time; moreover, it rarely uses the advantages of the classical solutions of the involved systems. In this article, we are going to use of measure theory for solving bone marrow cancer. Model adapted from a paper by K.R.Fister and J.C.Panetta [9].

Keywords: Non-Linear Model, Bone marrow cancer model, optimal control, Radon measure, cell-cycle-specific, dynamic System.

1. Introduction

According to an idea of L. C. Young, by transferring the problem in to a theoretical measure optimization, in 1986 Rubio introduced a powerful method for solving optimal control problems ([12]). The important properties of the method (globality, automatic existence theorem a linear treatment even for extremely nonlinear problems,...) caused it to be applied for the wide variety of problems. Even the method has been used frequency for solving several kinds of problems, like [5], [6], [7], [8] and [10], but at least two important points were not considered in applying the method yet. Generally the method can not be able to produce the acceptable optimal trajectory and control directly at the same time; and moreover, the classical format of the system solution, usually is not taken into account. Therefore, there is no any possibility to use this important fact and their related literatures in the analysis of the system not prescribed, although the various table text styles are provided. The formatter will need to create these components, incorporating the applicable criteria that follow.

chemotherapy drugs are a common type of drug used in treating cancer. The main action of these drugs works against cells in a specific phase of the cell cycle. That is, all cells go through a well-studied cycle of growth which includes a resting phase, a DNA replication phase, and a cell division (mitosis) phase. These types of drugs do not affect cells in the resting state. Hence, cells in the quiescent state are thought of as kinetically resistant to these drugs. Agur [1],

* Paper included in *Chaotic Systems: Theory and Applications*, C.H. Skiadas and I. Dimotikalis, Eds, World Scientific, pp 302—308, 2010.



Agur, Arnon, and Schechter [2] use both age-structured and probabilistic models with an “on-off” type drug function (the drug is either active or inactive) to describe the effects of cell-cycle-specific drugs on the bone marrow. Swan [15] provides a good review of the role of optimal control in non-cell-cycle-specific cancer chemotherapy. Another work by Swierniak, Polanski, and Kimmel [16] uses optimal control theory on a cell-cycle-specific chemotherapeutic model. They investigate a variety of ways to model the cell-cycle by various groupings of the cell-cycle phases. In each case, they attempt to minimize the total cancer mass at the end of some specified time interval using the least amount of drug possible.

2. The nonlinear model of bon marrow cancer

There is a control model study the effects of chemotherapy as a immune system infected with bone marrow cancer, see for example Panetta [10]. We basically used the model and notation introduced in [10]. We assume that the control model of bone marrow cancer is an follows:

$$\frac{dP}{dt} = (\gamma - \delta - \alpha - su(t))P(t) + \beta Q(t) \quad (1)$$

$$\frac{dQ}{dt} = \alpha P(t) - (\lambda + \beta)Q(t) \quad (2)$$

The function $u(t)$ is the control describing the effects of the chemotherapeutic treatment only on the proliferating cells. There are measurable functions defined on $J=[0,T]$, which bounded and assume . In the medical model (1), parameters and constrains, defined as follows:

$P(t)$ =The proliferating cell mass in the bone marrow

$Q(t)$ =The quiescent cell mass in the bone marrow

γ =Cycling cells growth rate

δ =Natural cell death

β =Transion rate from resting to proliferating

λ =Cell differentiation

s =The strength or effectiveness of the ~treatment

All the units for the parameters are We would like to give as much drug as possible while not excessively destroying the bone marrow. The objective function that to be maximized is defined as:

$$J(P, Q, u) = \int_0^T [aP(t) + Q(t) - \frac{b}{2}(1-u(t))^2] dt \quad (3)$$

The parameters a and b are weights describing the importance of each term in the objective functional. The objective function is contained the total amount of one arrow and the amount of drug give. Model adapted from a paper by K.Renee Fister and J.Carl Panetta [9].

3. Transformation nonlinear model

We define the function $f_0 : J \times P \times Q \times U \rightarrow R$ as following where P, Q and U are compact subsets of R



$$f_0(t, p(t), q(t), u(t)) = a(p(t) + q(t)) - \frac{b}{2}(1 - u(t))^2$$

then we write the problem (2) in the following form:

$$\begin{aligned} \text{Min} \quad & \Xi[p(\cdot), q(\cdot), u(\cdot)] = \int_0^T f_0(t, p(t), q(t), u(t)) dt \\ \text{S.to:} \quad & \dot{p}(t) = f_1(t, p(t), q(t), u(t)), \\ & \dot{q}(t) = f_2(t, p(t), q(t), u(t)), \quad (4) \\ & p(0) = p_0, \quad q(0) = q_0, \\ & p(T) = p_T, \quad q(T) = q_T \end{aligned}$$

Now, Let $\Omega = J \times P \times Q \times U$ and f_1, f_2 are continuous functions, where the trajectory functions $p(t)$ and $q(t)$ is absolutely continuous and the control function $u(t)$ is Lebesgue-measurable. We assume that the set of all admissible pairs is nonempty and denote it by Γ . Let $\omega = [X(\cdot), u(\cdot)]$ be an admissible pair, and B an open ball in R^3 containing $J \times A$, and $C'(B)$ be the space of all real-valued continuously differentiable functions on B such that the first derivation is also bounded.

Let $\phi \in C'(B)$, and define function $\phi_{f_1}, \phi_{f_2}, \psi_1, \psi_2$ as follows:

$$\begin{aligned} \phi_{f_i}(t, X(t), u(t)) &= \phi_X(t, X(t)) \cdot f_i(t, X(t), u(t)) + \phi_t(t, X(t)) \\ \psi_i(t, X(t), u(t)) &= p(t) \psi'_i(t) + f_i(t, X(t), u(t)) \psi_i(t) \quad (5) \end{aligned}$$

Also by choosing a variable t , we have

$$\int_0^T g(t, X(t), u(t)) dt = a_g, \quad g \in C_1(\Omega) \quad (6)$$

By using [11] and Radon measure μ , we have:

$$\mu(\phi_{f_i}) = \Delta \phi_i, \quad i = 1, 2 \quad \phi \in C'(B) \quad (7)$$

$$\mu(\psi_i) = 0, \quad i = 1, 2 \quad \psi \in (0, T) \quad (8)$$

$$\mu(g) = a_g, \quad g \in C_1(\Omega) \quad (9)$$

Define Ω the set of all positive Radon measures on satisfying (7), (8) and (9) as Σ . Also we assume $M^+(\Omega)$ be the set of all positive Radon measures on Ω . Now if we topologize the space $M^+(\Omega)$ by the weak*-topology, it can be shown that Σ is compact ([12]).

4. Metamorphosis

We now estimate the optimal control by a nearly-optimal piecewise constant control. The problem (7), (8) and (9) is an infinite dimensional linear



programming problem, because all the functionals in (7),(8) and (9) are linear in the variable μ , and furthermore μ is required to be positive.

Now, we construct a piecewise constant control function corresponding to the finite-dimensional problem. Therefore in the infinite-dimensional linear programming problem (7)-(9) with restriction defined by [9], we shall consider how

one can choose total functions in the constraints (7)-(9). Consider first ϕ_i in $C'(B)$ as the following form:

$$\begin{aligned}\phi_1 &= p, & \phi_2 &= q \\ \phi_3 &= p^2, & \phi_4 &= q^2 \\ & \dots & & \dots\end{aligned}$$

Trivially the linear combinations of these functions are uniformly dense in the space $C_1(\Omega)$ ([14]), we choose only M_1 number of them. Also, we choose

M_2 functions with compact support in the following form:

$$\psi_r(t) = \begin{cases} \sin[2\pi r \left(\frac{t-0}{T}\right)] & r = 1, 2, \dots, M_{21} \\ 1 - \cos[2\pi r \left(\frac{t-0}{T}\right)] & r = M_{21} + 1, \dots, 2M_{21} \end{cases}$$

Finally, it is necessary to choose L number of functions of time only, as follows:

$$g_s(t) = \begin{cases} 1 & t \in J_s \\ 0 & \text{otherwise} \end{cases}$$

Where $J_s = \left(\frac{0 + (s-1)T}{L}, \frac{0 + sT}{L}\right)$

The set $\Omega = J \times A \times U$ will be covered with a grid, where the grid will be defined by taking all points in Ω as $z_j = (t_j, p_j, q_j, u_j)$

the points in the grid will be numbered sequentially from 1 to N , which can be estimated numerically. Instead of the infinite-dimensional linear programming problem, we consider the following finite dimensional linear programming problem, where $z_j \in \omega$



$$\text{Minimize} \quad \sum_{j=1}^N \alpha_j f_0(z_j)$$

Subject to :

$$\left\{ \begin{array}{ll} \sum_{j=1}^N \alpha_j \phi_{f_i} = \Delta \phi_i, & i = 1, 2, \dots, M_1 \\ \sum_{j=1}^N \alpha_j \psi_r(z_j) = 0, & j = 1, 2, \dots, M_{21} \\ \sum_{j=1}^N \alpha_j g_s(z_j) = a_g, & s = 1, 2, \dots, L \end{array} \right.$$

5. Numerical Example

In section we obtain the approximation solution of the bone marrow cancer problem by measure theory technique . Numerical information for parameters is as in [9] and can be found in the following.

$$\begin{aligned} \gamma &= 1.47 & \delta &= 0 \\ \alpha &= 5.643 & \beta &= 0.48 \\ \lambda &= 0.164 & a &= b1 \end{aligned}$$

let the set $t \in J = [0, 2]$ divided into 10 subinterval, the sets P, Q and U are divided respectively into 10 subintervals, so that Ω is divided into 10,000 equal subsets.

We assume

$$Z_m = (t_m, p_m, q_m, u_m), \quad m = 1, 2, \dots, 10,000$$

$$m = i + 10(j - 1) + 100(k - 1) + 1000(l - 1),$$

$$1 \leq i \leq 10, \quad 1 \leq j \leq 10,$$

$$1 \leq k \leq 10, \quad 1 \leq l \leq 10,$$

Then our linear programming problem form



$$\text{Minimize } \sum_{m=1}^{10,000} \alpha_m \left\{ a(p_m + q_m) - \frac{b}{2}(1 - u_m)^2 \right\}$$

Subject to :

$$\left\{ \begin{array}{l} \sum_{m=1}^{10,000} \alpha_m \{A_m\} = -0.8 \\ \sum_{m=1}^{10,000} \alpha_m \{B_m\} = 0.69 \\ \sum_{m=1}^{10,000} \alpha_m \{2 p_m A_m\} = -0.96 \\ \sum_{m=1}^{10,000} \alpha_m \{2 q_m B_m\} = 1.8561 \\ \\ \sum_{m=1}^{10,000} \alpha_m \{ \pi h p_m \cos \pi h t_m + A_m \sin \pi h t_m \} = 0 \\ \\ \sum_{m=1}^{10,000} \alpha_m \{ \pi h q_m \cos \pi h t_m + B_m \sin \pi h t_m \} = 0 \\ \\ \sum_{m=1}^{10,000} \alpha_m \{ \pi h p_m \sin \pi h t_m + A_m (1 - \cos \pi h t_m) \} = 0 \\ \\ \sum_{m=1}^{10,000} \alpha_m \{ \pi h q_m \sin \pi h t_m + B_m (1 - \cos \pi h t_m) \} = 0 \\ \\ \alpha_1 + \alpha_2 + \dots + \alpha_{1000} = 0.2 \\ \alpha_{1001} + \alpha_{1002} + \dots + \alpha_{2000} = 0.2 \\ \dots \\ \dots \\ \alpha_{9001} + \alpha_{9002} + \dots + \alpha_{10000} = 0.2 \end{array} \right.$$

The graph of the control and trajectory are shown in Figs.1-2, respectively .

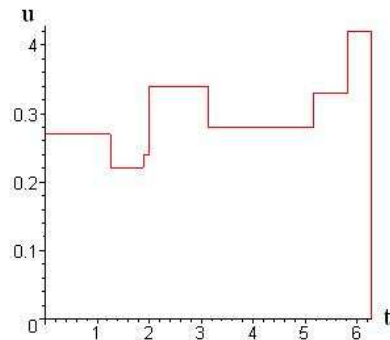


Figure1: The Optimal Control $u(t)$

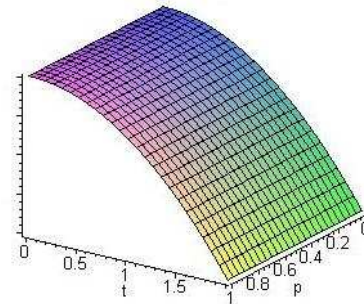


Fig 3

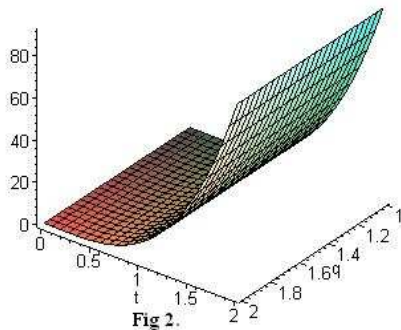


Fig 2.

References

1. Z. Agur, "The effect of drug schedule on responsiveness to chemotherapy," Ann. New York Acad. Sci., 504,1986, pp. 274-277
2. Z. Agur, R. Arnon, and B. Schechter, , "eduction of cytotoxicity to normal tissues by new regimens of cell-cycle phase-specific drugs" Math. Biosci., 92,1988 , pp. 1-15.
3. G. Chqquet, "Lectures on Analysis," Benjamin, New York (1969).
4. R.E. Edwards, "unctional Analysis Theory and Application," Holt, Rinehart and Winston, New York 1965.
5. J., A. Fakharzadeh and J. E., Rubio,"Global Solution of Optimal Shape Designe Problems," ZAA Journal for Analysis and its Applications. Vol.16,No.1, 1999, pp.143-155.
6. J., A .Fakharzadeh., "Determining the Best Domain for a Non-linear Wave System," JAMC J. of Applied Mathematics and Computing, Vol.13,No.1-2, , 2003, pp.183-194.
7. M. H., Farahi, " The Boundary Control of the Wave Equation," PhD thesis, Dept. of Applied Mathematical Studies, Leeds University, April 1996.
8. M. H. Farahi, H. H,Mehneh., and A. H.,Borzabadi, "Wing Drag Minimization by Using Measure Theory," J. Optimization Methoda and Software, 2005, pp.1-9.
9. K.R.Fister, and J.C.Panetta, "Optimal Control applied to cell-cycle-specific cancer chemotherapy," SIAM.J.Math, Vol 60,No 3, 2000, pp.1059-1072.



10. A. V. Kamyad, J. E. Rubio, and D. A. Wilson, "The Optimal Control of Multidimensional Diffusion Equation," *JOTA*, 1(70), 1991, pp.191-209.
11. J. E. Rubio, "Control and Optimization: the Linear Treatment of Non-linear Problems," Manchester University Press, Manchester, 1986.
12. J. E. Rubio, "The Global Control of Non-linear Elliptic Equation," *Journal of Franklin Institute*, 330(1), 1993, pp.29-35.
13. W. Rudin, "Real and Complex Analysis," McGraw-Hill(3Ed), 1987.
14. P. C. Rosenbloom, "Quelques Classes de Problèmes Extremaux," *Bulletin de Societe Mathematique de France*, 80, 1952, pp.183-216.
15. G. W. Swan, "Role of optimal control theory in cancer chemotherapy," *Math. Biosci.*, 101, 1990, pp. 237-284.
16. A. Swierniak, A. Polanski, and M. Kimmel, "Optimal control problems arising in cell-cycle specific cancer chemotherapy," *Cell Prolif.*, 29, 1996, pp. 117-139.
17. F. Trèves, "Topological vector spaces, Distributions and Kernels," Academic Press, New York and London 1967



Nonlinear programming methods for solving problems: a recent bibliographic review

Nicolas Fernando Gavlak¹, André Augusto Gavlak²

¹ Paulista University - UNIP, Bauru, Brazil

² Brazilian National Institute for Space Research – INPE, São José dos Campos, Brazil

E-mail: nicolasgavlak@gmail.com

Abstract: A great number of mathematical-programming applications are cast naturally as linear programs. Linear programming assumptions or approximations may also lead to appropriate problem representations over the diversity of decision variables being measured. At other times, however, nonlinearities in the form of either nonlinear objective functions or nonlinear constraints are critical for representing an application properly as a mathematical program. In mathematics, nonlinear programming (NLP) is the process of solving a system of equalities and inequalities, collectively termed constraints, over a set of unknown real variables, along with an objective function to be maximized or minimized, where some of the constraints or the objective function are nonlinear. This paper aims to list several nonlinear programming methods for solving problems that have been published at last 10 years.

Keywords: nonlinear programming, methods, bibliographic review

1. Introduction

The models produced by linear programming are, as its name implies, linear (both the objective function, and restrictions). This fact is, without doubt, "most of the restrictions" imposed on a model of programming. In most applications, linear models reflect only approximations of real models. Physical or economic phenomena are usually better represented by nonlinear models.

Most nonlinearities encapsulated in a programming model is within two main categories:

- 1) Relations empirically observed, such as changes in non-proportional costs, results and process quality characteristics.
- 2) Structurally derived relations, which include physical phenomena inferred mathematically and administrative rules.

In general, the models employed in Nonlinear Programming are like:

$$\text{Max (or Min) } f(x)$$

$$\begin{cases} g_i(x) \leq b_i \\ x \geq 0 \end{cases} \quad \text{for } i=1, 2, \dots, m$$

With:

$$X = (x_1, x_2, \dots, x_n)$$

$f(\cdot)$ and $g_i(\cdot)$ are nonlinear functions



The methods for solving problems of Nonlinear Programming can be divided into two groups: 1) Models without restrictions and 2) Models with restrictions. The main concept involved in Nonlinear Programming is the rate of change. The major problem that hinders the achievement of the optimal solution of the problems Nonlinear Programming is the minimum and maximum (extreme) local of the objective function.

According to [1], the practical problems of optimization often involve nonlinear behavior, which must be taken into consideration. Sometimes it is possible to reformulate these nonlinearities to fit a linear programming format. However, the best approach often is to use a nonlinear programming formulation. In most models is that real problems do not have some degree of linearity.

When studying computer science, or science in general is essential to seek to understand what the state of the art research theme. For this, the literature review becomes essential because through it we know what is being produced in the academic environment and, therefore, brings ideas and explanations for the researcher.

Thus, this paper attempts to show some work on nonlinear programming produced recently, with the objective of join, organize and present a systematic manner such publications.

2. Bibliographic Review

The propose of [2] was a new approach to solving nonlinear optimization problems with discrete variables using continuation methods. His focus was on pure integer nonlinear optimization problems with linear equality constraints (ILENP) but he showed how the technique can be extended to more general classes of problems such as those involving linear inequality and mixed integer constraints.

He showed the effectiveness of the approach by applying it to a number of real problems and also test problems taken from the literature. These include the binary unconstrained quadratic problem, the frequency assignment problem and the quadratic assignment problem. The results were compared to those from alternative methods, indicating that the new approach was able to produce good-quality solutions for diverse classes of nonlinear discrete optimization problems.

[3] presented a nonlinear model predictive control (NMPC) for multiple autonomous helicopters in a complex environment. The NMPC provides a framework to solve optimal discrete control problems for a nonlinear system under state constraints and input saturation. Their approach combines stabilization of vehicle dynamics and decentralized trajectory generation, by



including a potential function that reflects the state information of possibly moving obstacles or other vehicles to the cost function.

Various realistic scenarios were presented by [3] which show that the integrated approach outperforms a hierarchical structure composed of a separate controller and a path planner based on the potential function method. The proposed approach is combined with an efficient numerical algorithm, which enables the real-time nonlinear model predictive control of multiple autonomous helicopters.

[4] studied an integrated overview and derivation of mixed-integer nonlinear programming (MINLP) techniques, Branch and Bound, Outer-Approximation, Generalized Benders and Extended Cutting Plane methods, as applied to nonlinear discrete optimization problems that are expressed in algebraic form. Numerical comparisons were presented on a small process network problem to provide some insights to confirm the theoretical properties of these methods.

The objective of the work of [5] was to develop non-linear programming models for land grading to be applied in irregular shaped areas and that minimize soil movement. The GAMS (General Algebraic Modeling System) software was used for calculations and the models were compared with the Method of Generalized Minimum Squares developed by [6], using as evaluation parameter the volume of moved soil. It was concluded that the non-linear programming models developed in this study were shown suitable for application to irregular shaped areas and provided smaller values of soil movement when compared with the method of minimum squares.

3. Conclusions

A bibliographical review on nonlinear programming is extremely important when performing research in this area. Thus, this work has brought a brief presentation on some works that use this form of programming to solve the most diverse problems.

References

1. F. S. Hillier, G. J. Lieberman. *Introdução à pesquisa operacional*. 3th Ed. Rio de Janeiro, 1988.
2. Kien-Ming Ng. A continuation approach for solving nonlinear optimization problems with discrete variables, *Doctoral Thesis*, Stanford University, 2002.
3. D.H. Shim, H. Jin Kim, S. Sastry. Decentralized Nonlinear Model Predictive Control of Multiple Flying Robots: Autonomously Controlled Advanced Platforms, *Proceedings of the 42nd IEEE Conference on Decision and Control*, Maui, Hawaii, USA, 2003.
4. I.E. Grossmann, Z. Kravanja, Mixed-Integer Nonlinear Programming Techniques for Process Systems Engineering, *Computers and Chemical Engineering*, 19, 1995.



5. G. A. Biscaro, J. C. C. Saad. Sistematização de terras para irrigação em áreas irregulares utilizando modelos de programação não-linear. *Revista Ceres*, 54, 315, pp. 441-446, 2007.
6. E. J. Scaloppi, L. S. Willardson. Practical land grading based upon least squares. *Journal of Irrigation and Drainage Engineering*. 112, pp. 98-109, 1986.



Erratic behavior of an overdamped oscillator subject to two periodic fields

M. Gitterman

Department of Physics, Bar-Ilan University, Ramat-Gan 52900, Israel

Abstract. A harmonic oscillator subject to two periodic fields with two incommensurate frequencies is characterized by a broadband spectrum of the correlation function, which is typical for deterministic chaos. This "erratic" behaviour, like deterministic chaos, shows the close connection between determinism and chaos.

Keywords: .

The oscillator is the well-known toy model which is commonly used to describe many phenomena in Nature. In addition to the deterministic model, extensive use has been made of the stochastic oscillator which is described by the deterministic equation supplemented by a random force which has chaotic solutions. One of the great achievements of twentieth-century physics was the prediction of deterministic chaos which appears without any random force in the equations [1]. Deterministic chaos means an exponential increase in time of the solutions for even the smallest change in the initial conditions. Therefore, to obtain a "deterministic" solution, one has to specify the initial conditions to an infinite number of digits. Otherwise, the solutions of deterministic equations show chaotic behavior. To exhibit deterministic chaos, the differential equations have to be nonlinear and contain at least three variables. This points to the important difference between underdamped and overdamped equations of motion of an oscillator, since deterministic chaos may occur only in the underdamped oscillator.

Here, we consider an overdamped oscillator subject to two periodic fields,

$$\frac{dx}{dt} + \omega^2 x = C_1 \cos(\omega_1 t) + C_2 \cos(\omega_2 t), \quad (1)$$

and show that the solutions of this equation are "erratic", being intermediate between deterministic and chaotic solutions.

The stationary solutions of Eq. (1) have the following form

$$x(t) = \frac{C_1}{\omega_1} \sin(\omega_1 t) + \frac{C_2}{\omega_2} \sin(\omega_2 t) \quad (2)$$

Replace the continuous time in Eq. (1) by the discrete times $2\pi n/\omega_2$ [2]. The solution of this equation then becomes

$$x\left(n\frac{2\pi}{\omega_2}\right) = x(0) + \frac{C_1}{\omega_1} \sin\left(2\pi n\frac{\omega_1}{\omega_2}\right) \quad (3)$$



If ω_1/ω_2 is an irrational number, the sin factor in (3) will never vanish and the motion will become "erratic". The properties of "erratic" motion can be understood from analysis of the correlation function associated with the n -th and $(n + m)$ -th points,

$$C(2\pi m\omega_1/\omega_2) = \lim_{N \rightarrow \infty} \frac{1}{N} \sum_{n=0}^{N-1} x(2\pi n\omega_1/\omega_2) x[2\pi(n+m)\omega_1/\omega_2] = x^2(0) + x(0) \left(\frac{C_1}{\omega_1}\right) \lim_{N \rightarrow \infty} \frac{1}{N} \sum_{n=0}^{N-1} \{\sin(2\pi n\omega_1/\omega_2) + \sin[2\pi(n+m)\omega_1/\omega_2]\} + \left(\frac{C_1}{\omega_1}\right)^2 \lim_{N \rightarrow \infty} \frac{1}{N} \sum_{n=0}^{N-1} \sin(2\pi n\omega_1/\omega_2) \sin[2\pi(n+m)\omega_1/\omega_2] \quad (4)$$

Using the well-known relations between the trigonometric functions, one obtains from (4)

$$C\left(m \frac{2\pi\omega_1}{\omega_2}\right) = x^2(0) + \frac{1}{2} \left(\frac{C_1}{\omega_1}\right)^2 \cos\left(m \frac{2\pi\omega_1}{\omega_2}\right) \quad (5)$$

The Fourier spectrum of the correlation function (5) depends on the ratio ω_1/ω_2 . If this ratio is a rational number, this spectrum will contain a finite number of peaks. However, for irrational ω_1/ω_2 , the spectrum becomes broadband, what is typical of deterministic chaos. However, this "erratic" behavior arises from a simple "integrable" equation (1), which distinguishes it from deterministic chaos.

In conclusion, we found that in addition to deterministic chaos, which forms a bridge between deterministic and chaotic phenomena, another possibility exists for the "erratic" behavior induced by two periodic forces with incommensurate frequencies.

References

- 1.H. G. Schuster and W. Just, *Deterministic Chaos: An Introduction* [Wiley, 2005].
- 2.E. Ott, *Chaos in Dynamical Systems* [Cambridge University Press, 2002].



Modeling and Simulation of a Reactive Packed Distillation Column Using Delayed Neural Networks

Abdulwahab GIWA¹ and Süleyman KARACAN¹

¹Ankara University, Tandoğan, Ankara, Turkey

E-mail: agiwa@eng.ankara.edu.tr

Abstract: The complex nature of the reactive packed distillation column owing to the occurrence of both reactions and separations in a single unit brought up the need for the search for a very robust tool of representing the process. In view of this, delayed neural networks are considered as tools that can handle this problem effectively. As such, in this work, Nonlinear AutoRegressive, Nonlinear AutoRegressive with eXogenous inputs and Nonlinear Input-Output models are developed and simulated with the aid of MATLAB R2010b to predict the top and bottom sections temperatures. The predicted results obtained from the Input-Output models were not satisfactory. However, observing the good agreements from the plots as well as the correlation coefficients and the mean squared errors between the predicted results of the NAR and NARX models and the experimental ones showed that these two models can be used to represent the reactive packed distillation column.

Keywords: Reactive packed distillation column, Delayed Neural Network (DNN), Nonlinear AutoRegressive (NAR), Nonlinear AutoRegressive with eXogenous inputs (NARX), Nonlinear Input-Output (IO), MATLAB, Correlation coefficient (R), Mean squared error (MSE).

1. Introduction

In recent years, integrated reactive separation processes have attracted considerable attention in both academic research and industrial applications, Völker et al., 2007 [1]. One of these processes which is known as reactive distillation is potentially attractive whenever conversion is limited by reaction equilibrium, Balasubramhanya and Doyle III, 2000 [2]. Reactive distillation combines the benefits of equilibrium reaction with the traditional unit operation (distillation) to achieve a substantial progress in not only promoting the reaction conversion through constant recycling of reactants and removal of products but also reducing the capital and operating costs. In addition, reactive distillation has the capability of avoiding azeotropes. However, the design of reactive distillation processes, especially when a packed column is involved, is still a challenge because of the difficulties involved in obtaining process models capable of reliably describing the several complexes (such as the exhibition of multiple steady states) and interrelated phenomena including simultaneous reactions and separations in the column. The complicated behavior of the process made the search for a very robust and powerful tool of modeling and simulating the dynamics of the reactive distillation very challenging. Among the



strategies proposed for handling this kind of a task are the neural networks because they can be trained to handle complex functions, Beale et al., 2010 [3]. Neural Networks (NN) modeling can be viewed as a nonlinear empirical model that are especially useful in representing input–output data, in making predictions in time, and in classifying data, Himmelblau, 2000 [4]. NN can be highly nonlinear, can learn easily, require little or no a priori knowledge of the structure, are fault-tolerant and can handle complex problems that cannot be satisfactorily handled by the traditional methods, MacMurray and D. M. Himmelblau, 2000 [5].

In this paper, a reactive packed distillation column is modeled and simulated using three different kinds of delayed neural network models and the production of ethyl acetate from the reaction between acetic acid and ethanol was used as a case study.

2. The Model and Simulations

2.1 Data acquisition

The data used for the neural network modeling were acquired by carrying out experiments in a pilot scale packed reactive distillation column shown in Figure 1 which has, excluding the condenser and the reboiler, a height and a diameter of 1.5 and 0.05 m respectively. The main column was divided into three parts of 0.5 m each. The upper, middle and lower sections were the rectification, reaction and stripping sections respectively. The rectification and stripping sections were packed with rasching rings while the reaction section was filled with Amberlyst 15 catalyst. The column was fed with acetic acid at the top (between the rectification section and the reaction section) whereas ethanol was fed at the bottom (between the reaction section and stripping section) with the aid of peristaltic pumps which were operated with the aid of a computer program (MATLAB/Simulink). The top, reaction, stripping and bottom sections temperatures were measured and recorded on-line and in real-time using thermocouples linked to the computer also via MATLAB/Simulink. The reaction taking place in the column is given as:





Fig.1. Reactive packed distillation pilot plant

Two different experiments were carried out using a reboiler duty of 560 W and applying a step input to the recycle ratio from total reflux to 5 and acetic acid to ethanol feed ratio from 0 to 1.25 to generate two sets of data. One set was used for training and validating the model while the other was used to test the developed model.

2.2 Model development

The sets of data obtained from the experiments were treated by converting them to time sequence ones which were represented by a cell array because the delayed neural network model to be developed required that the data have to be sequential. The parameters used for the formulation of the model are as shown in Table 1 below:

Table 1. Neural network model formulation parameters

S/N	Parameter	Value/Description
1.	No. of inputs	2
	No. of outputs	2
2.	No. of layers	2
3.	No. of neurons	10
4.	No. of delays	5
5.	Training algorithm	Levenberg-Marquardt

Three kinds of delayed neural networks (Nonlinear Autoregressive, Nonlinear Autoregressive with Exogenous Inputs and Nonlinear Input-Output) models



were developed for the reactive packed distillation column using the parameters tabulated above.

The mathematical structures of the models are thus;

$$\text{NARX: } y(t) = f(u(t-1), u(t-2), \dots, u(t-d), y(t-1), y(t-2), \dots, y(t-d)) \quad (2)$$

$$\text{NAR: } y(t) = f(y(t-1), y(t-2), \dots, y(t-d)) \quad (3)$$

$$\text{Input-Output: } y(t) = f(u(t-1), u(t-2), \dots, u(t-d)) \quad (4)$$

2.2 Results and discussions

Applying a step change to the inputs (recycle ratio and feed ratio) of the model, the generated outputs from the experiments described in Section 2.1 are as shown in Figure 2 below.

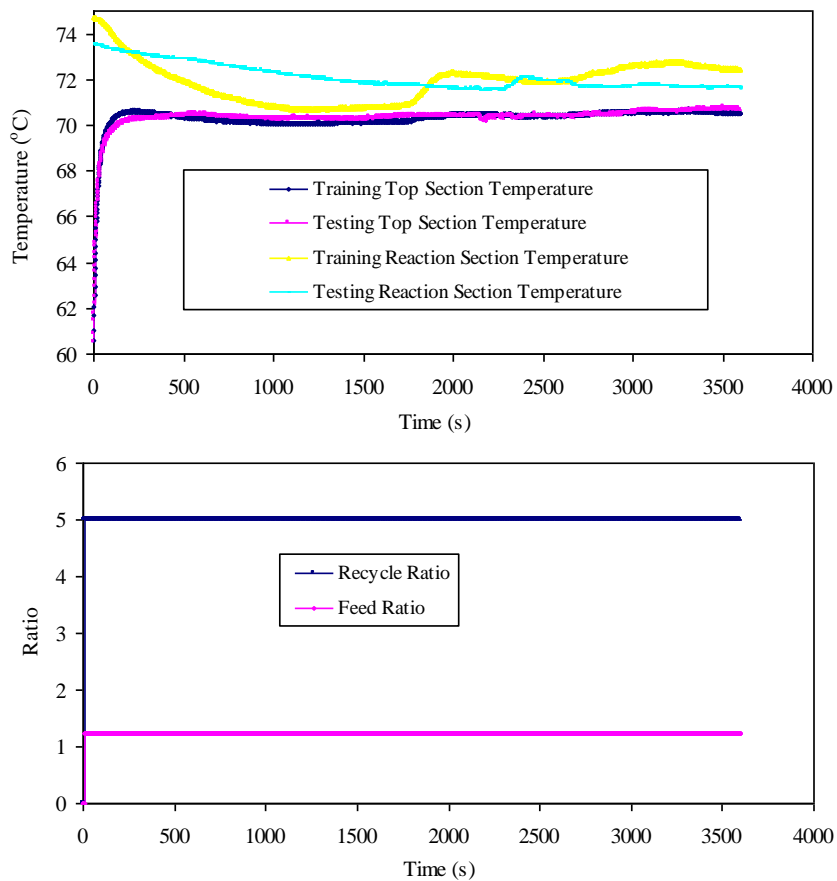


Fig 2. Input-output sampled data



After developing the neural network models, each of them was tested using the separate testing data collected in order to predict the top section and reaction section temperatures. Figure 3 and Figure 4 show the results of temperature predictions for the top and reaction sections respectively.

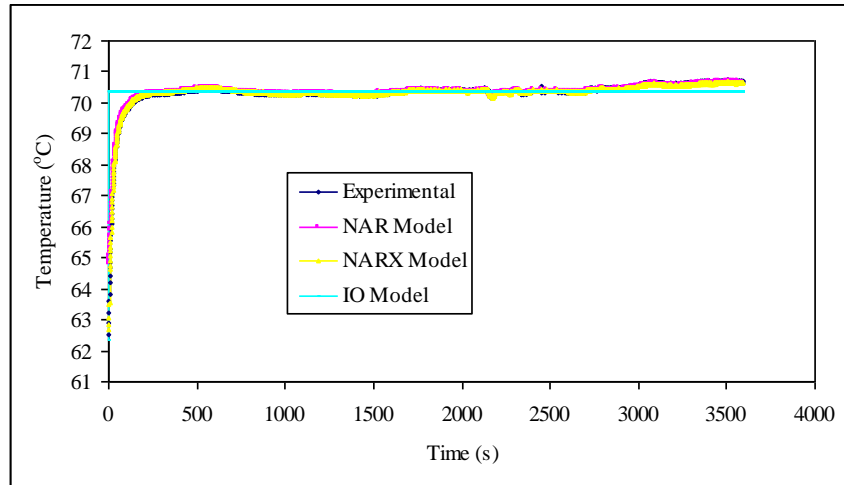


Fig. 3. Temperature prediction for the top section

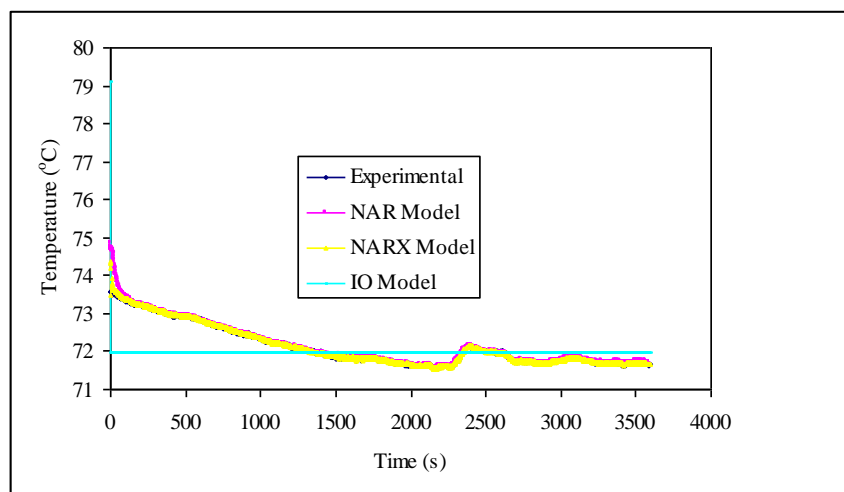


Fig. 4. Temperature prediction for the reaction section

From the results shown in Figure 3 and Figure 4, it was observed that there were good correlations between the experimental and predicted results for the NARX



and NAR models and the relationships can also be supported by observing the performance values of the networks shown in Table 2 below.

Table 2. Delayed neural network model performance values

Model Type	Top section temperature		Reaction section temperature	
	MSE	R	MSE	R
NAR	0.0063	0.9927	0.0120	0.9852
NARX	0.0023	0.9952	0.0011	0.9984
IO	0.2270	0.2642	0.3195	0.0454

From the table, it was observed that the correlation coefficients were 0.9927 and 0.9852 respectively for top section and reaction section temperatures predictions using NAR model while those of the NARX model were 0.9952 and 0.9984 respectively. The good results given by these models can be attributed to the presence of feedback in the model structures.

However, in the case of the Nonlinear Input-Output model, the situation was different because, as can be seen from the graphs, the curves produced were not in close relationships with those of the experimental data. The unsatisfactory performance of this model can also be seen from Table 2. For instance, the correlation coefficients obtained when this model was used to predict the top and reaction sections temperatures were 0.2642 and 0.0454 respectively. These values are very low for any good model. The discrepancies observed between the predicted results of this model and the experimental data can be said to be as a results of the fact that the Nonlinear IO model structure does not incorporate the past values of the target variables.

3. Conclusions

Three kinds of delayed neural networks models were developed and simulated. The good closeness of predicted results to the experimental ones for both the NARX and NAR models revealed that both of them could be used to represent the dynamics of the reactive packed distillation column.

Acknowledgements

One of the authors, Abdulwahab GIWA, wishes to acknowledge the support received from The Scientific and Technological Research Council of Turkey for his PhD Programme. In addition, this research was supported by Ankara University Scientific Research Projects.

References

1. M. Völker, C. Sonntag and S. Engell. Control of Integrated Processes: A Case Study on Reactive Distillation in a Medium-Scale Pilot Plant. *Control Engineering Practice* 15:863–881, 2007.



2. M. H. Beale, M. T. Hagan and H. B. Demuth. *Neural Network Toolbox 7*. The MathWorks Inc., Apple Hill Drive, Natick MA, 2010.
3. L. S. Balasubramhanya and F. J. Doyle III. Nonlinear Model-Based Control of a Batch Reactive Distillation Column. *Journal of Process Control* 10:209-218, 2000.
4. D. M. Himmelblau. Applications of Artificial Neural Networks in Chemical Engineering. *Korean Journal of Chemical Engineering* vol. 17, no. 4, 373–392, 2000.
5. J. C. MacMurray and D. M. Himmelblau. Modeling and Control of a Packed Distillation Column Using Artificial Neural Networks. *Computers and Chemical Engineering* vol. 19, no. 10, 1077–1088, 1995.





Sir Pinski Rides Again

Maria Ivette Gomes,¹ Dinis Pestana² and Pedro Pestana³

¹ Universidade de Lisboa and CEAUL, Lisboa, Portugal

(E-mail: ivette.gomes@fc.ul.pt)

² Universidade de Lisboa and CEAUL, Lisboa, Portugal

(E-mail: dinis.pestana@fc.ul.pt)

³ Universidade Lusfada and CEAUL, Lisboa; Universidade Católica and CITAR, Porto, Portugal (E-mail: pedro.duarte.pestana@gmail.com)

Abstract. The iterative procedure of removing “almost everything” from a triangle ultimately leading to the Sierpinski’s gasket \mathcal{S} is well-known. But what is in fact left when almost everything has been taken out? Using the Sir Pinski’s game described by Schroeder [4], we identify two dual sets of invariant points in this exquisite game, and from these we identify points left over in Sierpinski gasket. Our discussion also shows that the chaos game does not generate the Sierpinski gasket. It generates an approximation or, at most, a subset of \mathcal{S} .

Keywords: Sierpinski gasket, Sierpinski points, fractals, Sir Pinski game, chaos game, self-similarity, periodicity.

1 Introduction

Let \mathcal{T} be a triangle. A player chooses a point P_0 inside the triangle. Sir Pinski game consists of iteratively jumping to the points $\{P_1, P_2, \dots\}$, where P_{k+1} doubles the distance of P_k to its nearest vertex. The player looses at step n if $P_0, P_1, P_2, \dots, P_{n-1} \in \mathcal{T}$ and $P_n \notin \mathcal{T}$.

Let \mathcal{M}_1 denote the “middle triangle” whose vertices are the middle points of the \mathcal{T} sides. It is obvious that \mathcal{M}_1 is the set of loosing points at step 1. Similarly, the union \mathcal{M}_2 of the three middle triangles of $\mathcal{T} - \mathcal{M}_1$ is the set of loosing points at step 2, the union \mathcal{M}_3 of the 3^2 middle triangles of $(\mathcal{T} - \mathcal{M}_1) - \mathcal{M}_2 = \mathcal{T} - (\mathcal{M}_1 \cup \mathcal{M}_2)$ is the set of loosing points at step 3, and so on. Loosing points are illustrated in Figure 1, that also clarifies the connection of loosing points at step n with middle triangles removed at step n in the classical iterative construction of the Sierpinski gasket.

Schroeder [4] characterizes Sierpinski’s gasket as the set of winning points $\mathcal{S} = \mathcal{T} - \bigcup_{k=1}^{\infty} \mathcal{M}_k$ of Sir Pinski game.

In fact, from Banach’s contractive mapping fixed point theorem it follows that the Sierpinski gasket $\mathcal{S} = \mathcal{T} - \bigcup_{k=1}^{\infty} \mathcal{M}_k = \bigcup_{i=1}^3 \psi_i(\mathcal{S})$, where $\psi_i(\cdot)$ is the dilation of ratio $1/2$ around the vertex v_i of \mathcal{T} . In other words, \mathcal{S} is the unique non-empty fixed point of the corresponding Hutchinson operator [2] ψ , where $\psi(\mathcal{A}) = \psi_1(\mathcal{A}) \cup \psi_2(\mathcal{A}) \cup \psi_3(\mathcal{A})$, i.e. $\psi(\mathcal{A}) = \mathcal{A}$ if and only if $\mathcal{A} = \mathcal{S}$.

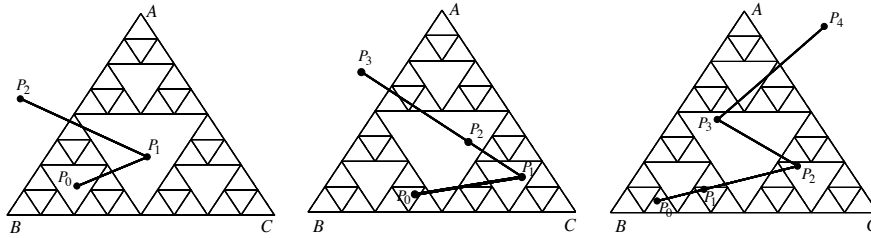


Fig. 1. Loosing points at steps 2 (*left*), 3 (*center*) and 4 (*right*).

Hence the Sierpinski points $s \in \mathcal{S}$ can be characterized as the set of points $s \in \mathcal{T}$ such that $(s + v_i)/2 \in \mathcal{S}$, $i = 1, 2, 3$. So, starting from whatever point $P \in \mathcal{T}$, iteratively jumping for a point halving the distance to v_i creates an infinite sequence of points in a straight line that ultimately converges to v_i . Observe however that

- if $P \in \mathcal{S}$, all the iterates are Sierpinski points; but, on the other hand,
- if $P \notin \mathcal{S}$, none of the iterates is a Sierpinski point.

In fact, the halving contractions ψ_i generate points that are nearer and nearer to Sierpinski points, but as the Sir Pinski game clearly shows their inverse doubling ultimately leaves \mathcal{T} unless the starting point is itself a Sierpinski point.

Iteratively halving (or, alternatively, doubling) the distance to a fixed vertex v_i creates an infinite sequence of colinear points. Hence we need some rule to use in turn, either deterministically or randomly, the different vertices in order to approximate the Sierpinski gasket \mathcal{S} . Sir Pinski game uses the rule: take the nearest vertex to the starting point/iterate, and double the distance. A “dual” rule is: use the farthest vertex from the starting point/iterate, and halve the distance (randomly choose one of the vertices when there is a tie) — this rule has the advantage of always changing the vertex to use in sequential steps of the algorithm.

Barnsley [1] devised a *chaos game*, using randomness to generate the three sets $\psi_i(\mathcal{T})$: pick a starting point P_0 , and generate iterates $\{P_1, P_2, \dots\}$, such that P_k is the midpoint of the segment whose endpoints are P_{k-1} and one of the vertices v_i of \mathcal{T} , randomly chosen using the discrete uniform law $X = \begin{Bmatrix} v_1 & v_2 & v_3 \\ 1/3 & 1/3 & 1/3 \end{Bmatrix}$. This chaos game is generally presented as a device to generate the Sierpinski gasket \mathcal{S} , but in view of the above observations it produces in general an approximation of the Sierpinski gasket, since in general $P_0 \notin \mathcal{S}$. Observe also that even starting from a Sierpinski point, what we obtain is a subset of the Sierpinski gasket — for example, the choice of the top vertex of the equilateral triangle used in [3], page 306, will generate as iterates only vertex points of the triangles left out when middle triangles are removed, in the classical deterministic iterative construction of \mathcal{S} . This issue will be discussed later in further detail.

2 The points of the Sierpinski gasket

As seen in the introduction, the points $s \in \mathcal{S}$ are easily described using the concept of self-similarity and its far-reaching consequences.

Using translation and rotation, if needed, we assume that the vertices of \mathcal{T} are $v_L = (0, 0)$, $v_R = (a, 0)$, $a > 0$, and $v_T = (c, d)$, $d > 0$.

If \mathcal{T} is the triangle with vertices $v_L = (0, 0)$, $v_R = (1, 0)$, and $v_T = (0, 1)$, in dyadic notation its Sierpinski points are $s = (x, 1 - x)$, i.e. if the abscissa is $x = 0.\nu_1\nu_2\nu_3\dots$, the k -th digit of the ordinate is $1 - \nu_k$ — for instance, $s = (0.11001011101\dots, 0.00110100010\dots)$, cf. Peitgen *et al.* [3], p. 173.

Let \mathcal{T} be the equilateral triangle with unit height, vertices $v_L = (0, 0)$, $v_R = (2\sqrt{3}/3, 0)$, and $v_T = (\sqrt{3}/3, 1)$. Schroeder [4], pp. 22–24, used a sophisticated redundant three-coordinates points affixation to show that the Sierpinski points are those with coordinates (in dyadic expansion) $x = 0.a_1a_2a_3\dots$, $y = 0.b_1b_2b_3\dots$, $z = 0.c_1c_2c_3\dots$, such that $(a_k, b_k, c_k) \in \{(1, 0, 0), (0, 1, 0), (0, 0, 1)\}$, $k = 1, 2, \dots$

Let us now consider that \mathcal{T} is the equilateral triangle with unit sides, with top vertex $A = (1/2, \sqrt{3}/2)$, left vertex $B = (0, 0)$, and right vertex $C = (1, 0)$. Project A in the point $A' = (1/3, 0)$, B in $B' = (5/6, \sqrt{3}/6)$, and C in $C' = (1/3, \sqrt{3}/3)$.

We claim that the points

- $V_1 = (3/7, 2\sqrt{3}/7)$, intersection of $\overline{AA'}$ with $\overline{CC'}$,
- $V_2 = (5/14, \sqrt{3}/14)$, intersection of $\overline{AA'}$ with $\overline{BB'}$, and
- $V_3 = (5/7, \sqrt{3}/7)$, intersection of $\overline{BB'}$ with $\overline{CC'}$,

are Sierpinski points, cf. Figure 2.

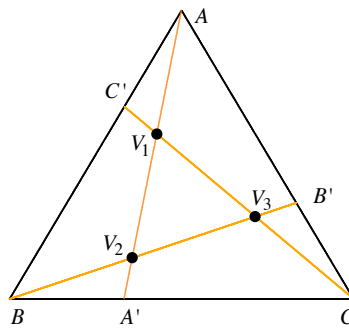


Fig. 2. Period-3 invariant Sir Pinski $\{V_1, V_2, V_3\}$ attractor.

In fact, V_1 is the midpoint of $\overline{AV_2}$, V_2 is the midpoint of $\overline{BV_3}$, V_3 is the midpoint of $\overline{CV_1}$, and therefore those points are winning points in the Sir Pinski game, i.e. $\{V_1, V_2, V_3\}$ is an invariant cycle-3 attractor of Sierpinski points.



Project A in the point $A'' = (2/3, 0)$, B in $B'' = (2/3, \sqrt{3}/3)$, and C in $C'' = (1/6, \sqrt{3}/6)$. Obviously, intersecting $\overline{AA''}$ with $\overline{BB''}$ we obtain $W_1 = (4/7, 2\sqrt{3}/7)$, intersecting $\overline{AA''}$ with $\overline{CC''}$ we obtain $W_2 = (9/14, \sqrt{3}/14)$, and intersecting $\overline{BB''}$ with $\overline{CC''}$ we obtain $W_3 = (2/7, \sqrt{3}/7)$. For similar reasons, $\{W_1, W_2, W_3\}$ is an invariant cycle-3 attractor of Sierpinski points, cf. Figure 3.

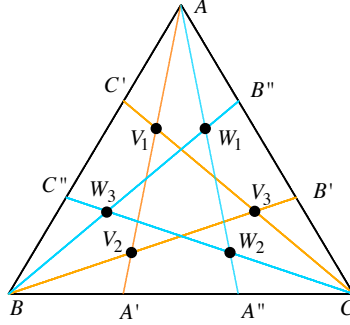


Fig. 3. Period-3 $\{V_1, V_2, V_3\}$ and $\{W_1, W_2, W_3\}$ invariant Sir Pinski points attractors. $\{A\}$, $\{B\}$ and $\{C\}$ are invariant in Sir Pinski game; $\{A', A''\}$, $\{B', B''\}$ and $\{C', C''\}$ are period-2 invariant sets in Sir Pinski game.

Remark 1. If we re-scale multiplying by $2/\sqrt{3}$ in order to have unit heights (i.e., each vertex is at distance 1 from the opposite side), the ordinates of the transformed V_1^* and W_1^* become $4/7$, the ordinates of the transformed V_2^* and W_2^* become $1/7$, and the ordinates of the transformed V_3^* and W_3^* become $2/7$.

Hence, if we adhere to Schroeder [4] three-coordinates system (x, y, z) , where x is the distance from the bottom side, y the distance from the left side, and z the distance from the right side, we see that the period-3 invariant points must have x -coordinate $4/7, 1/7$ or $2/7$.

From the $(2\pi/3)$ -rotational symmetry of \mathcal{T} , it follows that in Schroeder's three coordinates system $V_1^* = (4/7, 1/7, 2/7)$, $V_2^* = (1/7, 2/7, 4/7)$, $V_3^* = (2/7, 4/7, 1/7)$, $W_1^* = (4/7, 2/7, 1/7)$, $W_2^* = (1/7, 4/7, 2/7)$, and $W_3^* = (2/7, 1/7, 4/7)$. \square

Remark 2. The points $V_1, V_2, V_3, W_1, W_2, W_3$ lie on a circumference of radius $\sqrt{21}/21$ centered at the barycenter $(1/2, \sqrt{3}/6)$ of \mathcal{T} . \square

Remark 3. Each vertex of \mathcal{T} is invariant in Sir Pinski game. Hence $A, B, C \in \mathcal{S}$. On the other hand, in Sir Pinski game, the image of A' is A'' and vice-versa, i.e. $\{A', A''\}$ is a period-2 invariant set, and the same holds for $\{B', B''\}$



and $\{C', C''\}$. $\mathcal{V} = \{V_1, V_2, V_3\}$ and $\mathcal{W} = \{W_1, W_2, W_3\}$ are period-3 invariant sets (attractors) in Sir Pinski game.

Higher order periodic invariant sets do exist. For instance, using conditions $(a - 1/2)^2 + (b - \sqrt{3}/2)^2 = 4[(2a - 1/2)^2 + (2b - \sqrt{3}/2)^2]$ and $(2b - \sqrt{3}/2)/(2a - 1/2) = (\sqrt{3}/2 - b)/(a - 1/2)$ on the set of points $\{(a, b), (2a, 2b), (1 - a, b), (1 - 2a, 2b)\}$, so that $(a, b) = (0.3, 0.288675)$, we obtain the period-4 invariant set $\{(0.3, 0.288675), (0.6, 0.636194), (0.7, 0.288675), (0.4, 0.636194)\}$, cf. Figure 4.

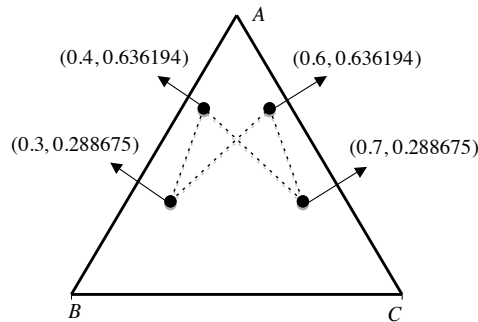


Fig. 4. A period-4 invariant Sir Pinski set.

Using the $(2\pi/3)$ -rotational symmetry of \mathcal{T} , two other period-4 invariant sets are readily obtained. \square

Now we perform the same construction in the T_1 (Top), L_1 (Left) and R_1 (Right) triangles remaining once the middle triangle of \mathcal{T} is removed in step 1 of the classical construction of the Sierpinski gasket, obtaining 2×3^2 points — 3^2 V s and 3^2 W s —, as shown in Figure 5. With the

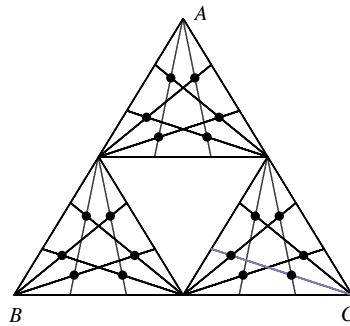


Fig. 5. More Sierpinski points, in T_1 , in L_1 and in R_1 .

self-explaining addressing and notations V_{i,L_1}, W_{i,L_1} , $i = 1, 2, 3$, it is obvious



that $V_{i,L_1} = \frac{1}{2} V_i$ and $W_{i,L_1} = \frac{1}{2} W_i$ — for instance, $V_{2,L_1} = (5/28, \sqrt{3}/28)$, $V_{1,L_1} = (4/14, 2\sqrt{3}/14)$.

Analogously, the corresponding points in the Right triangle R_1 are $V_{i,R_1} = (1/2, 0) + 1/2 V_i$ and $W_{i,R_1} = (1/2, 0) + 1/2 W_i$, and the corresponding points in the Top triangle T_1 are $V_{i,T_1} = (1/4, \sqrt{3}/4) + 1/2 V_i$ and $W_{i,T_1} = (1/4, \sqrt{3}/4) + 1/2 W_i$. For instance, $V_{1,T_1} = (13/28, 11\sqrt{3}/28)$.

The 3^2 V points in this second stage of the construction are, following the above algorithm, $(3/14, \sqrt{3}/7)$, $(5/7, \sqrt{3}/7)$, $(13/28, 11\sqrt{3}/28)$, $(5/28, \sqrt{3}/28)$, $(19/28, \sqrt{3}/28)$, $(3/7, 2\sqrt{3}/7)$, $(5/14, \sqrt{3}/14)$, $(6/7, \sqrt{3}/14)$, $(1/28, 9\sqrt{3}/28)$ — exactly the 9 points we obtain when we compute the middle point of the segments joining each of the $(3/7, 2\sqrt{3}/7)$, $(5/14, \sqrt{3}/14)$, $(5/7, \sqrt{3}/7)$ V points from stage one of the construction with each of the three vertices of \mathcal{T} . Similar results hold in what concerns W points.

Continuing the procedure, in step 3 of the iterative construction of Sierpinski's gasket we obtain 2×3^3 points as shown in Fig. 6. (We have included some extra segments connecting points to make clear that in Sierpinski game whatever the initial V point [respectively, W point], in a few steps we shall land in the attractor $\mathcal{V} = \{V_1, V_2, V_3\}$ [respectively, in $\mathcal{W} = \{W_1, W_2, W_3\}$].)

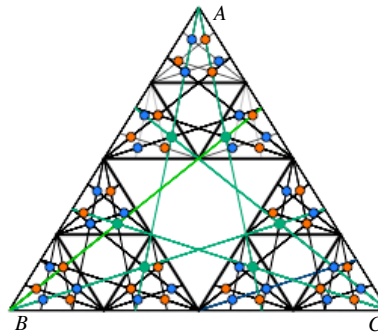


Fig. 6. More Sierpinski points, in T_1 , in L_1 and in R_1 .

Once again the coordinates of any V or W point are easy to compute. For instance $W_{1,L_1T_2} = (1/8, \sqrt{3}/8) + (1/2)^2 \times (4/7, 2\sqrt{3}/7) = (9/56, 11\sqrt{3}/56)$, since the left vertex of the triangle whose address is L_1T_2 is $(1/8, \sqrt{3}/8)$.

Using the same line of reasoning, the $V_{i,R_1T_2R_3}$ points of $R_1T_2R_3$ will have coordinates $(3/4, \sqrt{3}/8) + (1/2)^3 V_i$, the $W_{i,R_1L_2T_3T_4}$ points of $R_1L_2T_3T_4$ will have coordinates $(13/16, (13/16)(\sqrt{3}/2)) + (1/2)^4 W_i$. More generally,

- in step n , the coordinates of the original V s and W s are scaled by a factor $(1/2)^n$;
- the address determines the left vertex of the triangle: a L_k does not affect neither the abscissa nor the ordinate, a R_k shifts the left corner $(1/2)^k$



and does not affect the ordinate, and a T_k adds $(1/4)^k$ to the abscissa and $(1/2)^k \sqrt{3}/2$ to the ordinate.

For instance, the left corner of $T_1L_2L_3R_4R_5T_6$ is $(1/4 + (1/2)^4 + (1/2)^5 + (1/4)^6, (1/2 + (1/2)^6)(\sqrt{3}/2)) = (1409/4096, 33\sqrt{3}/128)$. Hence, the Sierpinski point $W_{3,T_1L_2L_3R_4R_5T_6}$ is $(1409/4096, 33\sqrt{3}/128) + (1/2)^6(2/7, \sqrt{3}/7) = (10119/28672, 233\sqrt{3}/896)$.

Remark 4. Suppose that in the k -th step of the iterative deterministic construction of the Sierpinski gasket we focus our attention in one of the remaining triangles, for instance $T_1R_2R_3T_4 \cdots L_k$.

- The midpoints of the segments whose endpoints are the vertex A and the points of $T_1R_2R_3T_4 \cdots L_k$ are the points of $T_1T_2R_3R_4T_5 \cdots L_{k+1}$.
- The midpoints of the segments whose endpoints are the vertex B and the points of $T_1R_2R_3T_4 \cdots L_k$ are the points of $L_1T_2R_3R_4T_5 \cdots L_{k+1}$.
- The midpoints of the segments whose endpoints are the vertex C and the points of $T_1R_2R_3T_4 \cdots L_k$ are the points of $R_1T_2R_3R_4T_5 \cdots L_{k+1}$.

Hence, the chaos game transforms the V points [respectively, the W points] of $T_1R_2R_3T_4 \cdots L_k$ in V points [respectively, W points] of either $T_1T_2R_3R_4T_5 \cdots L_{k+1}$, or $L_1T_2R_3R_4T_5 \cdots L_{k+1}$ or $R_1T_2R_3R_4T_5 \cdots L_{k+1}$. \square

It seems useless to elaborate more on this matter to conclude that:

- In the k -th step of the classical construction of the Sierpinski gasket we may explicitly compute the coordinates of 3 V points and of 3 W points in each remaining triangle.
- The midpoint of any V point [respectively, W point] and any vertex of \mathcal{T} is a V point [respectively, a W point]. In other words, in the chaos game the set of V points and the set of W points do not communicate.
- In Sir Pinski game, a V starting point generates iterates that ultimately will land in \mathcal{V} , and a W starting point generates iterates that ultimately will land in \mathcal{W} . Hence all V and W points are winning points of the Sir Pinski game, i.e. they lie in \mathcal{S} . We say that V points [respectively, W points] are in the attraction domain of \mathcal{V} [respectively, of \mathcal{W}], or that \mathcal{V} and \mathcal{W} are invariant periodicity-3 attractors in Sir Pinski game.

Remark 5. We also observe that subsets of 3 V points and 3 W points lie in circumferences centered at the barycenter of \mathcal{T} , cf. Fig. 7. \square

3 Concluding Remarks

Under the heading “Randomness Creates Deterministic Shapes”, Peitgen *et al.* [3], p. 299, raise some interesting questions. The discussion in the previous section patently shows that the chaos game does not generate the Sierpinski gasket.

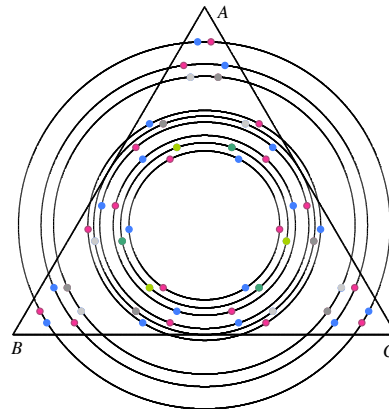


Fig. 7. A consequence of the $\frac{2\pi}{3}$ -rotational symmetry of \mathcal{S}

More precisely, if the starting point P_0 is not a Sierpinski point, its descendants are not Sierpinski points, and eventually some of them computed in the initial steps are clearly spurious specks observed upon close scrutiny of the images. The set looks like the Sierpinski gasket, because the composition of contractions creates something that is very close to the Sierpinski gasket, but its intersection with the Sierpinski gasket \mathcal{S} is void.

On the other hand, our discussion shows that sets generated by the chaos game starting with a Sierpinski V point and with a Sierpinski W point are disjoint. Moreover, any of them leaves out points in the domain of attraction of invariant attractors with periodicities other than 3.

So, even with a carefully selected Sierpinski point in any of those invariant sets, the best we can get applying the chaos game is a rarefied pale image of the rich complexity of the Sierpinski gasket. The gross imperfection of the representation of points and our eyes trick us in believing we are generating the Sierpinski gasket. In fact, the representation we get is as inaccurate as the representation we get after a finite number of steps of removal of middle triangles, in the classical deterministic construction.

Research partially supported by FCT/OE and PTDC.

References

1. M. F. Barnsley, *Fractals Everywhere*. New York, 1988, Academic.
2. J. Hutchinson, Fractals and self-similarity, *Indiana University Journal of Mathematics* 30:713-747, 1981.
3. H.-O. Peitgen, H. Jürgens, and D. Saupe. *Chaos and Fractals: New Frontiers of Science*, 2nd ed., New York, 2004, Springer.
4. M. Schroeder. *Fractals, Chaos, Power Laws: Minutes from an Infinite Paradise*. New York, 2009. Dover.



Analogue circuitry realization of neuron network

Tomas Gotthans and Jiri Petrzela

Dept. of Radio Electronics, Brno University of Technology, Brno, Czech republic
E-mail: tomas.gotthans@phd.feec.vutbr.cz

Abstract. In this paper, some new numerical as well as experimental results connected with simplified neuron model were presented. These neuron models were described by the nonlinear equations. First the differential equations describing the system were analysed from the chaos point of view. Then the system was synthesised into a circuit and was supported and verified by a measurement. The measurement proved spiking and bursting behaviour and also the presence of a chaos. The novel method of connecting the individual neural cells into the large networks was briefly discussed. This approach can be the first step of achieving the artificial intelligence.

Keywords: Chaos, neural model, neural network, artificial intelligence, Hindamarch Rose model.

1 Introduction

A huge pile of the journal articles solving problems with various models of the elemental neural cells have been published from its discovery. We present a new circuitry realization of the advanced nonlinear model (Hindamarch-Rose model) capable coupling into the arbitrary networks. For the synthesized analogue circuit the spectrum of the largest Lyapunov exponents (LLE) has been calculated. The model exhibit chaotic behaviour if some conditions are met. It needs to be modified to accomplish terms of bounding into the networks. It is well known that the most straightforward method for modelling motion of autonomous or driven dynamical systems is to design the corresponding electronic circuit. Understanding a complex dynamics is useful also from the theoretical point of view because chaos can be considered as universal phenomenon due to the normalization of the system parameters and handling with the system of the differential equations. This approach is very promising because it is the first small step towards creating basic artificial networks. Important parts creating a neural model were various measurement of a single neuron. A measurement of a single neuron is a very delicate process. First, the neuron has to be extracted from a slice of the hippo campus, followed by inserting a micro-pipette in its membrane. In this process the cell can easily be destroyed. The micro-pipette acts as measurement probe and stimulator. Because this micro-pipette does not disturb the flow of ionic currents across the membrane, the current clamped set up is close to



the natural situation of the neuron [1]. During the years many neural models were created with different porpoises.

2 Mathematical analysis of single neuron

A well known Hindmarsh-Rose system was chosen

$$\begin{aligned}\dot{x} &= y + bx^2 - x^3 - z + I(t) \\ \dot{y} &= 1 - ax^2 - y \\ \dot{z} &= \mu [s(x + x_0) - z],\end{aligned}\tag{1}$$

where dots over state variables denote time derivatives and a, b, s, μ are the real numbers. State x represents membrane potential, y is called recovery variable and the z variable represents adaptation of neuron. Constants a, b, μ and s are time constants. $I(t)$ is an external applied or clamping current as function of time. Variable x_0 is the x-coordinate of the stable sub-threshold equilibrium point. Time constants were chosen according to Hindmarsh-Rose observations.

It is computed for which real numbers (meaning a and b) the system behave chaotically. Setting parameters $a = 5$, $b = 2.96$, $mi = 0.01$, $s = 4$, $I = 2.99$ and $x_0 = 1.6$ the equilibrium points and its tight regions were investigated. The equilibria points are located at

$$P[x, y, z] = [-0.801355 \ -2.21085 \ 3.19458].\tag{2}$$

It is obvious, that for chosen values, there is only one equilibria point.

Investigation of stability around point P is given by

$$\det(\mathbf{J} - \lambda \mathbf{I}) = 0,\tag{3}$$

where J is Jacobian matrix of all first order derivatives, I is identity matrix and λ is a characteristic value. If x is equal to -0.801355 , we can get polynomial roots for λ

$$\begin{pmatrix} \lambda_1 \\ \lambda_2 \\ \lambda_3 \end{pmatrix} = \begin{pmatrix} -7.313 \\ 0.149 \\ 0.024 \end{pmatrix}.\tag{4}$$

Examination stability around fixed point in three dimensional system, where two values are positive and one is negative, we get unstable saddle point. Varying values a and b as a control parameter, the overall behaviour of system can change dramatically. Unstable fixed point is not a guarantee of chaotic behaviour. In Figure 1. can be seen a long transient performance, when integrating directly after powering on the circuit. For this case the initial conditions varies around zero $ic = [00.10]^T$. For an extensive analysis, largest Lyapunov exponents(LLE) were used. Analysing the LLE for

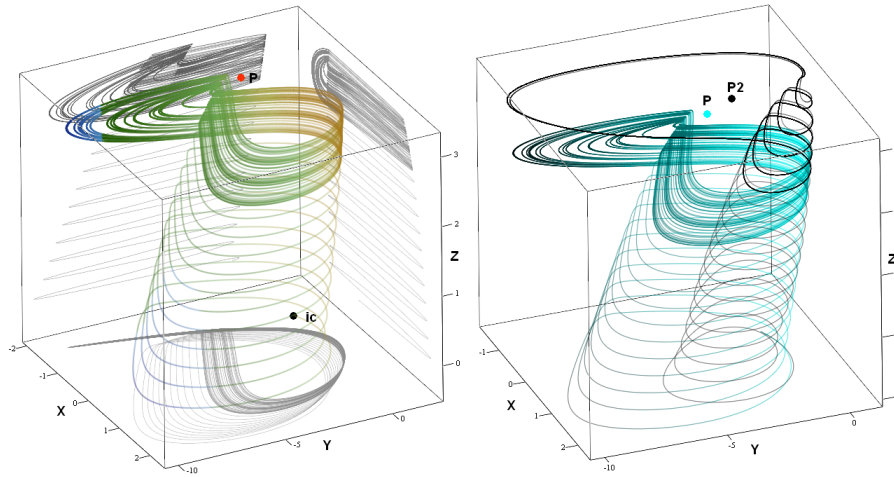


Fig. 1. Three dimensional representation of integrated system with initial point *ic* and unstable equilibria point *P* left and right is a different solution with unstable points *P* and *P2*

permutation of *a* and *b* of bonded set in Figure 2., can be seen the extreme sensitivity of parameters of the flow. Maximum obtained Lyapunov exponent was equal to $\lambda_{1max} = 0.025$ and $\lambda_{1min} = -0.055$. Slightly positive exponent is an obvious evidence of presence of a weak chaos.

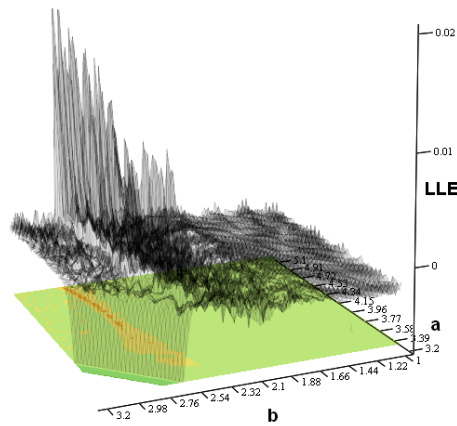


Fig. 2. Largest Lyapunov exponents for different *a* and *b*

3 Circuitry realization of single neuron

There exist several ways how to practically realize chaotic oscillators. Most of these techniques are straightforward and have been already published. Only few basic building blocks are necessary: inverting integrator, summing amplifier, analogue multipliers and voltage sources. Electronic neuron system consists of three integrator circuits (using operational amplifier TL084 with four amplifiers in one housing), which integrate the equations (1), and a multiplier circuits (also with TL084), build using AD633 multipliers, that generates the squared and cubic terms in the equations(1). Values of passive parts and voltage sources can be estimated directly from the equations. The synthesised schematics with values can be seen at Figure 3. Thus frequency re-normalization is an easy and straight-forward process covering identical change of all integration constants simultaneously.

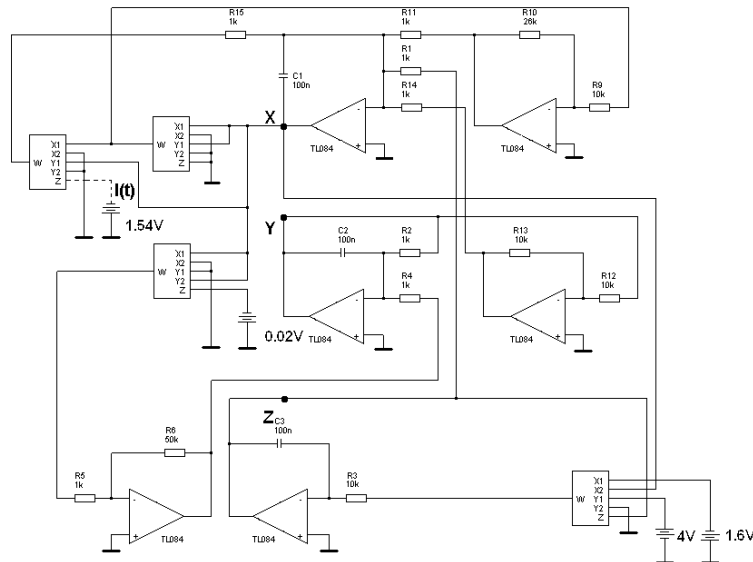


Fig. 3. Schematics of circuit realization

4 Experimental measurements of single neuron

Despite theoretical expectations, there are slight differences between the measured signals and the signals that can be obtained through numerical integration of the equations (1). This mismatch is due to tolerances of the used components, i.e. the parameters of each circuit differ a little from the nominal ones. It is also important to note that the above mentioned system has a



relatively long transient before the system becomes chaotic. This transient phenomenon was expected because it had been discovered the mathematical simulation and analysis. In Figure 4. can be seen the solution that corresponds to the most chaotic system of equations. Here the parameters of system corresponds approximately to $a = 4.91$, $b = 2.54$ in mathematical model.

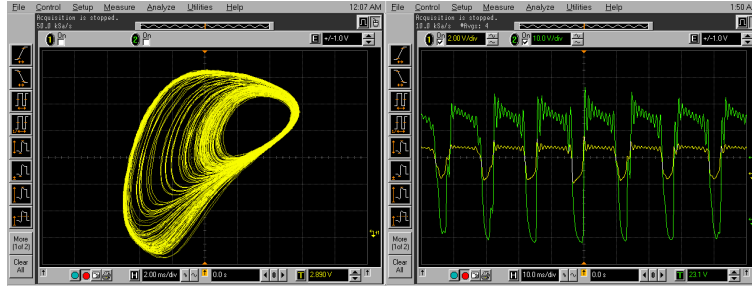


Fig. 4. Largest Lyapunov exponents for different a and b

5 Hindmarsh-Rose neural network coupling

The basic idea is build-up upon true account of Hindmarsh-Rose model and its description of physical behaviour. In case of true behaviour of a single neuron, the coupling into a networks by synapses is suggested. As porpoised in [10] the synaptically coupled two HR neurons are considered

$$\begin{aligned}\dot{\mathbf{x}}_1 &= y + bx^2 - x^3 - z - g_s(x_1 - V_{s1})\Gamma_s(x_2) \\ \dot{\mathbf{y}}_1 &= 1 - ax^2 - y \\ \dot{\mathbf{z}}_1 &= \mu [s(x + x_0) - z].\end{aligned}\quad (5)$$

Where g_s is coupling strength, V_s is the offset representing reversal potential ($V_s > x_i$) and $\Gamma_s(x)$ is the sigmoid function given by

$$\Gamma_s(x) = \frac{1}{1 + \exp(-\kappa(x - \Theta_s))}, \quad (6)$$

where κ represents slope and Θ is the threshold of sigmoid. Realizing sigmoid function by circuit is possible, but due complexity it is not necessary. In our porpoised realization sigmoid is supplied by comparator circuit. Generally the input current $I(t)$ synaptically connected with neighbouring neurons can be written as

$$I(t) = -g_s[x_1(t) - V_s]\sum_{i=1}^n w_i \Gamma[x_2(t)]. \quad (7)$$

After making the block model, the circuit realization was designed. Setting up the parameters of network is realized by digital potentiometers (w_i

and g_s). This approximation cuts of the options of setting up the network only to defined levels. The digital potentiometers were also chosen because of better management by any of external optimizing algorithms (e.g. genetic algorithms, swarm algorithms, or others). Training the network by setting the weights analogue would be almost impossible task for large networks. The circuit was designed only by the basic building blocks as in Figure 5.

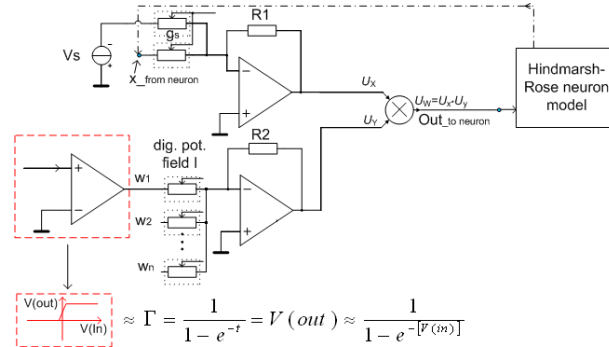


Fig. 5. Schematics of realizing coupling synapses between neurons

Analogue comparator, summing amplifier multiplier, voltage source and digital potentiometers were used. The output of synaptic model is connected with single HR model designed in Figure 3. into $I(t)$. And also integrated variable $x(t)$ is taken and connected as a feedback into synaptic model from HR circuit. The weights are set-up by digital potentiometers field and also the coupling strength is set-up by another pair of digital potentiometers.

6 Complexity of network and presence of chaos

The presence of weak chaos was proved in section 2. with the single neural model. It is obvious, that neurons connected into the proposed networks rises the order of differential equations and it can lead to robust chaotic behaviour.

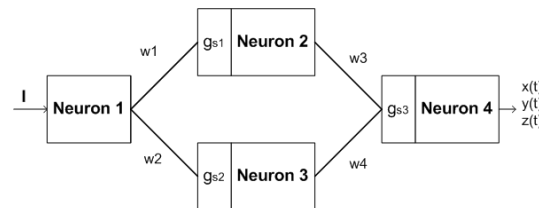


Fig. 6. Schematics of four synaptically coupled neurons



Considering four simplified mathematically coupled neurons

$$\begin{aligned}
 \dot{x}_1 &= y_1 + bx^2 - x_1^3 - z_1 + I(t) \\
 \dot{y}_1 &= 1 - ax_1^2 - y_1 \\
 \dot{z}_1 &= \mu [s(x_1 + x_0) - z_1] \\
 \dot{x}_2 &= y_2 + bx_2^2 - x_2^3 - z_2 - g_{s1}[x_2 - V_s] \left[w_1 \frac{1}{1 + \exp(-\dot{x}_1)} \right] \\
 \dot{y}_2 &= 1 - ax_2^2 - y_2 \\
 \dot{z}_2 &= \mu [s(x_2 + x_0) - z_2] \\
 \dot{x}_3 &= y_3 + bx_3^2 - x_3^3 - z_3 + -g_{s2}[x_3 - V_s] \left[w_2 \frac{1}{1 + \exp(-\dot{x}_1)} \right] \\
 \dot{y}_3 &= 1 - ax_3^2 - y_3 \\
 \dot{z}_3 &= \mu [s(x_3 + x_0) - z_3] \\
 \dot{x}_4 &= y_4 + bx_4^2 - x_4^3 - z_4 - g_{s3}[x_4 - V_s] \left[w_3 \frac{1}{1 + \exp(-\dot{x}_2)} + w_4 \frac{1}{1 + \exp(-\dot{x}_3)} \right] \\
 \dot{y}_4 &= 1 - ax_4^2 - y_4 \\
 \dot{z}_4 &= \mu [s(x_4 + x_0) - z_4].
 \end{aligned} \tag{8}$$

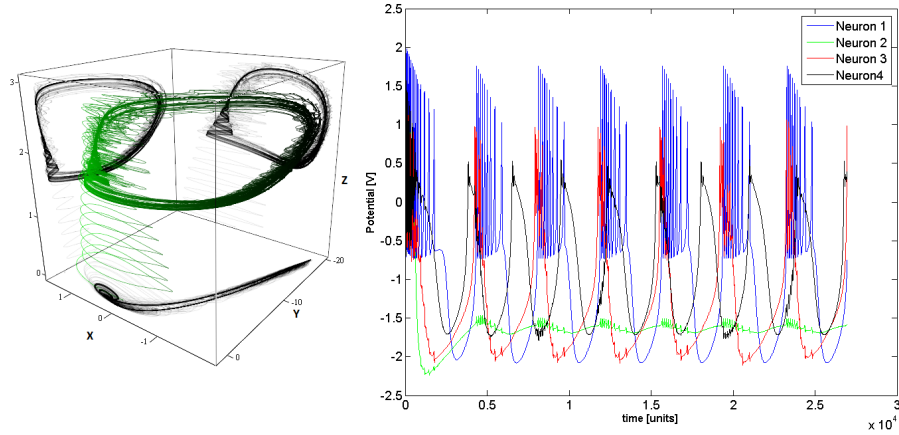


Fig. 7. Four coupled neurons and network's chaotic behaviour

Integrating numerically the system of (10) with previously mentioned parameters for single neurons, additionally with coupling strength set to $g_{s1} = 1$, $g_{s2} = 1$, $g_{s3} = 0.8$, reversal potential set to $V_s = 2$ and all weights set to 1, the Figure 7. can be obtained. The presence of chaos is almost certain.

7 Conclusion

Hindmarsh-Rose neuron system [1] was analysed and synthesized into a practical circuit. The mathematical model showed to be suitable for practical im-



plementation. The basic properties of neuron model examined by means of the numerical analysis have been discussed and verified. Huge number of the simulations reveals some cases, where the model behave chaotically. Measurements verified advanced neuron properties as is bursting and spiking, Figure 4. The synaptic model was presented and synthesised into a circuit. Creating the synapses is a very difficult task because of rising complexity with number of neural cells. Creating an array of neurons and their connections on the chip could help to create an intelligent analogue cells. Of course it would be necessary to adjust the weights in the learning process, for example, using genetic algorithm and digital potentiometers. This connection could be versatile, and there would be used in many industries. If the reader is interested in more details please do not hesitate to contact the corresponding author. Useful informations can be also found for example in [10].

Acknowledgment

Research described in the paper was financially supported by the Czech Grant Agency under grant 102/08/H027 and 102/09/P217.

References

1. Hindmarsh J. L., and Rose R. M. (1984) A model of neuronal bursting using three coupled first order differential equations. Proc. R. Soc. London, Ser. B 221:87102.
2. WOLF, A., SWIFT, J., SWINNEY, H. L., VASTANO J. A. Determining Lyapunov exponents from a time series, PHYSICA D 16, 1985.
3. Sprott, J. C. Some simple chaotic flows, PHYSICAL REVIEW E vol. 50 number 2, 1994
4. ITOH, M. Synthesis of electronic circuits for simulating nonlinear dynamics. International Journal of Bifurcation and Chaos, 2001, vol. 11, no. 3, p. 605 - 653.
5. CARROL, T., PECORA, L. Nonlinear Dynamics in Circuits. World Scientific Publishing, 1995.
6. PETRELA, J. *Modeling of the Strange Behavior in the Selected Nonlinear Dynamical Systems*, Part II: Analysis. Brno: Vutium Press, 2010.
7. SPROTT, J. C. *Chaos and time series analysis*. Oxford University Press, 2003. 507 pages.
8. SPROTT, J. C., CHLOUVERAKIS, K. E. *Labyrinth chaos*. International Journal of Bifurcation and Chaos, 2007, vol. 17, no. 6, p. 2097 - 2108.
9. GRYGIEL, K., SZLACHETKA, P. *Lyapunov exponents analysis of autonomous and nonautonomous set of ordinary differential equations*. Acta Physica Polonica B, 1995, vol. 26, no. 8, pp. 1321 - 1331.
10. Ryuta, I., Yusuke, T., Haruo, S., Takami, M. *Adaptive Estimation of Firing Patterns of Hindamarsch-Rose Neurons and Synchronization Detection with Instantaneous Lyapunov Exponents*. SICE Annual Conference 2010, 2010 Taipei, pp. 1743 - 1748.



Chaos and multiple mode spatio-temporal complexity in thermo-visco-elastic systems subject to laser irradiation

O. Gottlieb and E. Hollander

Department of Mechanical Engineering, Technion - Israel Institute of Technology, Haifa 32000, Israel

A self-excited nonlinear dynamical system is one that, in the absence of external modulated forcing, will undergo bounded periodic limit-cycle oscillations beyond a stability threshold of an equilibrium state. Thermally driven limit-cycle oscillations have been shown to occur in mechanical systems that span multiple spatial scales. A large scale example is a space structure which absorbs solar radiation that can either increase or decrease as the structure bends towards or away from the incoming radiation. This consists of a feedback loop that can change the equilibrium configuration or can lead to self-excited bending vibrations. Additional examples include limit-cycle oscillations of a five cm long aluminum coated glass cantilever [1], and recently, various nano-resonators in the shape of disks, domes, paddles and wires [2]. The advantages of self-excited nano-electro-mechanical-systems include a dramatic improvement of the quality factor via parametric amplification, stability enhancement through the use of feedback, and incorporation of a single optical configuration for both drive and motion sensing. To date, these systems have been modeled by single-degree-of-freedom resonators coupled to a lumped-mass thermal description. However, while their analysis qualitatively reveals the onset of limit cycle oscillations, the analytically determined thresholds differ from measurements by a factor of two [2]. Furthermore, these systems have been shown experimentally to exhibit complex vibrations that alternate between several continuous vibration modes which cannot be explained by lumped-mass models [1].

Thus, in order to resolve the spatio-temporal complexity of the thermo-visco-elastic system response near primary, secondary and multiple internal resonances, we formulate an initial-boundary-value problem that consistently includes both nonlinear viscoelastic and thermal fields [3]. We determine the coupled thermo-elastic field basis functions and construct a low-order nonlinear multi-mode dynamical system for the experimental conditions (Fig. 1) defined by Hane in 1996 [1].

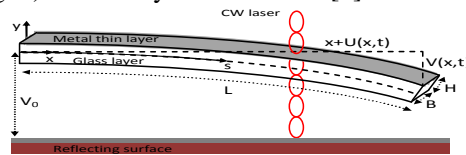


Figure 1: Definition sketch of the laser irradiation initial-boundary-value problem.

The resulting dynamical system truncated to cubic order, consistently incorporates the coupled thermo-visco-elastic equations [3] with the geometric stiffness and gyroscopic nonlinearities of a micro-cantilever developed for finite amplitude dynamics in atomic force microscopy [4]. The influence of the laser is embedded within the thermal field equation as the time-averaged absorption of a standing wave captured within a bi-material (the cantilever) and the mirror, creating a Fabri-Pero interferometer. Stability analysis of the thermo-elastic dynamical system equilibrium configuration reveals existence of a complex bifurcation structure (Fig. 2) which includes coexisting bi-stable solutions between snaddle-node pairs, and flutter thresholds that correspond to saddle-node and Hopf bifurcations, respectively.

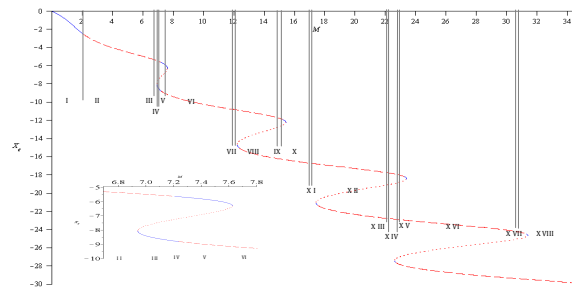


Figure 2: Bifurcation diagram of equilibrium as a function of input power (solid-stable, dashed-unstable).



A numerical analysis of system response exhibits free vibration decay (Fig. 3 left) below the Hopf threshold in region I of Figure 2, self-excited vibrations (Fig. 3 center) for the low power input documented by [1] in region II of Figure 2, and possible irregular chaotic jumps (Fig. 3 right) between coexisting bi-stable solutions in region V of Figure 2.

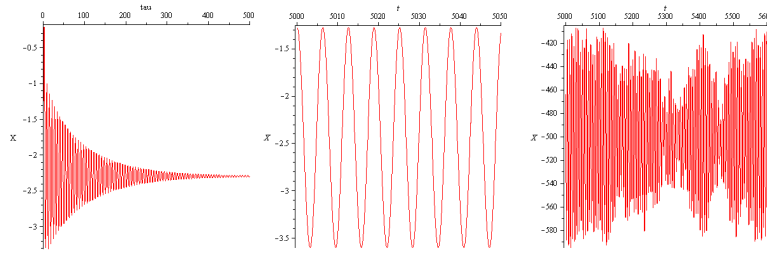


Figure 3: Cantilever tip time-series response: free decay (left) below the first Hopf threshold, periodic limit-cycle motion above the first Hopf threshold (center), and non-stationary response above the first bi-stable transition (right).

Investigation of system periodicity via sampling of the non-dimensional displacement (X) and temperature (Z) response intersection with the zero velocity plane ($Y=0$), yields a bifurcation diagram of Poincare' points for various values of input power (Fig. 4 left). The bifurcation structure reveals a period-doubling mechanism ($M \sim 15$) which culminates with a strange attractor ($M \sim 15.5$) which is then destroyed via a reverse bifurcation ($M \sim 16$).

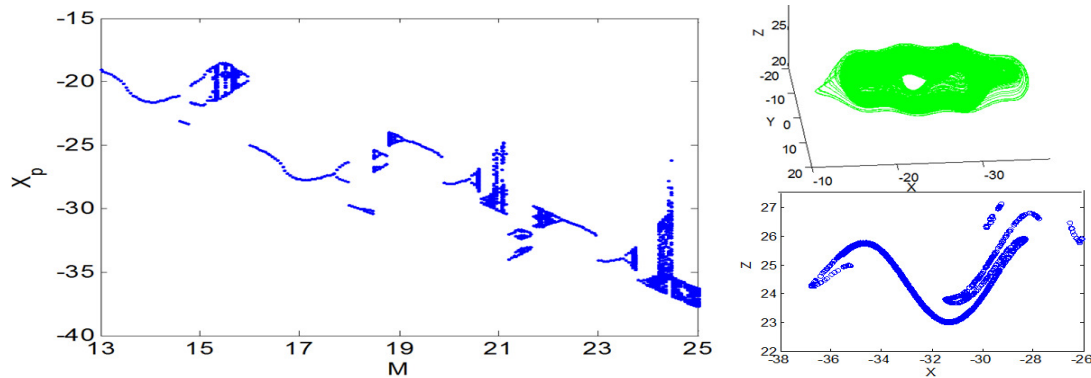


Figure 4: A bifurcation diagram (left) depicting the displacement Poincare' points (X_p) for increasing laser intensity (M) spanning regions VII to XVI in Figure 2. A three dimensional chaotic state-space (upper right) and fractal Poincare' map projection (lower right) for a selected intensity in region XVI of Figure 2 ($M=24.4$).

An example chaotic strange attractor ($M=24.4$) is depicted (Fig. 4 upper right) via its three dimensional state-space [$Z(X,Y)$] and (Fig. 4 lower right) Poincare' map projection [$Z(X)$] which exhibits a distinct fractal behavior that includes both stretch and fold properties.

This numerical investigation enables a quantitative description of a complex multiple-mode bifurcation structure that includes coexisting equilibrium solutions, self-excited periodic oscillations, quasiperiodic solutions due to a 3:1 internal resonance between the third and second modes, and chaotic structural response of the thermo-visco-elastic dynamical system that is subject to laser irradiation.

[1] Hane, K. and Suzuki, K., *Sensors and Actuators A* 51, 179-181, 1996.
 [2] Aubin, K. et al, *J. Microelectromechanical Systems*, 13, 1018-1026, 2003.
 [3] Gottlieb, O. and Champneys, A.R., in *Solid Mechanics and its Applications* vol. 122, eds. Rega G. and Vestroni. F., Springer, 117-126, 2005.
 [4] Hornstein, S. and Gottlieb, O., *Nonlinear Dynamics*, 54, 93-122, 2008.
 [5] Lenci, S. and Rega, G., *J. Micromechanics and Microengineering*, 16, 390-401, 2006.